2023-08-21

Constructing Stellar Mass Models for Early-type Galaxies with Circumnuclear Disks

Jared R. Davidson
Brigham Young University

Constructing Stellar Mass Models for Early-type Galaxies with Circumnuclear Disks

Jared R. Davidson

A thesis submitted to the faculty of
Brigham Young University
in partial fulfillment of the requirements for the degree of

Master of Science

Benjamin Boizelle, Chair
Eric Hintz
Denise Stephens

Department of Physics and Astronomy

Brigham Young University

ABSTRACT

Constructing Stellar Mass Models for Early-type Galaxies
with Circumnuclear Disks

Jared R. Davidson
Department of Physics and Astronomy, BYU
Master of Science

Dusty circumnuclear disks (CNDs) in luminous early-type galaxies (ETGs) show regular, dynamically cold molecular gas kinematics. For a growing number of these ETGs, Atacama Large Millimeter/sub-millimeter Array (ALMA) CO imaging and detailed gas-dynamical modeling have yielded moderate to high precision black hole (BH) mass ($M_{\rm BH}$) determinations. To date, however, few studies have explored the effects of dust attenuation, or uncertainties in dust corrections, on recovered stellar luminosity models from high angular resolution optical/near-IR observations and $M_{\rm BH}$ measurements. Recent kinematic studies that modeled ALMA CO data sets have found that uncertainties in the intrinsic central stellar surface brightness slope due to dust may even dominate the BH mass error budgets. From the ALMA archive, we identified a subset of 26 ETGs with clean CO kinematics and good prospects for eventual $M_{\rm BH}$ determination but that did not have sufficiently high angular resolution observations in the optical and near-IR. We have obtained new optical and near-IR Hubble Space Telescope (HST) images of this sample to supplement the archival HST data. Together, these new and archival HST data will enable the mitigation of dusty CND obscuration in the construction of dust-corrected stellar luminosity models, leading to both BH mass measurement and complete error analysis using existing ALMA CO imaging. Here, we present the sample properties, data analysis techniques, and dust-masked stellar surface brightness profiles and luminosity models using the multi-Gaussian expansion formalism. With estimated $M_{\rm BH}/M_{\odot} \gtrsim 10^8$ to few $\times 10^9$, securing quality $M_{\rm BH}$ determinations for this sample of ETGs will significantly improve the high-mass end of the current BH census, facilitating new scrutiny of local BH mass-host galaxy scaling relationships.

Keywords: galaxies: elliptical and lenticular, galaxies: nuclei, galaxies: kinematics and dynamics

ACKNOWLEDGMENTS

This work represents the scientific exploration and the journey of the past few years. I acknowledge the support of my lovely wife who encouraged me to pursue this degree and helped to make it a reality.

I acknowledge the funding I have received from the Space Telescope Science Institute (STScI), which provided support for this project through a grant under NASA contract NAS5-26555. I also acknowledge support from the BYU Department of Physics and Astronomy. I also appreciate the members of my committee, who have provided encouragement and direction along the way.

I am grateful to my advisor, Dr. Benjamin Boizelle. He has taught me how to be an extragalactic astronomer and has spent *many* hours helping, directing, and guiding this project. Most of all, I am grateful that he cared about me as a person, as well as my success as a graduate student.

This work has made use of archival data obtained with the Spitzer Space Telescope, which was operated by the Jet Propulsion Laboratory, California Institute of Technology under a contract with NASA. This work as made use of observations made with the NASA/ESA Hubble Space Telescope, and obtained from the Hubble Legacy Archive, which is a collaboration between the Space Telescope Science Institute (STScI/NASA), the Space Telescope European Coordinating Facility (ST-ECF/ESA) and the Canadian Astronomy Data Centre (CADC/NRC/CSA). This research has made use of the HyperLEDA database and the NASA/IPAC Extragalactic Database (NED) which is operated by the Jet Propulsion Laboratory, California Institute of Technology, under contract with the National Aeronautics and Space Administration.

Contents

List of Figures

List of Tables

Chapter 1

Introduction

This thesis describes our approach to facilitating more robust black hole mass error budgets, especially when modeling CO kinematics. The immediate goal of this project is to study the nuclear stellar surface brightness properties using a range of Hubble Space Telescope broadband imaging of a subset of massive early-type galaxies with dusty gas disks around the galactic core, primarily through observations of dust absorption. These are the first steps in creating dust maps for selected early-type galaxies to use in constructing dust-corrected models of stellar surface brightness profiles, which when paired with CO kinematics will help achieve a more complete and fulsome black hole mass error budget. We emphasize that stellar surface brightness models are necessary for obtaining black hole mass measurements when using gas-dynamical modeling. Previous stellar surface brightness models were not always uniformly constructed and at times lacked a straightforward approach to masking dust features. The models described in this thesis aim to correct these problems and provide the best possible results when paired with gas-dynamical modeling.

We first explain some terminology used in this thesis to avoid confusion, roughly in the order in which the terms will appear.

1.1 Terminology

Dust extinction is the absorption and scattering of light by dust and gas between a light source and the observer. **Dust attenuation** refers to the net effect of dust on geometrical distribution of light sources, where the light sources are found in front of and behind the dust at a range of depths. The dust itself can be clumpy, smooth, or anything in between. The relative location of both the light sources and the dust has a major impact on the net absorbed and scattered light. It is important to note that light can be scattered *out of* as well as *into* the line of sight of the observer.

Velocity dispersion (σ) is the statistical dispersion of velocities about the mean velocity for a group of astronomical objects. Using spectroscopy to measure the radial velocities of the group's members, the velocity dispersion can be estimated and used to derive the group's mass using the virial theorem ($GM(<r)/r \approx \sigma^2$), where $M(<r)$ is the mass enclosed within the radius r. A **central velocity dispersion** refers to the σ of the interior regions of an extended object (e.g., a galaxy or group/cluster of galaxies).

Brightest group galaxy (BGG) and **brightest cluster galaxy (BCG)** are defined as the brightest galaxy in a group or cluster of galaxies, respectively. A group of galaxies is a collection of large galaxies comprising $\sim$50 or fewer gravitationally bound members. A cluster of galaxies is larger, with anywhere from hundreds to thousands of large galaxies gravitationally bound together. BCGs are generally elliptical galaxies and include the most luminous and largest galaxies in the universe, residing in the highest density regions.

A **cored** or **cuspy** profile refers to the shape of a galaxy's stellar surface brightness or dark matter density profile at small radii. Cored profiles flatten out to a constant value, whereas cuspy profiles continue to increase towards the center (see example in Figure 1.1). Cored profiles indicate a near-isothermal central region and are generally found in more luminous early-type galaxies. Cuspy profiles indicate a non-isothermal central region and are found in less luminous early-type galaxies.

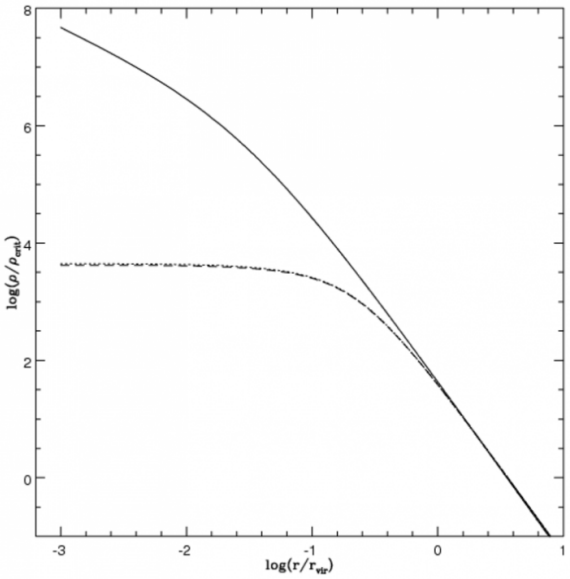

Figure 1.1 Example of cuspy and cored density profiles. The cored profile (dashed line) flattens out to a constant value at small radii. The cuspy profile (solid line) continues to increase towards the center. [Adapted from Del Popolo (2009)]

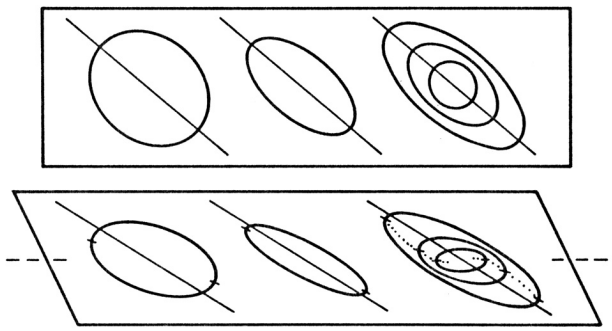

Figure 1.2 Example of how isophotal twisting can occur. The upper panel is a face-on view of isophotes with different ellipticities but a single position angle. In the lower panel the same configurations are viewed at an angle. When flat ellipses are viewed at skewed orientations, projection effects make the apparent major axes (ticks) rotate away from the intrinsic major axes (straight lines) toward the line (dashed) about which the objects have been rotated to produce the viewing geometry. The change in apparent position angle is larger for isophotes that are rounder, producing a twist in the position angle with radius. [From Kormendy (1982)]

Effective radius is the radius within which half of the galaxy light is contained. Galaxy sizes are difficult to measure because they lack a clearly defined boundary to their outer regions. The apparent size of a galaxy will therefore depend almost entirely on the sensitivity of the telescope, the exposure time of the observations, and the orientation of the galaxy with respect to the line of sight of the observer. To relieve some of this ambiguity, astronomers use the effective radius to help gauge galaxy sizes.

AGNs are active galactic nuclei that emit non-stellar radiation resulting from black hole accretion disks. They have a higher than normal luminosity over at least some portion of the electromagnetic spectrum. Such excess emission has been observed in the radio, microwave, infrared, optical, ultra-violet, X-ray, and gamma ray regimes. A galaxy hosting an AGN is called an active galaxy.

Isophotal twisting refers to the observed twist in major-axis position angle of isophotes with increasing radius (see Figure 1.2). A twist *can* imply that the true principal axes change position angle with radius, though projection effects on concentric ellipses with the same position angle but differing ellipticities can achieve the same result. Generally, galaxies that show large isophotal twists are thought to have recently been gravitationally perturbed, either through close interaction with another galaxy or through a galaxy merger.

1.2 Background

Supermassive black holes (BHs), spanning a mass range of $\sim 10^5 - 10^{10}\ M_\odot$, are believed to be at the center of nearly every large galaxy. Over the past two decades, dynamical modeling techniques have been employed to measure BH masses ($M_{\rm BH}$) in well over 100 galaxies (e.g., Kormendy & Ho 2013; Saglia et al. 2016). Although BHs gravitationally dominate only the innermost regions of their host galaxies (often not more than the central few parsecs [pc]), their masses strongly correlate with several large-scale galaxy properties, especially the stellar bulge velocity dispersion

($\sigma_\star$; e.g., Ferrarese & Merritt 2000; Gebhardt et al. 2000) and luminosity or mass ($L_{\rm bul}$ or $M_{\rm bul}$; e.g., Kormendy & Richstone 1995; McConnell & Ma 2013). Such empirical relations suggest a co-evolution of the central BH and its host galaxy through a series of accretion and merger events across cosmic history. During this galaxy growth, star formation is regulated by feedback processes. However, the detailed nature of these scaling relationships – including the intrinsic scatter and behavior by galaxy morphology – remain uncertain due to small samples, many poorly constrained $M_{\rm BH}$ values, and persistent selection biases.

For the most luminous early-type galaxies (ETGs), which includes several brightest group and cluster galaxies (BGGs, BCGs), current data hint at a steeper $M_{\rm BH}-\sigma_\star$ slope for those with cored stellar surface brightness profiles (Bernardi et al. 2007; Lauer et al. 2007). This suggests that BH growth in merger-rich environments follows a different evolutionary path (e.g., see Bogdán et al. 2018) due to the prevalence of dry (gas-poor) mergers in clusters and to a lesser extent in groups. However, the BH census remains incomplete above $\sim 10^{8.7}\ M_\odot$, and uncertainties in this high-mass regime are typically large (of order 25%; e.g., Saglia et al. 2016). In addition, potentially serious (and often unexplored) systematics in both stellar and gas-dynamical models may bias $M_{\rm BH}$ measurements (see Kormendy & Ho 2013 for further discussion). A larger sample of $M_{\rm BH}$ for BGGs and BCGs, together with greater measurement precision, are necessary for any confident interpretation of BH-host galaxy co-evolution in dense galaxy environments.

Extended atomic and/or molecular gas is detected in about half of all ETGs (Young et al. 2011), often forming filaments or dusty circumnuclear disks (CNDs) with typical radii of $\sim$100 pc to several kpc. Although many show disturbed morphologies or evidence for incomplete settling processes (e.g., Tran et al. 2001), roughly $10-20$% of the total host morphologically round CNDs that suggest dynamically cold kinematics (e.g., Lauer et al. 2005). Because of their small physical extent, CND kinematics are less sensitive to uncertainties in large-scale galaxy properties that often hampers stellar-dynamical efforts (e.g., McConnell & Ma 2013; van den Bosch & de Zeeuw

2010). The most reliable $M_{\rm BH}$ determinations originate from spatially resolved tracer kinematics that extend well within the sphere of influence[1] ($r_{\rm g} \approx GM_{\rm BH}/\sigma_\star^2$) where the BH's gravitational influence dominates over the galaxy's extended mass contributions. In many CNDs, these tracer kinematics are detected down to near – or even well within – $r_{\rm g}$, making them appealing targets for constraining BH masses.

The origin of these CNDs is still a topic of ongoing research. Three possible scenarios are often discussed to explain the presence of dusty molecular gas in ETGs (e.g., see Davis et al. 2019): (i) the gas could be a remnant of the star-forming reservoir from before the galaxy was morphologically transformed; (ii) the gas could have been constantly replaced by an internal source, such as stellar mass loss or cooling of the hot halo; (iii) the gas could be acquired externally from minor/major mergers and cold accretion. The first of these possibilities has been explored, and while star-forming reservoirs can be present, they do not dominate the population of gas-rich ETGs and thus the other mechanisms also seem to be important (Davis et al. 2019). Previous studies have found no correlation between the ambient galaxy density and the presence of dusty CNDs or filamentary dust in ETGs (e.g., Tran et al. 2001), which suggests the molecular gas and dust in these CNDs are of internal origin. Others have found evidence for molecular gas in ETGs that is likely of external origin, the amount of which is consistent with a minor merger origin (Alatalo et al. 2013). Recent statistical analyses seem to show that, in galaxy centers, denser bulges appear to keep the gas more stable and allow for the formation of smooth CNDs in ETGs because of high shear, the absence of stellar spiral density waves, and/or the absence of inflowing gas (Davis et al. 2022). Clearly, molecular gas reservoirs are common across the ETG population, regardless of whether the ETG is in isolation or part of a group or cluster. The amount of gas present, however, is affected by

[1]Note that some authors define the SOI radius $r_{\rm g}$ as $GM_{\rm BH}/\sigma_\star^2$ while other authors use a separate radius (e.g., $r_{\rm eqv}$; Yoon 2017) where $M(<r) = 2M_{\rm BH}$. In practice, $r_{\rm g}$ and the equivalence radius may be distinct by a factor of perhaps 2, especially when $M_{\rm BH}$ is estimated based on scaling relationships (see Boizelle et al. 2019). Here, we use the oft-used relation for $r_{\rm g}$ that relies on $\sigma_\star$.

environment. Mergers appear to dominate the supply of gas, but stellar mass loss, hot halo cooling, and remnants of the galaxy's late-type stage may also play a role (Davis et al. 2019).

At typical distances of 20−50 Mpc for nearby ETGs, these CNDs subtend an angular size of only a few arcseconds or less with the typical r_g of the host BH on the order of $\sim 0\farcs05 - 1\farcs0$. These CND systems are therefore difficult to resolve and study in the optical/near-IR wavelengths except with the Hubble Space Telescope (HST) or large-aperture ground-based facilities with adaptive optics capabilities. Unfortunately, kinematic modeling of ionized atomic and warm molecular gas components has been challenging due to high gas turbulence and possible non-circular motion (e.g., Neumayer et al. 2007; Verdoes Kleijn et al. 2006). In certain H_2O megamaser systems, very long baseline interferometry has revealed emission extending from $\sim r_g$ down to perhaps $0.1 r_g$ (e.g., Kuo et al. 2011; Zhao et al. 2018), tracing a Keplerian-like potential and enabling precision M_{BH} determinations in the best cases. Given their rarity and non-detection in the most massive galaxies (van den Bosch et al. 2016), however, these megamaser disks also have limited application in building a more complete high-mass BH census.

Early generations of mm/sub-mm interferometric arrays could resolve cold molecular gas kinematics in only a small number of CNDs (Davis et al. 2013), although the regular dust morphologies and lower-resolution ^{12}CO imaging hinted at the prevalence of dynamically cold molecular gas (Alatalo et al. 2013; Davis et al. 2011; Maiolino 2008). Now, the order-of-magnitude improvements in both angular resolution and sensitivity of the Atacama Large Millimeter/sub-millimeter Array (ALMA) provide a more promising avenue to expand the BH census with precision M_{BH} across the full mass range of ETGs using low-J CO lines. This is especially valuable for the most luminous galaxies with BH masses above $\sim 10^{8.7}\ M_\odot$, which tend to have large physical r_g. To date, resolved ALMA CO imaging has been used to great effect, mapping molecular gas kinematics in a few dozen ETGs with dusty gas disks (Barth et al. 2016a;b; Boizelle et al. 2017; 2021; Cohn et al. 2021; Davis et al. 2017; 2018; North et al. 2019; Onishi et al. 2017; Ruffa et al. 2019; 2023; Smith et al. 2019;

Table 1.1. ETG Sample

Galaxy Name (1)	RC3 Type (2)	$m-M$ (mag) (3)	A_{F160W} (mag) (4)	z (5)	D_L (Mpc) (6)	D_A (Mpc) (7)	Scale (kpc arcsec^{-1}) (8)	R_e (kpc) (9)	σ_c (km s^{-1}) (10)	M_K (mag) (11)	L_H (10^{11} $L_\odot$) (12)	r_g (arcsec) (13)
Hydra A	(R')SA0^−:	36.89 ± 0.15	0.021	0.055782	238.70	214.14	1.038	17.79	341.1	−25.99	4.958	0.13
NGC 612	SA0^+ pec edge-on	35.46 ± 0.15	0.010	0.029430	123.60	116.63	0.565	5.79	···	−25.86	3.591	0.22
NGC 997	E	34.71 ± 0.15	0.071	0.021015	87.70	84.13	0.408	4.96	···	−25.26	2.168	0.22
NGC 1332	S0^−:(s) edge-on	31.80 ± 0.18[1]	0.017	0.005180	22.91	22.67	0.110	2.87	294.6	−24.74	1.369	0.57
NGC 1387	SAB0^-(s)	31.80 ± 0.09[5]	0.006	0.004079	19.32	19.16	0.093	1.40	167.3	−23.94	0.593	0.42
NGC 3245	SA0^0(r):?	31.43 ± 0.20[1]	0.013	0.005854	20.89	20.65	0.100	2.87	207.0	−23.70	0.658	0.33
NGC 3258	E1	32.53 ± 0.27[1]	0.041	0.009580	32.06	31.46	0.153	2.57	261.0	−24.34	0.788	0.32
NGC 3268	E2	32.73 ± 0.25[1]	0.053	0.009280	34.83	34.20	0.166	5.99	228.6	−24.54	1.342	0.34
NGC 3271	SB0^0(r)	33.73 ± 0.15	0.056	0.013393	55.60	54.14	0.262	4.43	246.8	−25.54	2.785	0.40
NGC 3557	E3	33.30 ± 0.22[1]	0.052	0.009867	45.71	44.82	0.217	6.64	270.3	−26.06	4.844	0.65
NGC 3862	E	34.95 ± 0.15	0.012	0.023403	97.80	93.38	0.453	15.26	265.1	−25.41	3.946	0.21
NGC 4061	E:	35.21 ± 0.15	0.018	0.026302	110.20	104.62	0.507	10.48	477.2	−25.32	3.116	0.18
NGC 4261	E2−3	32.34 ± 0.19[2]	0.009	0.003332	29.38	29.18	0.141	5.03	296.7	−25.05	2.100	0.54
NGC 4373a	SA0^+: edge-on	32.60 ± 0.52	0.043	0.008019	33.10	32.58	0.158	2.94	201.6	−23.77	0.640	0.23
NGC 4429	SA0^+(r)	30.73 ± 0.15	0.017	0.003382	13.90	13.81	0.067	2.65	173.4	−23.93	0.647	0.58
NGC 4435	SB0^0(s)	31.12 ± 0.05[4]	0.015	0.003399	16.75	16.64	0.081	1.38	155.0	−23.75	0.420	0.41
NGC 4697	E6	30.35 ± 0.14[1]	0.015	0.005114	11.75	11.63	0.056	2.32	165.2	−24.00	0.658	0.71
NGC 4751	SA0^−:	31.86 ± 0.16	0.062	0.005694	23.50	23.24	0.113	2.91	350.6	−23.59	0.601	0.29
NGC 4786	cD pec	34.26 ± 0.15	0.019	0.017115	71.20	68.82	0.334	8.49	284.7	−25.51	3.743	0.30
NGC 4797	S0^−:	35.35 ± 0.15	0.006	0.028053	117.70	111.36	0.540	6.14	201.7	−25.44	2.210	0.18
NGC 5084	S0 edge-on	31.85 ± 0.15	0.060	0.005664	23.40	23.14	0.112	2.50	199.8	−24.77	1.139	0.59
NGC 5193	E pec:	33.35 ± 0.15[2]	0.029	0.010247	46.77	45.83	0.222	3.30	205.1	−24.66	1.196	0.24
NGC 5208	S0	35.09 ± 0.15	0.018	0.024894	104.20	99.20	0.481	12.19	···	−25.55	4.454	0.22
NGC 5838	SA0^−	31.75 ± 0.15	0.027	0.005420	22.40	22.16	0.107	1.74	273.6	−24.13	0.667	0.41
NGC 6861	SA0^−(s):	32.24 ± 0.36[1]	0.028	0.010137	28.05	27.49	0.133	2.41	387.2	−24.74	1.278	0.47
NGC 6958	cD	33.03 ± 0.15	0.023	0.009750	40.30	39.53	0.192	2.98	185.2	−24.59	1.246	0.30

Note. — Properties of the ETGs observed with these HST programs. Col. (3) lists the distance modulus, with preference for SBF measurements, otherwise calculated from the adopted luminosity distance values. SBF measurements were drawn from [1]Tonry et al. (2001), [2]Jensen et al. (2003), [3]Cantiello et al. (2005), [4]Mei et al. (2007), [5]Blakeslee et al. (2009). Cols. (4) and (5) report Galactic extinction in the WFC3/F160W band and optical redshifts from the NASA/IPAC Extragalactic Database after correcting for the Virgo + Great Attractor + Shapley inflow model (Mould et al. 2000). Cols. (6) and (7) give the luminosity distance D_L and angular size distance D_A corresponding to the adopted z values as well as a standard cosmology described in §1.3, computed using the Wright (2006) cosmological calculator. The corresponding physical scale is given in col. (8). Col. (9) gives the effective radius R_e as estimated from multi-Gaussian expansion models. Col. (10) gives the measured central stellar velocity dispersion from the HyperLEDA database (Paturel et al. 2003). From this same database, the apparent total K-band magnitudes are combined with the adopted D_L to estimate M_K for each galaxy in col. (11). Col. (12) gives the total H-band luminosity as estimated from multi-Gaussian expansion models. Lastly, col. (13) gives the r_g value estimated from the $M_{BH} - L_K$ scaling relation.

2021b). Increasingly detailed gas-dynamical modeling of the observed CO data cubes has resulted in some of the most precise BH mass measurements to date.

The confidence of both stellar and gas-dynamical models rely on an accurate model of the galaxy mass as a function of radius. In most cases, the gas masses of CNDs in ETGs range between just $\sim 10^5$–10^9 $M_\odot$ (e.g., Boizelle et al. 2017; Ruffa et al. 2019; Young et al. 2011), meaning that

the extended mass profile remains dominated by the stellar component out to a few effective radii (R_e). Models of a galaxy's mass profile are typically derived from 2D images of the observed stellar surface brightnesses. Unfortunately, the large CO column densities of these embedded CNDs are accompanied by relatively high dust surface mass densities that also obscures the stellar light originating from behind the disk. The intrinsic dust extinction is not known *a priori*, but early studies have demonstrated peak $A_V \sim 3-5$ mag of the background stellar light (e.g., Boizelle et al. 2019; 2021; Cohn et al. 2021; Ferrarese et al. 1996; Kabasares et al. 2022; Viaene et al. 2017; c.f. much lower foreground screen estimates, e.g., Tran et al. 2001).

Some of these authors have adopted a range of plausible extinction corrections to explore the effects of dust extinction on the final best-fitting M_{BH} value (see also Viaene et al. 2017). Due in large part to exquisite CO kinematics, these ALMA studies have shown that uncertainty in the dust extinction correction tends to be the dominant term in the BH mass error budget, excluding contributions arising from the uncertainty in the distance to the galaxy. For cases where ALMA imaging does not resolve CO kinematics as deeply within r_g, the overall error budget may appreciably broaden. In cases where we have seen kinematics that are more warped or less regular, perhaps due to low CO signal-to-noise, dust extinction will likely be an important – but not always dominant – source of uncertainty.

1.3 ALMA Archival CO Imaging

The ALMA archive now contains low-J CO imaging for well over 100 nearby ETGs, many of which have average synthesized beam full width at half maximum (FWHM) $\theta_{FWHM} \lesssim 2r_g$ that may enable a good quality M_{BH} determination (Davis 2014). A fraction of these ETGs have neither broadband optical nor near-IR observation with an angular resolution similar to r_g (or at least θ_{FWHM}). To construct stellar luminosity models, near-IR data is preferred to mitigate the impact

of dust attenuation on the stellar light that originates from behind the CND. Stellar luminosity models may still be derived from lower-resolution ($\sim 1''$) imaging, although doing so may introduce additional bias in the best-fitting $M_{\rm BH}$ (see Yoon 2017). To facilitate more confident BH mass measurement, we developed an HST program to obtain new broadband imaging for ETGs with the most promising ALMA CO emission-line data sets (i.e., which have large $r_{\rm g}$ and small $\theta_{\rm FWHM}$, with regular kinematics) but that had no near-IR (or, at times, even optical) HST imaging.

Since initial proposals by Dickey & Kazes (1992) and Sofue (1992), CO has also been used as an alternative to other emission line tracers as a probe of asymptotic rotational velocities (e.g., Davis et al. 2016; 2011; Ho 2007; Tiley et al. 2016; 2019; Topal et al. 2018), with the resulting CO Tully-Fisher (TF) relation being used to study extragalactic sources. CO offers many advantages compared to other tracers, including that the underlying molecular gas is relatively insensitive to environmental perturbations. Observed CO line profiles are more irregular in general than traditionally-used H I profiles (Ho 2007; Smith et al. 2021a). For morphologically round CNDs, however, these CO velocity profiles are typically double-horned and sharp-edged (sometimes with high-velocity emission in the wings; Boizelle et al. 2017; 2021; Ruffa et al. 2019). These previous studies assumed the velocity curve traced by the CO disk either reached $V_{\rm max}$ (followed quickly by a turnover) or an asymptotic circular velocity due to the combined mass distribution, with asymptotic velocities typically occurring beyond an inner $V_{\rm max}$. However, Smith et al. (2021a) did recognize that gas tracers might not extend far enough to probe $V_{\rm max}$, resulting in smaller CO line widths and incorrect estimation of correlated galaxy properties (e.g., $\sigma_\star$, $M_\star$, $M_{\rm BH}$). We therefore also look to test the reliability of the CNDs in our target ETGs when pursuing a CO TF analysis.

Throughout this paper, we adopted a standard ΛCDM cosmology with $\Omega_{\rm m} = 0.308$, $\Omega_{\rm vac} = 0.692$, and the more local Hubble constant value $H_0 = 73$ km s^{-1} Mpc^{-1} (Blakeslee et al. 2021; Kenworthy et al. 2022; Riess et al. 2022).

1.4 ETG Sample

Targets for this project, listed in Table 1.1, were identified from CO(1−0), CO(2−1), and/or CO(3−2) imaging of ETGs in ALMA Cycles 2−5. Figure 1.3 shows the ALMA CO surface brightness and luminosity-weighted line-of-sight velocity maps for a subset of the full target list. These disks show a wide range of CO morphologies, including ring-like, inclined, mildly disrupted, and more centrally concentrated configurations. In each case, we find the CO kinematics to be very regular, giving confidence that future gas-dynamical modeling could constrain $M_{\rm BH}$. Using measured central stellar velocity dispersions and the $M_{\rm BH} - L_K$ scaling relation (Kormendy & Ho 2013), we selected ETGs with estimated $r_{\rm g} \gtrsim 0\farcs09$ to ensure that $r_{\rm g}$ could be fully resolved, if not in archival CO imaging with $\theta_{\rm FWHM} \sim 0\farcs1 - 0\farcs6$ then in future ALMA imaging using a more extended configuration in a reasonable amount of time. The final sample consists of 26 ETGs, with slightly more lenticular galaxies than classical ellipticals. Nearly all are members of galaxy groups. Five – Hydra A, NGC 3258, NGC 3268, NGC 3557, and NGC 6861 – are referred to in the literature as either BGGs or BCGs. These new HST data were obtained over three separate programs in HST Cycles 24, 25, and 27.

For 12 of these galaxies, we adopted luminosity distances (D_L) from surface brightness fluctuation (SBF) distance modulus measurements (Blakeslee et al. 2009; Cantiello et al. 2005; Jensen et al. 2003; Mei et al. 2007; Tonry et al. 2001). For the remaining 14 galaxies lacking SBF-derived $m - M$ values, we estimated D_L from Hubble flow velocities using the Virgo + Great Attractor + Shapley Supercluster inflow model (Mould et al. 2000) and the Wright (2006) cosmological calculator, assuming the corrected redshift reported in the NASA/IPAC Extragalactic Database[2] (NED) is entirely cosmological in origin. The median error for SBF-derived $m - M$ gives ∼12% uncertainties in the corresponding D_L values. For the Hubble flow-derived distance moduli, the 7% uncertainties from redshift errors alone underestimates the true distance uncertainty.

[2] https://ned.ipac.caltech.edu/

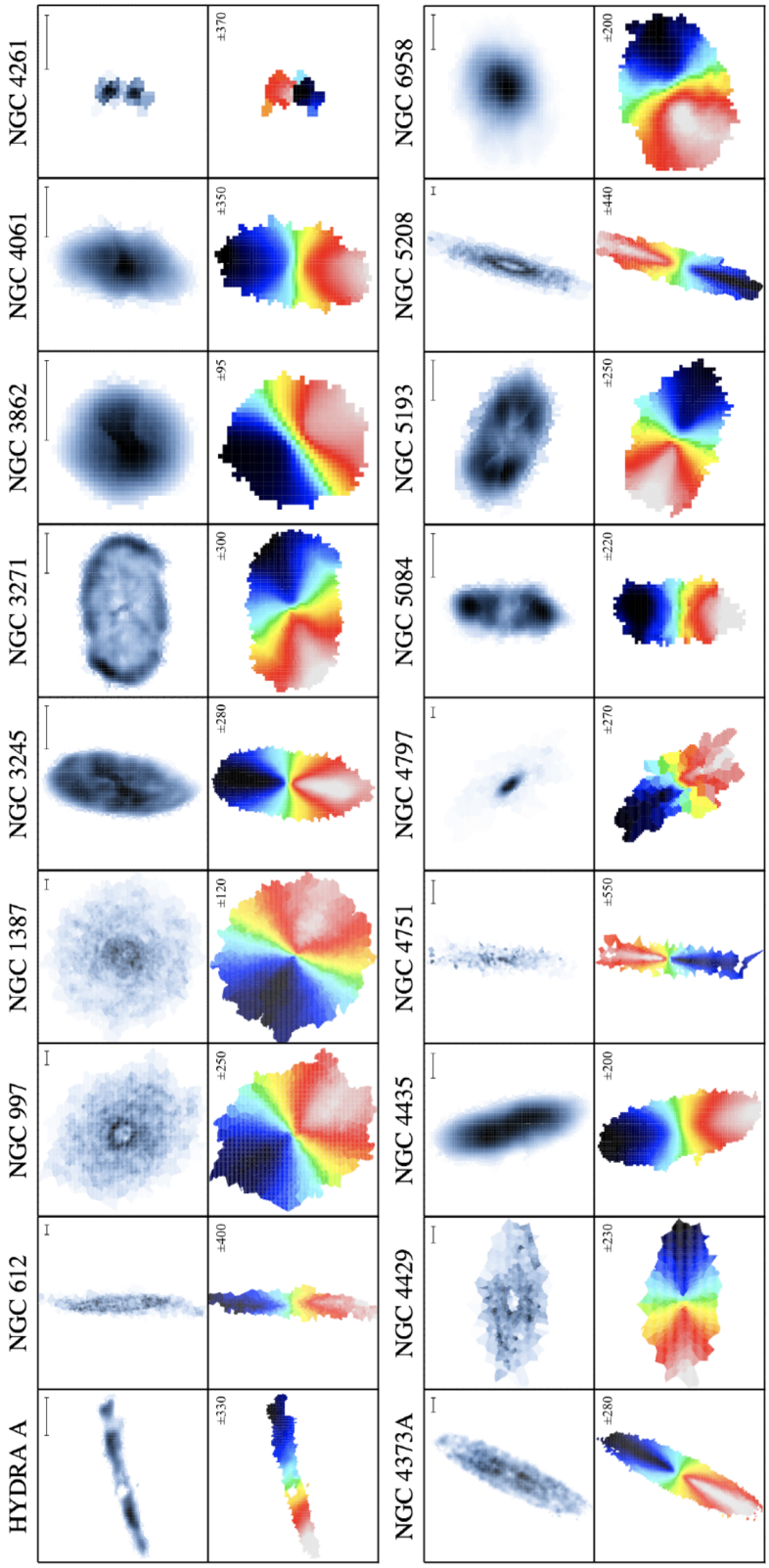

Figure 1.3 ALMA CO surface brightness (top) and luminosity-weighted line-of-sight velocity (bottom) maps for a subset of the full target list, which are amenable to gas-dynamical modeling and should permit moderate to tight constraints on the central BH mass. These disks show a wide range of CO morphologies, including ring-like cases and those that are more centrally concentrated. In every instance the CO gas exhibits regular, albeit at times somewhat warped, kinematics. The scale bar indicates an angular distance of 1 arcsec and applies to both the CO flux and velocity maps. In each velocity map frame, we report line-of-sight velocity ranges (in km s^{-1}) from the systemic value, which corresponds to the color scale extremes.

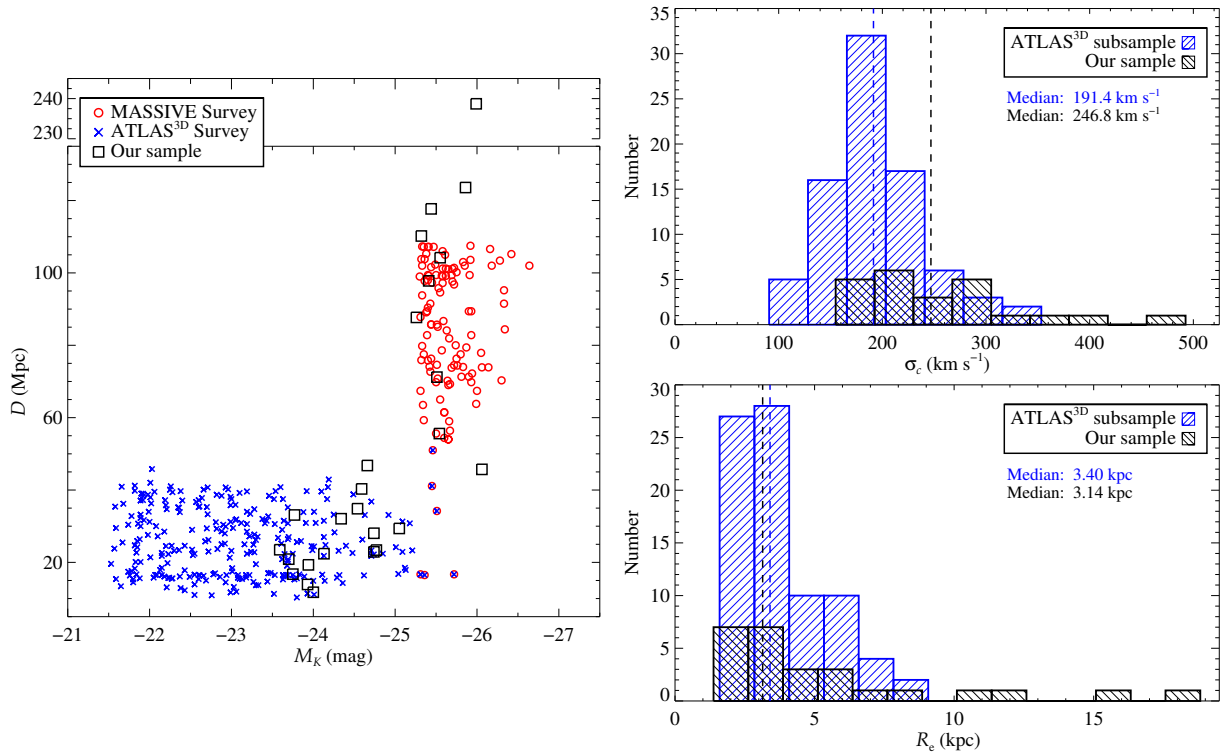

Figure 1.4 *Left panel:* Distance and absolute K-band magnitude of galaxies in our sample (black open squares) compared with values for two major ETG surveys – MASSIVE (red circles) and ATLAS^{3D} (blue crosses). Note that the y-axis is truncated from 135 to 235 Mpc to include Hydra A. *Right panels:* Comparison between a subsample of the ATLAS^{3D} survey (blue) and our sample (black) of the distribution of central velocity dispersion (σ_c; retrieved from the HyperLEDA database) and the effective radius (R_e). The ATLAS^{3D} subsample consists only of galaxies with equal or greater brightness than the dimmest galaxy in our sample ($M_K \leq -23.59$). The median σ_c and R_e values are printed and plotted (vertical dashed lines) for convenience. Even when compared to this subsample of brighter galaxies, our sample appears to be biased toward galaxies with a higher central velocity dispersion and slightly biased toward smaller effective radii.

We compare our final sample to two major volume-limited surveys of nearby ETGs: ATLAS^{3D} (Cappellari et al. 2011) and MASSIVE (Ma et al. 2014). Out of 260 ETGs, the ATLAS^{3D} survey is comprised of ∼26% elliptical and ∼74% lenticular galaxies. Out of 116 ETGs, the MASSIVE survey is comprised of ∼68% elliptical and ∼32% lenticular galaxies. Our final sample of 26 ETGs is comprised of ∼42% elliptical and ∼58% lenticular galaxies. We have six galaxies in common with the ATLAS^{3D} survey (NGC 3245, NGC 4261, NGC 4429, NGC 4435, NGC 4697, and NGC 5838) and three in common with the MASSIVE survey (NGC 997, NGC 3862, and NGC

5208). Figure 1.4 compares the distance and absolute K-band magnitude (M_K) of our sample with these ETG surveys. The galaxies in our sample appear to be, on average, more luminous than the ATLAS^{3D} galaxies and less luminous than the MASSIVE galaxies. Figure 1.4 also compares the distributions of central velocity dispersion and R_e of our sample with an ATLAS^{3D} subsample, which consists only of galaxies with equal or greater brightness than the dimmest galaxy in our sample ($M_K \leq -23.59$). Even when compared to this subsample of brighter ETGs, our sample appears to be biased toward galaxies with a higher central velocity dispersion and slightly biased toward galaxies with smaller R_e.

We note that 9 of the targets in our sample presently have published BH mass measurements or estimates (Barth et al. 2016a;b; Boizelle et al. 2019; 2021; Davis et al. 2017; 2018; Kabasares et al. 2022; Ruffa et al. 2019; 2023; Thater et al. 2022). For two of these ETGs – NGC 3258 and NGC 4261 – we have already analyzed the respective HST data (Boizelle et al. 2019; 2021). For uniformity, however, we include them for analysis using the same approach as is applied to the other HST data sets. In many cases, the stellar luminosity models constructed here will still be useful in any re-analysis of the ALMA CO data, or to better explore CND dust attenuation. Figure 1.5 shows a zoomed-in view of the CNDs for the entire sample, revealing the range of dust obscuration faced in this work.

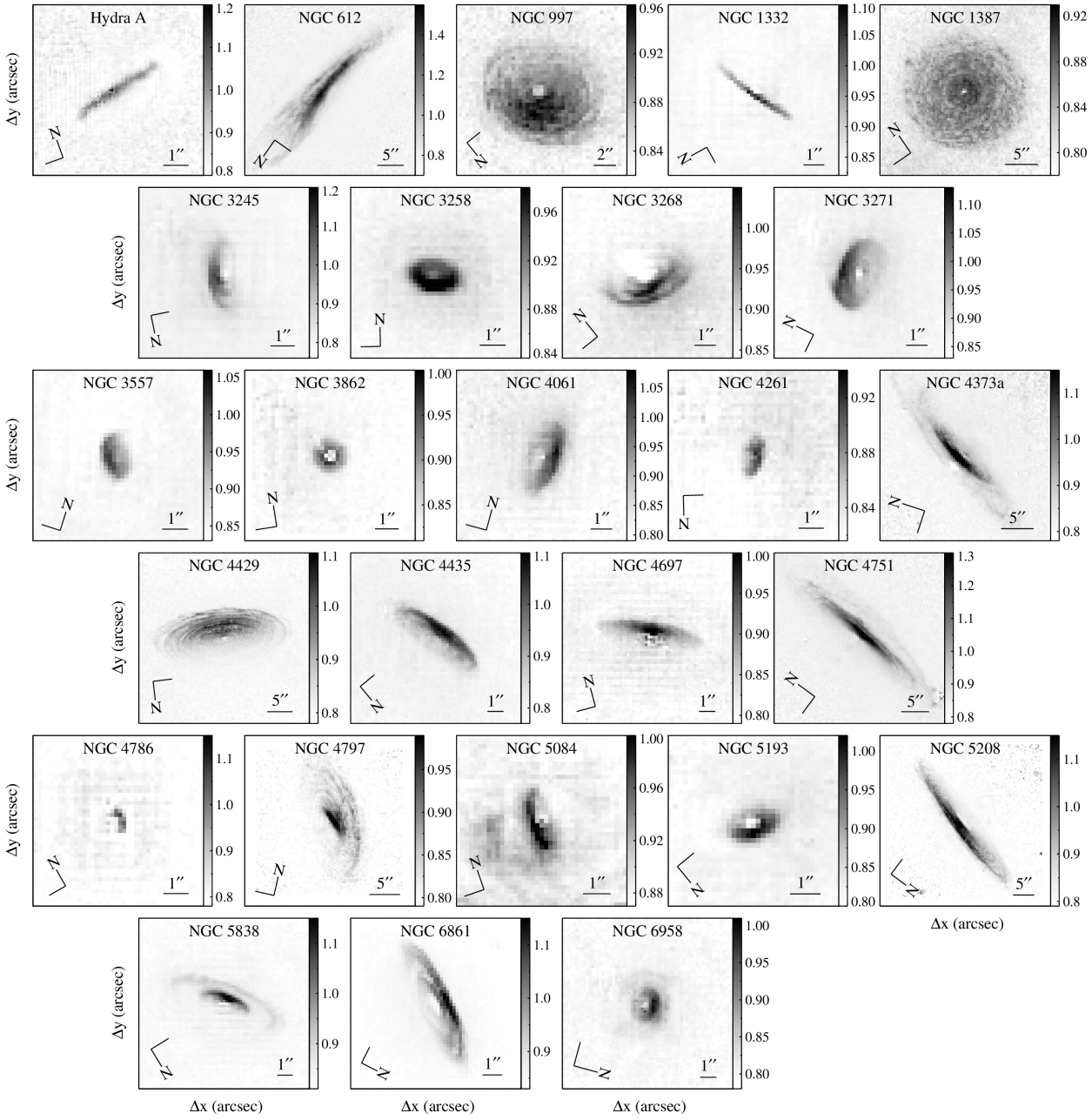

Figure 1.5 Sky-subtracted $J-H$ color maps for all 26 target galaxies, highlighting just the dusty disk regions. All images are shown using a linear intensity scale. The color values in each image are shown in their respective color bars.

Chapter 2

Methods

In this chapter we discuss the methods used for obtaining and reducing optical and near-IR HST data. In §2.1, we describe the HST (§2.1.1) observations used to measure the stellar surface brightness distributions for each ETG in our sample and the Spitzer Space Telescope (§2.1.2) observations to obtain a more accurate sky value for galaxies with more extended halos. Sky subtraction procedures to account for zodiacal light are also outlined in §2.1.2.

2.1 Optical/Near-Infrared Imaging

2.1.1 HST Imaging

Each ETG in this sample of 26 targets was observed in a single HST orbit during programs GO-14920, GO-15226, or GO-15909 (PIs: Boizelle). In all cases, data taken using the Wide Field Camera 3 (WFC3; Dressel 2022) IR detector mitigates dust attenuation from these CNDs. For just over half of these targets, we obtained additional WFC3/UVIS imaging to supplement previous optical HST imaging. Broad wavelength coverage is crucial when attempting to constrain dust attenuation, and from the B to the H bands the standard Galactic extinction law decreases by a

Table 2.1. New and Archival HST Observations

Galaxy Name	This Program[1] WFC3/IR	This Program[1] WFC3/UVIS	Other Programs WFPC2	Other Programs ACS	Other Programs WFC3/UVIS	GO ID
Hydra A	F110W, F160W	F475W	···	F814W	···	12220 (PI: Mittal)
NGC 612	F110W, F160W	F475W	···	F814W	···	15444 (PI: Barth)
NGC 997	F110W, F160W	F475W, F814W	···	···	···	···
NGC 1332	F110W, F160W	F438W	F814W	···	···	5999 (PI: Phillips)
NGC 1387	F110W, F160W	···	F606W	···	···	5446 (PI: Illingworth)
			···	F475W, F850LP	···	10217 (PI: Jordan)
NGC 3245	F110W, F160W	F475W	F547M	···	···	6837 (PI: Ho)
NGC 3258	F110W, F160W	···	···	F435W, F814W	···	9427 (PI: Harris)
NGC 3268	F110W, F160W	F555W	···	F435W, F814W	···	9427 (PI: Harris)
NGC 3271	F110W, F160W	F475W, F814W	···	···	···	···
NGC 3557	F110W, F160W	F438W	F555W	···	···	6587 (PI: Richstone)
NGC 3862	F110W, F160W	···	F547M, F791W	···	···	5927 (PI: Ford)
			F702W	···	···	9069 (PI: Biretta)
			···	···	F225W, F475W, F814W	14159 (PI: Meyer)
NGC 4061	F110W, F160W	F475W	F555W, F814W	···	···	9106 (PI: Richstone)
NGC 4261	F110W, F160W	···	F547M, F675W, F791W	···	···	5124 (PI: Ford)
			F702W	···	···	5476 (PI: Sparks)
			F450W, F606W, F814W	···	···	11339 (PI: Zezas)
NGC 4373a	F110W, F160W	F475W, F814W	···	···	···	···
NGC 4429	F110W, F160W	F475W, F814W	F606W	···	···	5446 (PI: Illingworth)
NGC 4435	F110W, F160W	···	F450W, F675W, F814W	···	···	6791 (PI: Kenney)
			···	F475W, F850LP	···	9401 (PI: Cote)
NGC 4697	F110W, F160W	F555W	···	F475W, F850LP	···	10003 (PI: Sarazin)
			···	···	F225W, F336W	11583 (PI: Bregman)
NGC 4751	F110W, F160W	F475W, F814W	···	···	···	···
NGC 4786	F110W, F160W	F438W	F555W	···	···	6587 (PI: Richstone)
NGC 4797	F110W, F160W	F475W, F814W	···	···	···	···
NGC 5084	F110W, F160W	F475W	···	···	···	···
NGC 5193	F110W, F160W	F475W	F814W	···	···	5910 (PI: Lauer)
NGC 5208	F110W, F160W	F475W, F814W	···	···	···	···
NGC 5838	F110W, F160W	F555W	F450W, F814W	···	···	7450 (PI: Peletier)
NGC 6861	F110W, F160W	F438W	F814W	···	···	5999 (PI: Phillips)
NGC 6958	F110W, F160W	F475W	F547M, F814W	···	···	8686 (PI: Goudfrooij)

Note. — Optical and near-IR medium and broadband-filter HST observations that provide good coverage and depth. New WFC3/IR and UVIS observations ([1]GO IDs: 14920, 15226, and 15909; PIs: Boizelle) supplement archival data sets that were obtained using the WFPC2, ACS, or WFC3/UVIS detectors, ensuring sufficient coverage and sampling for forthcoming dust attenuation modeling efforts. In cases where multiple HST observations exist at a given filter wavelength, we selected the observations that best covered the CND, preferring later-generation detectors while avoiding long exposures with saturated nuclei or containing too many cosmic rays over the CND.

factor of nearly 8. In Table 2.1, we detail these new WFC3 data, along with the archival Wide Field Planetary Camera 2 (WFPC2; McMaster & et al. 2008), Advanced Camera for Surveys (ACS; Ryon 2022), and WFC3 observations that were selected for this project to span the desired wavelength range.

New WFC3 Data

In the IR channel, we obtained both F110W and F160W (hereafter J and H) imaging for all targets. The primary focus was to construct a near-IR mosaic that samples the CND using a dither pattern while also probing well into the stellar halo. We employed a 4-point dither pattern for H-band observations with a pattern separation depending on the projected galaxy size. For targets where the galaxy is contained within the full-array WFC3/IR field-of-view (FOV), we adopted the 4-point WFC3-IR-DITHER-BOX-MIN pattern to more optimally sample the H-band point-spread function (PSF). For more extended galaxies, we employed a large square dither pattern with offsets of up to $75''$ and total coverage up to $3.6' \times 3.6'$. The stellar halos of several targets span a much larger angular diameter, but larger-scale mosaicing would have resulted in additional overheads. This larger-scale mosaicing placed the central bright region of each galaxy within the overlap region between all four pointings. In most cases, these WFC3/IR mosaics extend out to a few $\times R_{\rm e}$, where $R_{\rm e}$ has been measured from our stellar luminosity models, as is described in §3.2. Individual H-band exposure times ranged from 250 to 400 s, using various SPARS or STEP sampling sequences (SAMP-SEQ) to avoid time loss due to buffer dumps. Each MULTIACCUM image used NSTEP = 9 or higher to enable good up-the-ramp calibration and cosmic-ray rejection. The combined data reached the background limited sensitivity for this filter in the overlap regions.

For filters bluer than H, only the central region containing the CND is crucial to this project. Therefore, we adapted the observational setup for the remaining new HST imaging to fit into a single orbit. This adaptation included a smaller number of dithers and/or the use of a sub-array aperture to avoid costly buffer dumps.

We generally obtained the J-band data using the IRSUB512-FIX sub-array aperture, employing the 2-point WFC3-IR-DITHER-LINE pattern to better sample the PSF. This aperture gives a FOV of about $60'' \times 60''$. In a few cases, the available optical data and orbit constraints allowed for full-aperture J-band imaging. Sampling sequences for the J-band observations were similar to

those employed in acquiring the *H*-band data. While individual exposure times generally ranged from only 100 to 200 s, the combined exposure time matched (or exceeded) the optimal value for background-limited imaging in this filter.

Two cases with extended stellar light – NGC 3862 and NGC 4261 – host AGN that are more prominent in the optical. Since these ETGs already had sufficient optical coverage, we obtained more *J* and *H*-band imaging of these galaxy nuclei to facilitate better characterization of the near-IR point source. These additional data were taken using the IRSUB256-FIX aperture and the ideal 4-point dither pattern, with the SPARS5 / NSAMP = 15 combination for rapid temporal sampling (see Figure 2.1). For these shorter data sets, the total MULTIACCUM exposure time at an individual pointing was just 33 s.

For over 80% of this sample, new WFC3/UVIS data was justified to supplement existing HST optical data. Selections ensured coverage in broadband filters in the *B* and *I*-band regimes. At the blue end, we obtained new WFC3/UVIS imaging using either the F438W or F475W filter, depending on the program. At the red end, we chose the F814W filter. In a few cases, orbit scheduling also allowed for F555W imaging for more complete wavelength sampling. To allow all data to be scheduled in a single orbit, we chose either the UVIS1-2K2A-SUB or UVIS2-M1K1C-SUB apertures that were centered on these CNDs. Exposure lengths for individual frames ranged from 150 to 400 s depending on the remaining time available in the orbit. To limit the impact of cosmic rays, observations in a single filter were split into either 2 or 3 frames and dithered using the corresponding WFC3-UVIS-DITHER-LINE pattern.

Archival Data

We retrieved ACS, WFC3, and WFPC2 optical (and occasionally UV) images of our target galaxies from the Mikulski Archive for Space Telescopes[1] (MAST). Imaging was selected to ensure good

[1] https://archive.stsci.edu/hst

coverage of the galaxy's CND. Additional criteria included employing only medium or broadband filters to avoid possible contamination from emission lines, requiring good image quality (e.g., low incidence of cosmic rays overlapping with the CND, and an unsaturated nucleus). In cases with more than one imaging set in a filter or similar wavelength range, consideration was given to data sets with the best angular resolution or most clear recovery of the CND structure. We note that the HST archive contains additional NICMOS imaging in a range of near-IR filters for some galaxies in our sample, even in redder filters than F160W. Due to the limited FOV and calibration issues towards that instrument's edges, however, we decided to not include any NICMOS products in our analysis.

Calibration and Analysis

After processing these new data through the `CALWF3` pipeline, we created final H-band mosaics and B, I, and J subarray products using `AstroDrizzle` (Gonzaga et al. 2012). All WFC3 images were drizzled successfully using the `PyRAF` (Science Software Branch at STScI 2012) version (see Figure 2.1). However, errors arose when trying to drizzle the WFPC2 and ACS images, which necessitated the use of the `astropy` (Astropy Collaboration et al. 2018) version instead. Following the methodology in the DrizzlePac handbook[2] (Gonzaga et al. 2012) for drizzling WFPC2 images, we applied the same procedures to the ACS images, i.e., we updated their WCS coordinates and then successfully equalized and drizzled the images. The WFPC2 images required a more time-consuming process. Despite following the procedures as outlined, we were unable to successfully update the WCS coordinates of, and consequently unable to drizzle, the WFPC2 images. We eventually learned that the problem stemmed from the calibration frames, specifically that we lacked all the necessary files. To ensure there would be no further issues, we retrieved *all* the calibration frames for each set of WFPC2 observations from the HST archive. Once done, we successfully

[2]The tutorial we followed can be found here.

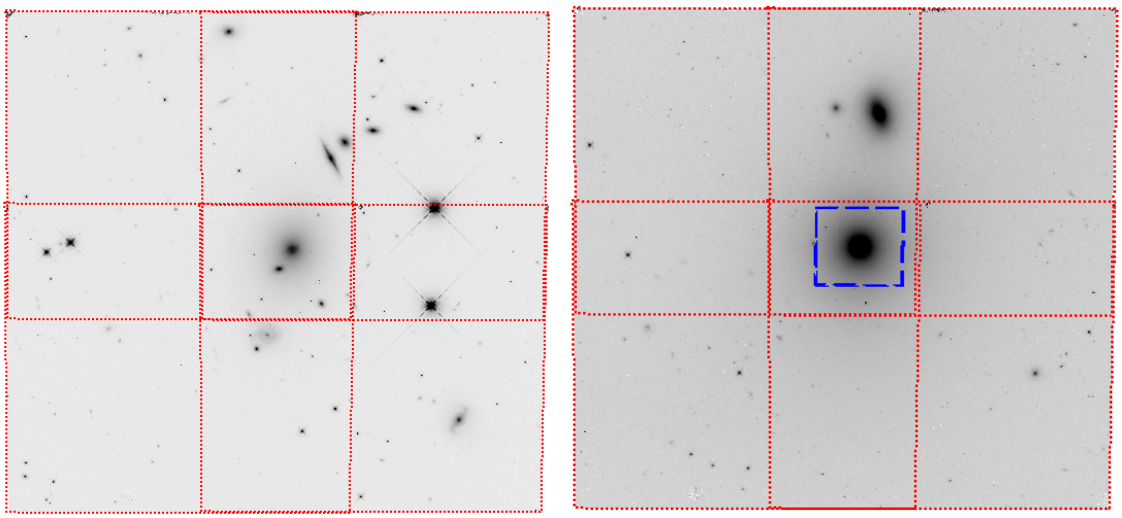

Figure 2.1 Large-scale H-band mosaics for Hydra A (*left*) and NGC 3862 (*right*). The red dashed-line boxes demonstrate the pointing overlap for the dithered HST images before being drizzled into a single mosaic. Though less visible, the blue dashed-line boxes indicate the smaller, ideal dither pattern used in the case of NGC 1387, NGC 3862, NGC 4261, and NGC 4435.

updated the WCS coordinates and equalized and drizzled the images.

All images were drizzled to the same pixel scale of $0.08''$ pixel^{-1} to facilitate our goal of constraining dust extinction on a pixel-by-pixel basis. For the dithered WFC3/IR data, we adopted a pixel fraction of 0.75 to better sample the PSF. Since the WFC3/UVIS data had smaller detector pixel sizes but less ideal dithering, we used the same pixel fraction. In general, these WFC3 data obtained in a single orbit remain well aligned after drizzling. In Figure 2.2, we show examples of these H-band mosaics and the HST footprint together with larger-scale near-IR imaging.

Preliminary mosaicing of the archival HST data did not align well with the new WFC3 data, so we first aligned the pipeline-calibrated files to the H-band mosaic using `TweakReg`. Then, we combined the single-filter data in `AstroDrizzle` using the same pixel scale and fraction as chosen for the WFC3/IR imaging. The accuracy of dust attenuation modeling is very sensitive to the relative (sub-pixel) alignment of data across all filters. Slight offsets between different filters were still present, so to further improve the alignment of the HST data for each target, we calculated a luminosity-weighted centroid using a series of stellar isophotes that were measured beyond the dusty

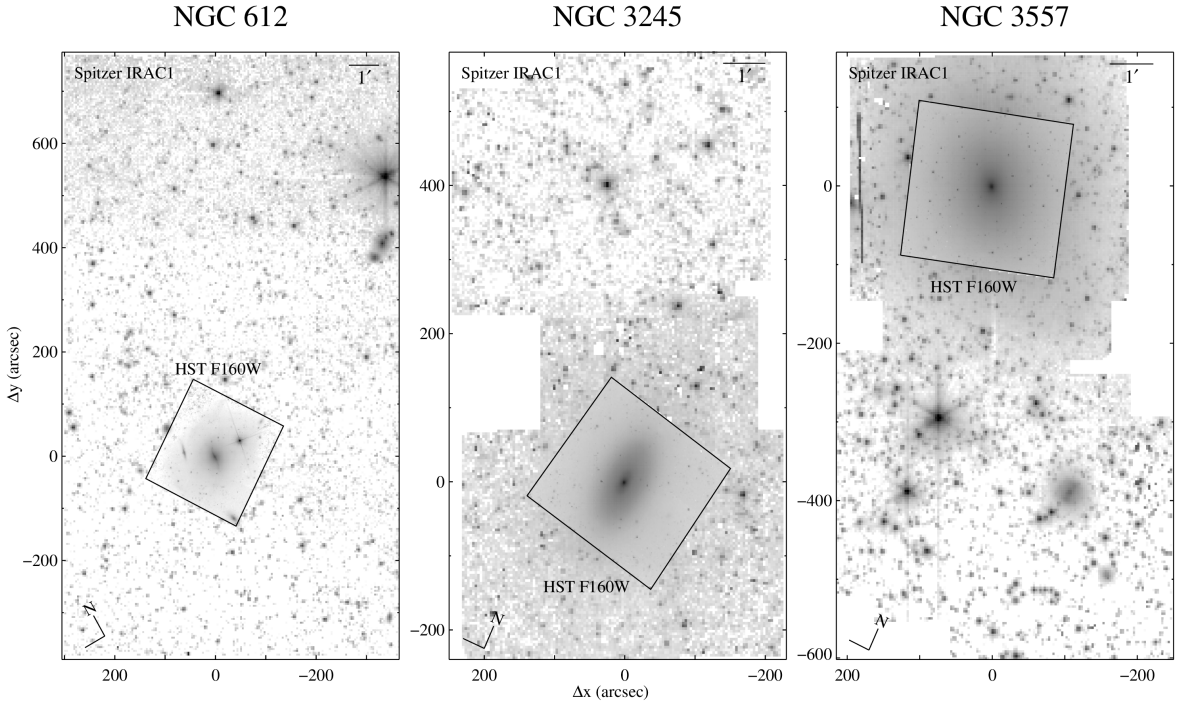

Figure 2.2 HST WFC3 F160W drizzled mosaics overlaid on Spitzer IRAC1 (3.6 μm) supermosaics, with the IRAC1 surface brightnesses scaled to match the sky-subtracted H-band surface brightnesses at the edge of the HST footprint. These three targets were selected to highlight the diversity of stellar halo angular extents and the challenges in accurately subtracting the H-band sky background for most of the sample. All images are shown using a logarithmic intensity scale and the scalebar demarcates 1 arcmin. The entirety of the Spitzer supermosaics are shown for NGC 3245 and NGC 3557; for NGC 612, the large-scale imaging was cropped for convenience and better visibility of the HST F160W image.

features of the CND. Afterwards, we removed the offsets of the lower-wavelength data relative to the H-band mosaic using spline interpolation. Finally, we confirmed the accuracy of these sub-pixel offsets (or introduced additional fine tuning) by inspecting the resulting color maps. In Figure 2.3, we show an example of the alignment of these multi-wavelength images for a single target.

Intrinsic stellar luminosity models described in §3.2 require a prescription for the point spread function (PSF) in the corresponding filter. Following standard practice, we created model H-band PSFs for each target by dithering and drizzling copies of the Tiny Tim (Krist & Hook 2004) F160W response in an identical manner as were the HST data (see Figure 2.4). We note that the dithering and drizzling process does help to obtain a larger full width at half maximum (FWHM) than usual,

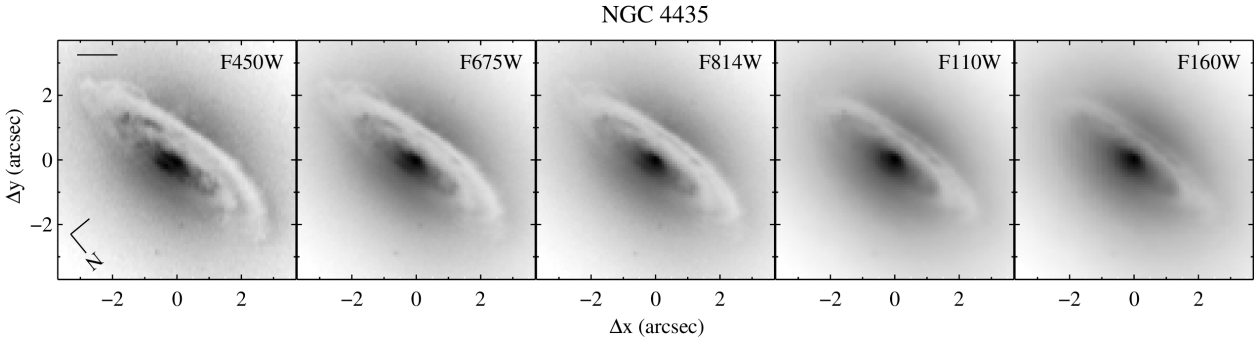

Figure 2.3 Aligned HST images showing NGC 4435 in five different filters, highlighting just the dusty disk region in an inverted grayscale. The scale bar demarcates 100 pc. Going from bluer to redder filters, the more diffuse dust towards the disk outskirts (at $R \sim 3.5''$) becomes less apparent while the more dense dust towards the center (at $R \sim 2''$) becomes more distinct. Additional details on the relevant detectors are found in Table 2.1.

but the theoretical PSF still shows a somewhat more narrow FWHM ($\sim 0.19''$ on average) than is observed for foreground stars in each H-band mosaic (generally $\sim 0.24''$). An alternative approach is to employ an empirical PSF, and we find somewhat better agreement of these PSFs ($\sim 0.20''$ on average) with the observed stellar FWHM for our data. Previous work by Zhao et al. (2021) explored the differences between using a Tiny Tim WFC3 PSF and an empirical WFC3 PSF derived from stars extracted from archival images, in the context of quasar host galaxy studies. They found that an empirical PSF is undoubtedly better, though extraction of a PSF from a suitable star is not always possible and timing and/or field variation effects can make constructing a proper empirical PSF nontrivial. For our targets, bright foreground stars are not always seen near each galaxy center, so we constructed a second model PSF by relying on the empirical WFC3/IR F160W PSF provided by STScI[3], again dithering and drizzling copies of this frame in the same manner as done for the Tiny Tim files (see Figure 2.4). For the sake of simplicity, we include only the analysis using Tiny Tim PSFs in this paper, with the exception of one representative target. For NGC 3862, we present a comparison of the stellar luminosity models constructed using both a theoretical and an empirical PSF in Section 3.2.1.

[3]The STScI WFC3 empirical PSF can be found at https://www.stsci.edu/hst/instrumentation/wfc3/data-analysis/psf.

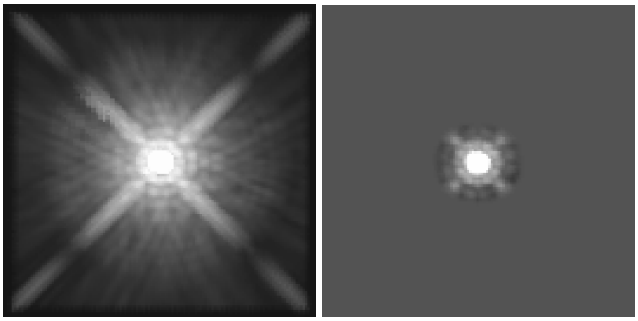

Figure 2.4 Side-by-side look at the 2D Tiny Tim (*left*) and the empirical (*right*) PSF, displayed to the same spatial extent. Both sets of PSFs were constructed identically to the HST data, including dithering and drizzling. The empirical PSF was provided by STScI. A comparison of the effects of using the Tiny Tim versus the empirical PSF is presented in §3.2.1.

Careful analysis of a galaxy's surface brightness distribution necessitates removing or masking out contaminants. To isolate our target galaxies, we masked out all other galaxies, foreground stars and diffraction spikes, detector artifacts, and cosmic ray-affected pixels. At small radii, we created a second pixel mask that included the worst of the dust obscuration. To constrain the central surface brightness profile with the least possible obscuration, we created an additional mask for each CND. These dust masks, seen in Figures 2.5 and 2.6 for CNDs with a range of angular sizes, nearly always contain the entire near side of the disk and typically include pixels with $J-H \gtrsim 0.88$ mag [or an intrinsic color excess $\Delta(J-H) \gtrsim 0.08$ mag from the observed stellar colors just outside the CND]. The reason for this choice in color cutoff can be seen in Figure 1.5, which shows sky-subtracted $J-H$ color maps highlighting just the CND region of all our target galaxies, and Figure 2.7, which shows the sky-subtracted $J-H$ and $\Delta(J-H)$ color as a function of radius for the entire sample — to ensure that we remove the worst of the dust obscuration while also maintaining a reasonable standard between the variety of CNDs in our sample.

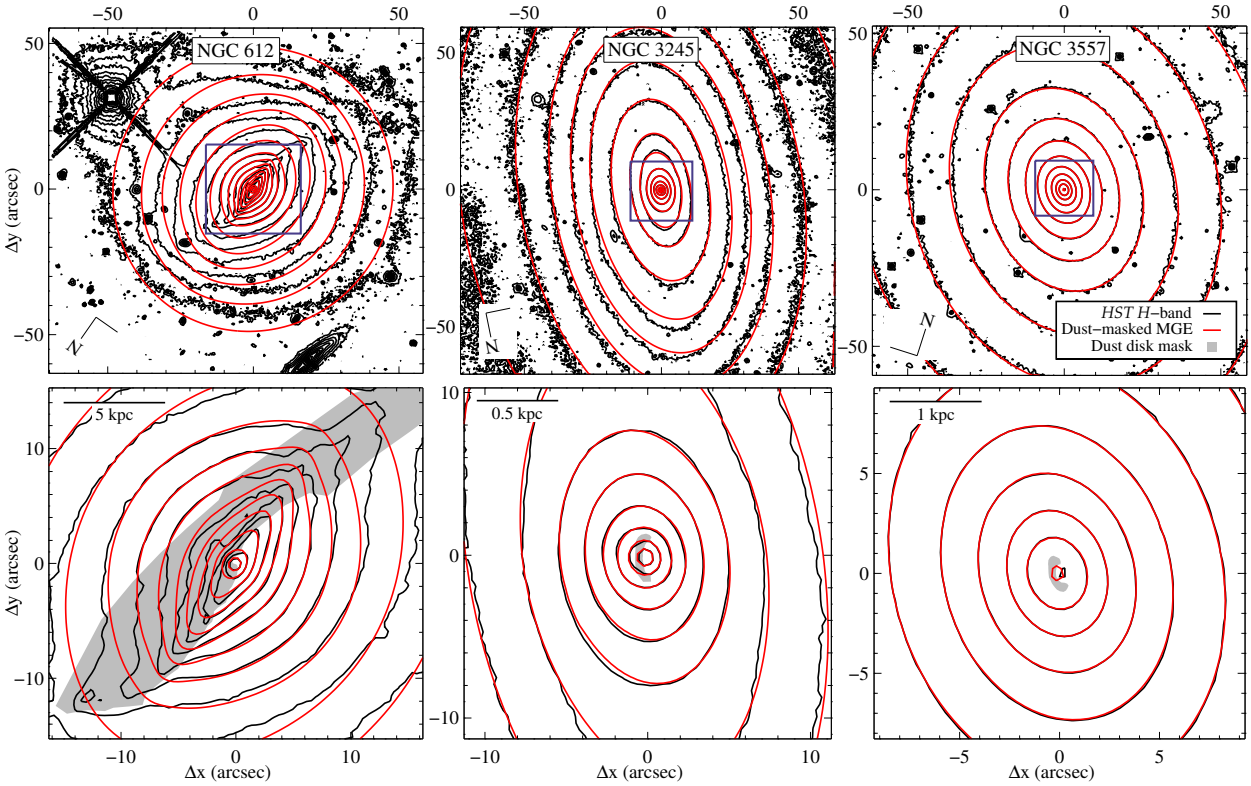

Figure 2.5 HST WFC3 F160W drizzled mosaics for the same set of targets as shown in Figure 2.2, NGC 612, NGC 3245, and NGC 3557. On top of the nearly full-frame sky-subtracted data (*top panels*) is a box that defines the zoom-in region (*bottom panels*). These data are shown using contours that are logarithmically spaced to highlight the range of features. The best-fitting `GALFIT` MGE solutions are overplotted (in red), showing general good agreement with the data in the central zoom-in plots. At larger radii, stellar isophotal PA twists result in larger but unavoidable discrepancies. In the zoom-in panels, shaded regions show masked portions of each CND based on high $J-H$ color (see Figure 1.5), removing from the MGE fit the most dust-obscured pixels that are typically found on the near side of the disk.

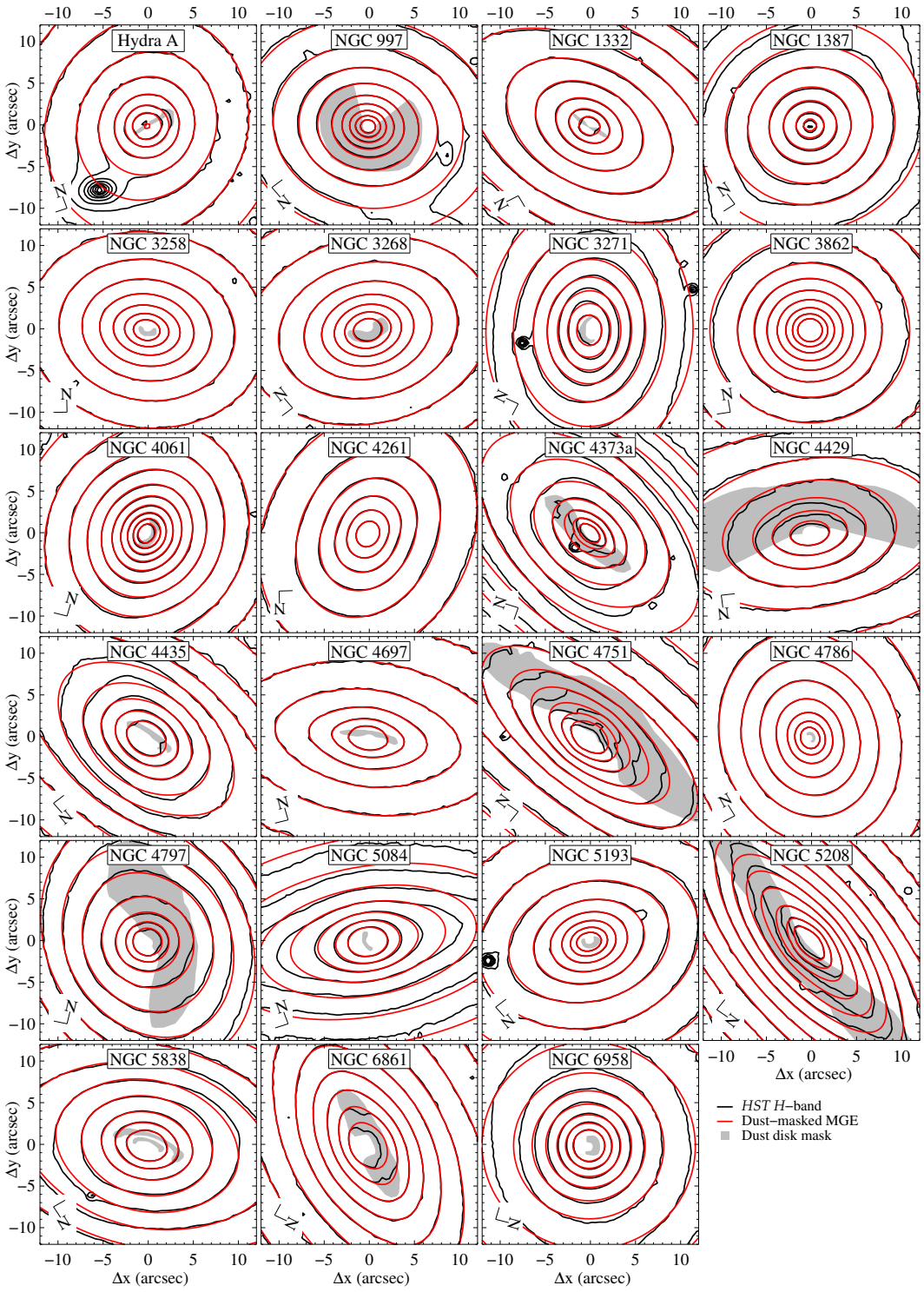

Figure 2.6 Zoomed-in HST WFC3 F160W drizzled mosaics for targets not shown in Figure 2.5. Sky-subtracted data are shown using contours that are logarithmically spaced to highlight the range of features. The best-fitting `GALFIT` MGE solutions are overplotted (in red). Shaded regions show masked portions of each CND based on high $J-H$ color (see Figure 1.5), removing from the MGE fit the most dust-obscured pixels that are typcially found on the near side of the disk. Note that the CNDs of NGC 1387, NGC 3862, and NGC 4261 were left unmasked because they are not readily visible in the H-band images due to small inclination angles and/or low intrinsic extinction.

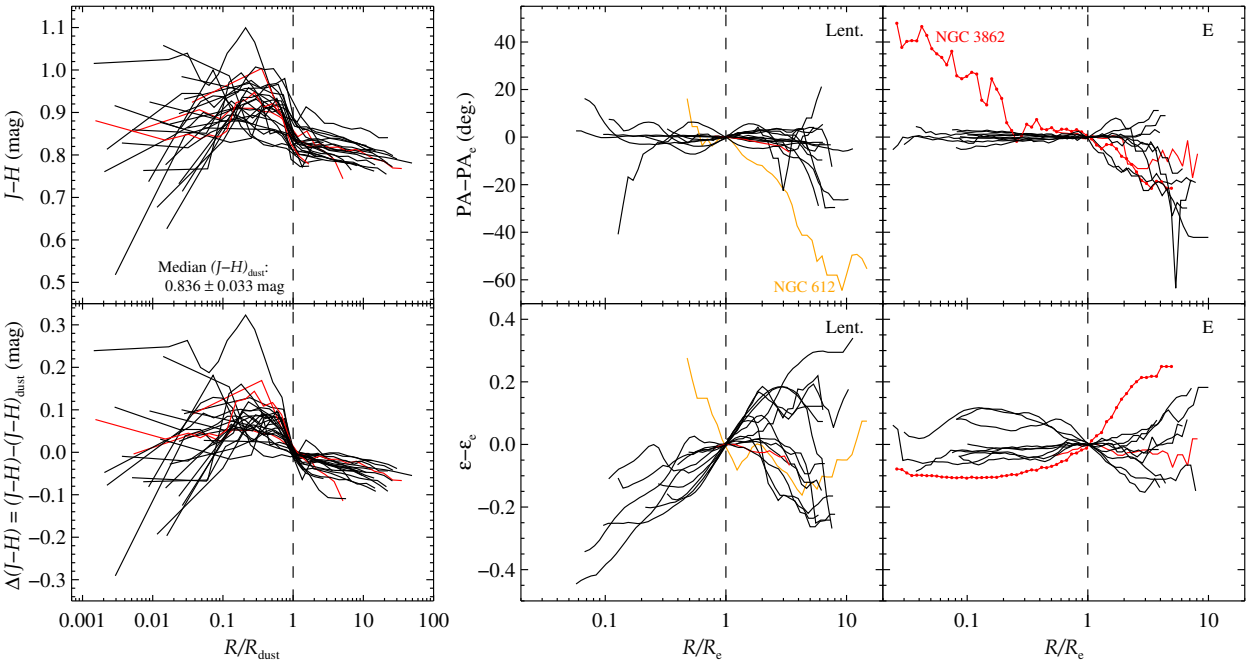

Figure 2.7 *Top left panel:* Sky-subtracted $J-H$ color as a function of radius, normalized to the dust disk influence. The dust disk influence was determined based on the slope of the color curve near the dust disk radius in the H-band ($R_{\mathrm{dust},H}$, i.e., the dust disk radii reported in Table 2.2), such that R_{dust} here now equals $R_{\mathrm{dust,\,infl.}}$ which ranged from $R_{\mathrm{dust},H}$ to $1.2\,R_{\mathrm{dust},H}$. *Bottom left panel*: $(J-H)-(J-H)_{\mathrm{dust}}$ color, where $(J-H)_{\mathrm{dust}}$ is the color measured at the dust disk influence for each target, as a function of radius, also normalized to the dust disk influence. The color data for both of these panels was adjusted as previously described and binned to better show the overall trends of the color curves. The median color measured at R_{dust} is also reported. *Right panels:* PA$-$PA$_{\mathrm{e}}$ (*top*) and $\varepsilon-\varepsilon_{\mathrm{e}}$ (*bottom*) as a function of radius from the dust disk influence outward, where PA$_{\mathrm{e}}$ and ε_{e} are the PA and ε measured at R_{e}, respectively. The only exception is NGC 612 (shown in orange), whose R_{dust} is larger than its R_{e}, in which case we plot it from $\sim 0.5\,R_{\mathrm{e}}$ outward. These plots are also normalized by R_{e} and separated by galaxy type. For all data shown here, those in red are the galaxies our sample has in common with the MASSIVE survey.

2.1.2 Spitzer Imaging and Sky Subtraction

Based on an initial analysis of the surface brightness profiles, we identified 17 galaxies (see Table 2.2) whose H-band stellar light contributions near the edges of the HST footprint were at the same level as the expected background level (primarily zodiacal in origin; Pirzkal 2014), as estimated using the WFC3/IR Exposure Time Calculator[4] (ETC) for the corresponding solar angles for those images. Such a high level of stellar light that persists out to a projected $R \sim 2'$ from the nucleus or beyond prevents confident sky subtraction, at least without making assumptions about the surface brightness slopes.

To avoid unnecessary assumptions and to extend surface brightness profiles for our sample galaxies, we directly fit for the sky background by comparison to larger-scale Spitzer IRAC channel 1 (3.6 μm) data. We retrieve these IRAC supermosaics from the Spitzer Heritage Archive[5]. Prior to extracting surface brightness profiles along a common direction for both the HST H-band and Spitzer data, we masked galaxies and foreground stars in the relevant portions of the IRAC frames. Additionally, we masked some noisy regions at the edges of the Spitzer supermosaics and at the overlap of detector pointings.

For the 17 galaxies with more extended stellar distributions on the sky, we extracted H-band and IRAC1 surface brightness profiles in the same direction towards the corner of the HST mosaic. Following the method outlined by Boizelle et al. (2019), we used overlapping measurements to simultaneously determine both the $H-$IRAC1 color and the H-band sky background, generally between $R \sim 20-70''$ where color gradients tend to be mild (see Figure 2.8 for an example). As reported in Table 2.2, these sky values are mostly consistent with expected ETC values for the Sun angles at the time of observation. For the remaining 9 galaxies, whose stellar light distributions are well contained within the H-band mosaic, we determined (and removed) the sky background using

[4] https://etc.stsci.edu/etc/input/wfc3ir/imaging/

[5] https://irsa.ipac.caltech.edu//onlinehelp/heritage/#about

corner regions of the dithered footprint.

It was also necessary to determine and remove the J-band sky background. We estimated the J-band sky values based on the WFC3/IR ETC, except for a few cases where the J-band footprint covered out far enough to estimate the background independently. Sky values were chosen to ensure a smooth color gradient between the dust disk extent and the outer portion of the J-band mosaics. Because of the smaller FOV, not all J-band mosaics probed out to the H-band $R_{\rm e}$.

Table 2.2. CND Properties, Isophotal Analysis, and Spitzer Scaling Results

Galaxy Name (1)	$R_{\rm dust}$ (kpc) (2)	$(b/a)_{\rm dust}$ (arcsec) (3)	$PA_{\rm dust}$ (deg.) (4)	$\overline{PA}_{\star,\rm phot}$ (deg.) (5)	$\Delta PA_{\star,\rm phot}$ (deg.) (6)	$\Delta\varepsilon$ (7)	median a_4/a (8)	min,max a_4/a (9)	sky_H (e s^{-1} $arcsec^{-2}$) (10)	$H-$IRAC1 (mag) (11)	∇_{J-H} (mag) (12)
Hydra A	2.03	0.27 / 1.96	−75.3	-36.0	41.2	0.304	−0.006	−0.101, 0.003	32.81	···	-0.024
NGC 612	10.8	2.90 / 19.1	−11.0	-15.4	46.8	0.198	0.014	−0.023, 0.046	31.15	2.26	-0.027
NGC 997	2.32	4.69 / 5.70	32.6	29.7	11.0	0.034	−0.006	−0.043, −0.002	43.75	···	-0.103
NGC 1332	0.24	0.17 / 2.17	114.9	116.7	3.4	0.445	−0.007	−0.014, 0.005	35.93	2.12	-0.031
NGC 1387	0.88	8.35 / 9.43	52.1	108.7	54.5	0.296	−0.001	−0.015, 0.006	40.41	2.22	-0.024
NGC 3245	0.16	0.59 / 1.60	−6.9	-3.4	19.7	0.367	0.001	−0.091, 0.024	71.66	2.65	-0.054
NGC 3258	0.15	0.58 / 0.99	75.0	76.3	21.3	0.188	−0.001	−0.009, 0.031	45.52	2.66	-0.071
NGC 3268	0.40	1.27 / 2.40	−108.6	-112.1	7.4	0.097	0.001	−0.002, 0.007	33.35	2.20	-0.044
NGC 3271	0.46	1.04 / 1.74	−86.1	-66.9	33.7	0.280	−0.003	−0.035, 0.043	28.13	···	-0.058
NGC 3557	0.22	0.62 / 0.99	36.2	33.4	7.7	0.122	0.002	−0.006, 0.011	56.51	2.20	-0.025
NGC 3862	0.38	0.80 / 0.84	−9.0	-16.0	62.7	0.344	0.002	−0.019, 0.015	38.82	2.27	-0.046
NGC 4061	0.92	0.93 / 1.81	−6.2	-5.6	28.1	0.084	−0.006	−0.076, 0.027	39.06	···	-0.063
NGC 4261	0.13	0.51 / 0.89	−16.4	-22.3	13.9	0.137	−0.002	−0.014, 0.005	45.25	2.20	-0.024
NGC 4373a	0.95	2.17 / 6.00	−26.0	-32.4	9.7	0.404	0.003	−0.010, 0.030	28.13	···	-0.123
NGC 4429	0.90	5.62 / 13.5	90.3	94.4	11.5	0.248	0.004	−0.013, 0.043	43.30	2.15	-0.021
NGC 4435	0.25	0.86 / 3.07	13.8	6.3	28.8	0.273	0.002	−0.018, 0.054	42.22	2.13	-0.042
NGC 4697	0.20	0.95 / 3.48	65.3	66.0	2.3	0.142	−0.003	−0.010, 0.003	51.50	2.13	-0.034
NGC 4751	1.54	3.22 / 13.7	−5.1	-4.9	5.2	0.102	−0.003	−0.031, 0.008	26.56	···	-0.157
NGC 4786	0.19	0.32 / 0.57	−13.1	-17.0	13.1	0.105	0.002	−0.011, 0.033	40.66	2.20	-0.025
NGC 4797	5.72	4.64 / 10.6	22.8	31.0	17.8	0.219	0.001	−0.013, 0.024	32.81	···	-0.069
NGC 5084	0.13	0.44 / 1.18	−2.0	82.8	5.7	0.449	−0.002	−0.016, 0.006	48.44	2.13	-0.023
NGC 5193	0.21	0.60 / 0.96	64.7	70.8	46.1	0.196	0.005	−0.031, 0.047	68.75	···	-0.036
NGC 5208	8.70	3.42 / 18.1	−17.7	-17.1	6.2	0.050	−0.006	−0.008, 0.036	34.38	···	-0.083
NGC 5838	0.45	1.70 / 4.15	36.8	47.4	11.9	0.464	−0.004	−0.023, 0.007	49.79	2.18	-0.080
NGC 6861	1.01	1.92 / 7.60	−37.9	-38.0	25.7	0.224	0.002	−0.002, 0.038	39.69	2.19	-0.078
NGC 6958	0.25	1.15 / 1.29	105.5	109.7	43.7	0.225	−0.001	−0.024, 0.050	74.59	2.25	-0.059

Note. — Measured properties of the CNDs and results from an isophotal analysis applied to the H-band mosaics. Col. (2), (3), and (4) report the dust disk radius (in kpc), the measured minor and major axis (in arcseconds), and the position angle of the dusty circumnuclear disk, respectively, as observed and estimated by eye in IR HST imaging. While the full isophotal results are shown in Figure 3.1 and in the Appendix, col. (5), (6), and (7) give the average stellar photometric PA, the degree of isophotal twisting ($\Delta PA_{\star,\rm phot}$), and $\Delta\varepsilon$ values. The average stellar photometric PA was calculated using Equation 3.1, between $R_{\rm dust}$ and $R_{\rm e}$, with the exception of NGC 612 and NGC 4797, calculated between $R_{\rm dust}$ and $3R_{\rm e}$ and $1.5R_{\rm e}$, respectively. The ΔPA and $\Delta\varepsilon$ values were calculated using Equations 3.2, and 3.3, as measured from just beyond the outer edge of the dust disk to near the edge of the H-band mosaic. Col. (8) and (9) report the median and range of a_4/a parameters. To this table are added the sky backgrounds in col. (10), which were determined by splicing together the H-band+IRAC1 data. For those with more extended stellar halos, col. (11) gives the color term needed to scale the IRAC1 surface brightness profiles to match the H-band data. Col. (12) reports the $J-H$ color gradient calculated using the formula $\nabla_{J-H} = d(J-H)/d(\log\rho)$ (La Barbera et al. 2010), where ρ is the unitless distance to the galaxy center $R/R_{\rm e}$. Each color profile was fitted in the radial range of $\rho_{\rm min} = R_{\rm dust}$ to $\rho_{\rm max} = 2R_{\rm e}$, except for NGC 612, in which case the radial range was extended to $3.5R_{\rm e}$.

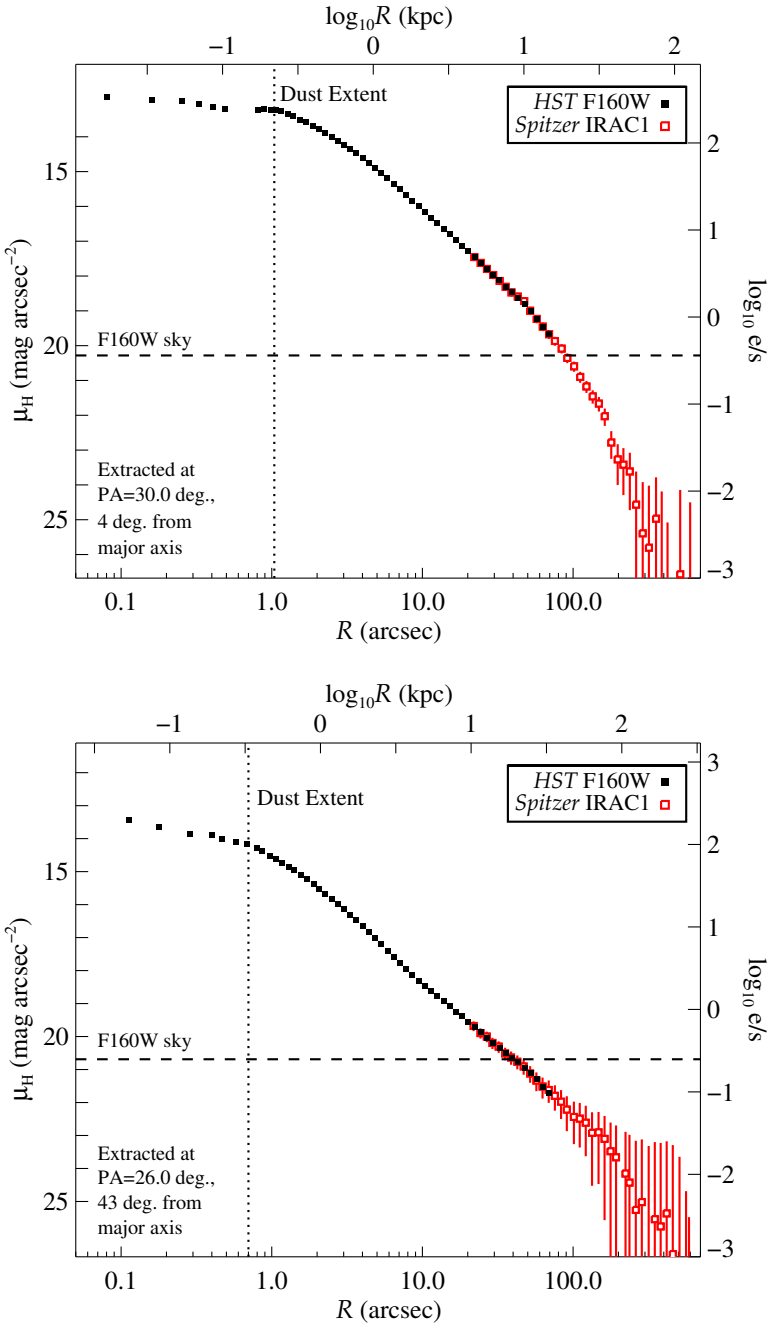

Figure 2.8 *Top:* Example of using Spitzer IRAC1 (3.6 μm) data to extract a more accurate H-band sky background for NGC 3557. *Bottom:* Example of a galaxy, NGC 3862, that did not (much) need the large-scale Spitzer imaging to get the sky background. The surface brightness was measured from the HST H-band image (in black), with Spitzer data (in red) spliced in at radii beyond 20″.

Chapter 3

Results and Conclusions

In §3.1, we present the results of an isophotal analysis of the HST data. §3.2 details the construction of stellar luminosity profiles using the multi-Gaussian expansion formalism and §3.2.1 presents a comparison of the effects of using a theoretical versus an empirical PSF. In §3.3, we discuss the goodness of fit (§3.3.1), additional challenges in constructing the models (§3.3.2), the consistency of the solutions (§3.3.3), the circular velocity curves of the sample (§3.3.4), and some current gas-dynamical modeling efforts that have made use of some of the multi-Gaussian expansion models in this work (§3.3.5). In §3.4, we discuss future dust attenuation modeling efforts. We conclude in §3.5.

3.1 Isophotal Analysis

Final masks for each galaxy, including the masked portions of each CND (where relevant; see Figure 2.6), were passed into the `IRAF` (Tody 1986; 1993) task `badpiximage` to create bad pixel maps. After removing the background level from the target images, the bad pixel maps and sky-subtracted images were used as inputs to the `IRAF` `ellipse` task, which returns the intensity, position angle (PA), ellipticity (ε), and deviation from a true ellipse (a_4/a) parameter at logarithmically

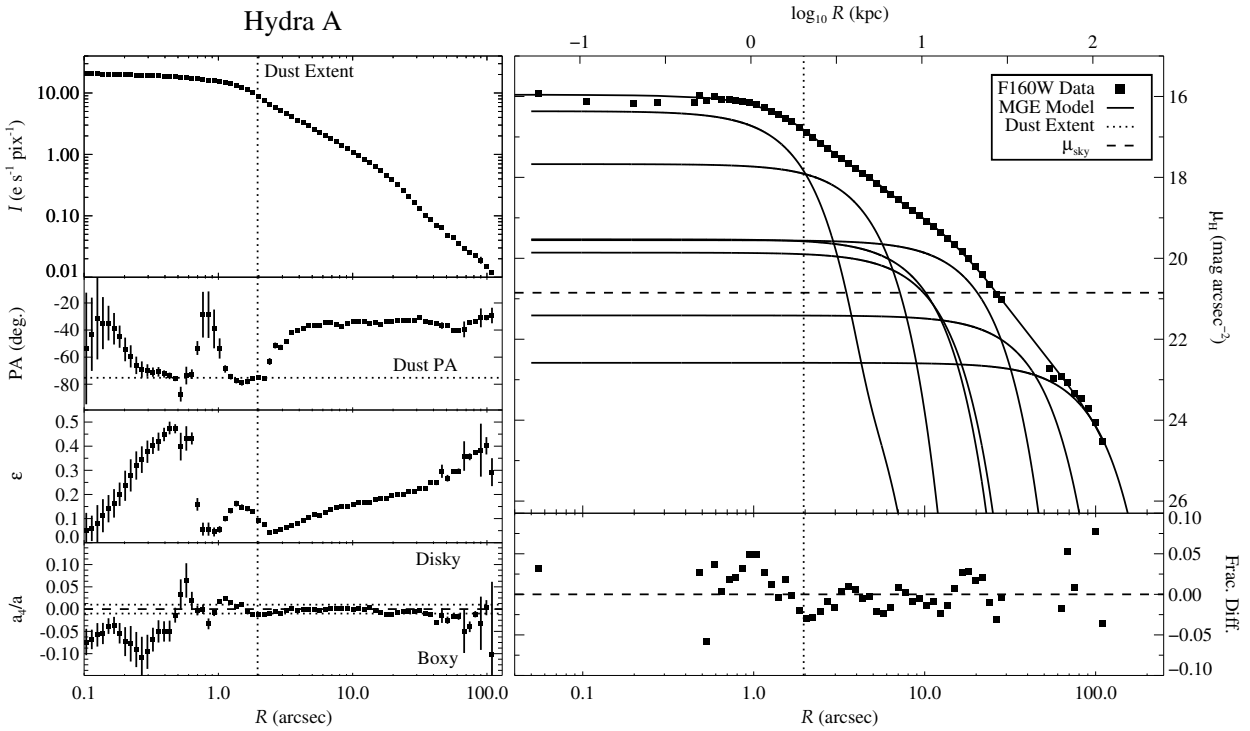

Figure 3.1 Isophotal analysis (*left panels*) and MGE fit (shown along the major axis; *right panels*) for Hydra A after masking the most dust-obscured regions of the CND. Each panel gives the dust disk extent (vertical dotted line), beyond which the fitted ellipse PA and ellipticity ε are reliable and show generally smooth variations. The position angle of the CND is also shown for reference (horizontal dotted line; *PA panel*). The a_4/a deviations from a perfect ellipse are likewise generally small, showing slight preference for boxy isophotes beyond the estimated $R_e \sim 17''$. On the MGE panel are shown both the full MGE and individual components, with generally good agreement (*bottom right panel*) to the data.

spaced radius intervals. The results for the entire sample are plotted together in Figure 2.7.

The results for each individual target are plotted in Figure 3.1 and in Appendix A, together with the stellar luminosity models described in §3.2. In Table 2.2, we report the average stellar photometric PA and the PA and ellipticity ranges from just beyond the outer edge of the dust disk to near the edge of the WFC3 mosaic, where the stellar isophotal behavior can be confidently recovered. The average stellar photometric PA was calculated by taking a weighted average of the PA values,

$$\overline{\mathrm{PA}}_{\star,\mathrm{phot}} = \frac{\sum w_i \mathrm{PA}_i}{\sum w_i}, \quad w_i = 1/\sigma^2_{\mathrm{PA},i}, \tag{3.1}$$

between the edge of the dust disk and R_e, with the exception of NGC 612, whose dust disk radius is

roughly equal to twice its effective radius, and NGC 4797, whose dust disk radius is roughly equal to its effective radius. For these galaxies, the radial ranges were extended out to $3\,R_{\rm e}$ and $1.5, R_{\rm e}$, respectively. The degree of isophotal twisting (ΔPA) was computed using the method described in Goullaud et al. (2018), i.e.,

$$\Delta\mathrm{PA} = \left(\frac{\mathrm{PA}_{i-1} + \mathrm{PA}_i + \mathrm{PA}_{i+1}}{3}\right) - \left(\frac{\mathrm{PA}_{j-1} + \mathrm{PA}_j + \mathrm{PA}_{j+1}}{3}\right), \tag{3.2}$$

where PA_i and PA_j are the absolute maximum and minimum PA values within this radial range, respectively. The range in ellipticity ($\Delta\varepsilon$) was computed likewise,

$$\Delta\varepsilon = \left(\frac{\varepsilon_{i-1} + \varepsilon_i + \varepsilon_{i+1}}{3}\right) - \left(\frac{\varepsilon_{j-1} + \varepsilon_j + \varepsilon_{j+1}}{3}\right), \tag{3.3}$$

where ε_i and ε_j are the absolute maximum and minimum ε values within the radial range, respectively. Some of the final `ellipse` results were not included in these reported ranges due to large uncertainties. We also include the median a_4/a parameter along with its minimum and maximum values over the same set of radial points.

This isophotal analysis shows a broad range of features. Similar trends can be seen between the same types of galaxies. The lenticular galaxies in our sample tend to have fairly constant PA out to $\sim 2\,R_{\rm e}$, with the notable exception of NGC 612. They also tend to show large shifts in ellipticity from $R_{\rm e}$ outward. Our elliptical galaxies seem to have constant PA out to $R_{\rm e}$ then start to diverge at larger radii, with NGC 3862 showing the opposite trend. They also show smaller shifts in ellipticity than their lenticular counterparts, even out to larger radii. The stellar photometric PA twists of the sample are generally small but at times exceeding $\Delta\mathrm{PA} = 45^\circ$. The $\Delta\varepsilon$ values in the dust-free regions corresponding to factor of $\lesssim$2 changes in the isophotal axis ratio. These targets show similar photometric PA behavior as the ETGs in the MASSIVE survey (Goullaud et al. 2018), although none of the 26 ETGs here show as extreme PA twists as measured for a few of the MASSIVE targets. In general, there does not appear to be any clear correlation between the galaxy properties and either the ΔPA or $\Delta\varepsilon$ values. With the possible exception of NGC 6958, these ETGs are almost

uniformly in a group or cluster environment, and past mergers or ongoing interactions are expected to introduce deviations from radially constant PA and ε values.

Half of the galaxies in our sample show minor isophotal twists, which we somewhat arbitrarily set at $\Delta\mathrm{PA} \lesssim 15^\circ$. Of this subset, every case of large $\Delta\varepsilon \geq 0.2$ corresponds to a lenticular galaxy, with the increase in ε following the transition from bulge to disk-dominated regions. In the remaining half of our sample, every other case with such a high $\Delta\varepsilon$ is either a lenticular galaxy or (for NGC 3862 and NGC 6958) shows $\Delta\mathrm{PA} \gtrsim 45^\circ$. In many cases those lenticular galaxies also show elevated ΔPA values.

3.2 Stellar Luminosity Models

We modeled the sky-subtracted H-band surface brightnesses of our galaxies using the Multi-Gaussian Expansion (MGE) formalism (Emsellem et al. 1994), which is convenient for analytical purposes and has been shown to accurately reproduce the stellar profiles of ETGs (see also Cappellari 2002). This series expansion optimizes the peak surface brightness measurements (in $L_\odot$ pc^{-2} units) of each Gaussian component, together with projected dispersions σ' (in arcsec) and axis ratios q'. The MGE formalism is appealing, in part as it provides straightforward surface brightness decomposition and stellar luminosity modeling. Non-parametric approaches allow for more careful analysis of the deprojection (e.g., reconstruction of intrinsic densities and comparison of the relative likelihood of different deprojections; de Nicola et al. 2020). Given the centrally confined ALMA CO kinematics, however, uncertainties in the deprojection are not expected to be significant and we retain the MGE approach.

While photometric PA twists are common, as is shown in §3.1, allowing for variable PA between Gaussian components prevents a simple deprojection and determination of circular speeds in the galaxy's midplane. In a future paper, we will explore MGE solutions when allowing for distinct

PAs, which will be useful for stellar-dynamical efforts (e.g., Krajnović et al. 2011; van den Bosch et al. 2008) that explore the expected triaxality. The isophotal centroids are not always consistent with radius (e.g., Goullaud et al. 2018), likely due to ongoing settling of a recent merger or tidal interaction. However, non-concentric series expansions are not viable for dynamical modeling efforts.

In this paper, we have employed a two-dimensional (2D) concentric MGE that keeps the PA of each Gaussian component tied together during optimization. In addition to the benefit of speed and usability of using MGEs, this approach also enables simple and efficient convolution with a PSF model to account for blurring effects. The ensuing deprojection using the inclination angle i (assuming oblate axisymmetry to determine intrinsic σ and q; Cappellari 2002) then results in an intrinsic stellar luminosity density profile.

Individual Gaussian components generally do not have physical meaning. However, low q' for individual components may fall below $\cos i$ for an assumed i, effectively preventing deprojection. Fully modeling the ALMA CO kinematics does recover a disk inclination angle; a more efficient estimate is $i \approx \cos^{-1}(b/a)$ which uses the observed dust axis ratios reported in Table 2.2, with this proxy so far being accurate to within $\sim 4^\circ$ (see Barth et al. 2016b; Boizelle et al. 2017; 2019). To ensure that the MGE solutions can be deprojected for a range of reasonable inclination angles about the assumed i, we set a limiting $q'_{\rm min} = \cos[\cos^{-1}(b/a) - \Delta i]$ where Δi ranges from 5°(for $i \geq 80^\circ$) to 15° (for $i \leq 25^\circ$). In most cases, this $q'_{\rm min}$ constraint does not severely limit the MGE optimization process, although best-fitting MGEs are sometimes noticeably affected as a result. However, this buffer Δi is unavoidable and ensures that gas-dynamical models are able to explore the full parameter space without deprojection errors. We note that stellar-dynamical modeling typically requires a larger buffer due to the intrinsic galaxy thickness and the optimization of additional intrinsic galaxy viewing angles. Since our stated goal is explicitly to aid future ALMA CO work, we retain the Δi from above.

We first modeled the 2D surface brightness values using the MGE method presented by Cappellari (2002), using a linear decomposition to find initial guesses for the magnitude, FWHM, and q' of each Gaussian component and the initial number of Gaussian components themselves. These initial guesses were then used as input parameters to carry out a final MGE using the 2-D parametric galaxy-fitting algorithm `GALFIT` (Peng et al. 2010) on the H-band mosaic, with between 7 and 16 components in the best fits. In both approaches, we accounted for the H-band PSF by blurring out the intrinsic MGE using the Tiny Tim F160W model during the optimization process. We preferred `GALFIT` as this program allows for the inclusion of an asymmetric, 2D PSF. The Cappellari (2002) code is much faster but requires a symmetrical approximation to the full PSF shape.

In both cases, we employed the contaminant and dust masks described in §2.1 to mitigate the impact of circumnuclear dust during the optimization. In the final MGE solutions presented in Table 3.1, we corrected for foreground Galactic reddening A_H listed in Table 1.1. The resulting MGEs are plotted in Figure 3.1 and in Appendix A. For four of these ETGs (NGC 3557, NGC 3862, NGC 4261, and NGC 4429), very compact inner components arose from distinct AGN in the H-band. We therefore included an unresolved point source in the MGEs of these galaxies in the form of a PSF component to remove prominent AGN contamination.

We wish to emphasize that these MGEs are necessary for obtaining BH mass measurements. In the past, MGEs made for gas-dynamical modeling were not always uniformly constructed and at times lacked a straightforward approach to masking dust features. We created our MGEs as described to correct these problems and provide the best possible results for gas-dynamical modeling.

Table 3.1. MGE Parameters

j	$\log_{10} I_{H,j}$ ($L_\odot$ pc^{-2})	σ'_j (arcsec)	q'_j	$\log_{10} I_{H,j}$ ($L_\odot$ pc^{-2})	σ'_j (arcsec)	q'_j	$\log_{10} I_{H,j}$ ($L_\odot$ pc^{-2})	σ'_j (arcsec)	q'_j	$\log_{10} I_{H,j}$ ($L_\odot$ pc^{-2})	σ'_j (arcsec)	q'_j
(1)	(2)	(3)	(4)	(2)	(3)	(4)	(2)	(3)	(4)	(2)	(3)	(4)
			$q'_{min} = 0.23$			$q'_{min} = 0.24$			$q'_{min} = 0.91$			$q'_{min} = 0.17$
	Hydra A			**NGC 612**			**NGC 997**			**NGC 1332**		
1	3.4550	1.1649	0.9952	4.2379	0.1071	0.9992	4.5670	0.2489	0.9100	5.7035	0.1397	0.3338
2	2.9155	2.9399	0.9060	4.1880	0.3045	0.7814	4.2751	0.7090	0.9118	4.2340	0.2494	0.6765
3	2.1662	6.4848	0.9790	3.8601	0.5822	1.0000	3.9212	1.4545	0.9387	4.9782	0.4911	0.9816
4	2.0350	7.2705	0.6890	3.4447	0.9554	0.9996	3.4301	3.1261	0.9100	4.6117	1.5227	0.7291
5	2.1566	13.133	0.7992	3.3975	2.3870	0.6227	2.9587	6.5902	0.9100	4.2075	3.4156	0.7281
6	1.4121	26.732	0.6940	3.4693	3.8903	0.2553	2.4483	13.696	0.9100	3.8332	7.3989	0.7688
7	0.9438	58.893	0.6676	3.3355	4.1163	0.2400	1.8333	33.844	0.9260	3.1562	17.528	0.3178
8	⋯	⋯	⋯	2.9094	4.9283	0.9815	⋯	⋯	⋯	3.0689	32.944	0.2910
9	⋯	⋯	⋯	3.2056	5.0378	0.5201	⋯	⋯	⋯	2.5357	52.074	0.3259
10	⋯	⋯	⋯	2.3213	12.501	0.6161	⋯	⋯	⋯	1.8995	78.066	0.4190
11	⋯	⋯	⋯	2.1723	16.296	0.9293	⋯	⋯	⋯	0.9968	165.32	0.9901
12	⋯	⋯	⋯	1.3515	40.479	0.9999	⋯	⋯	⋯	⋯	⋯	⋯
13	⋯	⋯	⋯	0.2426	72.324	0.9968	⋯	⋯	⋯	⋯	⋯	⋯
			$q'_{min} = 0.95$			$q'_{min} = 0.52$			$q'_{min} = 0.72$			$q'_{min} = 0.67$
	NGC 1387			**NGC 3245**			**NGC 3258**			**NGC 3268**		
1	5.3554	0.1517	0.9973	5.5227	0.1388	0.6686	4.1386	0.7662	0.9671	3.6153	0.2802	0.6700
2	4.8519	0.5218	0.9994	4.2977	0.2578	0.5378	4.0292	1.1586	0.7200	3.9109	0.9996	0.9918
3	4.5377	1.6441	0.9999	4.7789	0.3163	0.5205	3.9129	2.0040	0.7633	3.9752	1.0794	0.7425
4	4.0769	4.0668	0.9500	4.7368	0.3776	0.9647	3.6336	2.9726	0.8064	3.8462	1.9852	0.7188
5	3.4977	7.1948	0.9500	4.6770	0.6348	0.8459	3.5087	4.8344	0.8513	3.7069	2.2767	0.8903
6	2.8663	14.983	0.9500	4.5074	1.1201	0.9631	2.6360	8.9900	0.8158	3.4637	3.8058	0.7805
7	2.4841	40.343	0.9624	4.0375	2.5263	0.6386	2.9576	11.511	0.9348	3.2626	6.3293	0.8090
8	⋯	⋯	⋯	3.8275	3.2671	0.7809	2.2148	22.281	0.9800	2.8091	12.075	0.7841
9	⋯	⋯	⋯	3.5080	8.9091	0.5200	2.0012	47.787	0.7872	2.4624	21.504	0.8048
10	⋯	⋯	⋯	2.9232	26.569	0.5200	⋯	⋯	⋯	2.0247	51.639	0.7253
11	⋯	⋯	⋯	1.7579	44.971	0.5681	⋯	⋯	⋯	1.5208	87.993	0.9289
12	⋯	⋯	⋯	1.5658	52.299	0.6091	⋯	⋯	⋯	⋯	⋯	⋯
13	⋯	⋯	⋯	1.1653	162.32	0.7948	⋯	⋯	⋯	⋯	⋯	⋯
			$q'_{min} = 0.73$			$q'_{min} = 0.75$			$q'_{min} = 0.99$			$q'_{min} = 0.66$
	NGC 3271			**NGC 3557***			**NGC 3862***			**NGC 4061**		
1	5.0396	0.0654	0.9630	4.2304	0.8510	0.9866	4.1542	0.7628	0.9900	4.1285	0.1755	0.6600
2	5.1355	0.1271	0.7300	4.3214	1.2778	0.7500	3.7966	1.4370	0.9940	4.2827	0.5379	0.6600
3	4.6472	0.3418	0.8132	3.9536	2.0599	0.7500	3.4906	2.9353	0.9910	3.7328	1.0829	0.9533
4	4.2113	0.9768	0.7300	4.0190	2.9514	0.7500	2.7847	7.0954	0.9933	3.6122	1.2839	0.6600
5	4.0600	2.3968	0.7300	3.7178	4.5401	0.7613	2.2149	18.472	0.9900	3.5582	2.1409	0.8016
6	3.7230	3.7726	0.7300	3.4740	6.8297	0.7535	1.7046	58.754	0.9900	3.1855	3.7517	0.8240
7	3.3897	6.8931	0.7300	2.8595	11.632	0.7500	PSF mag = 15.86			2.4901	6.1372	0.9569
8	2.8772	17.577	0.7300	3.0156	13.000	0.7500	⋯	⋯	⋯	2.2961	8.1515	0.6600
9	2.0910	23.313	0.7300	2.6283	22.466	0.7500	⋯	⋯	⋯	2.2072	12.643	0.8367
10	1.8662	51.492	0.7300	2.5442	36.827	0.7500	⋯	⋯	⋯	1.5922	20.997	0.7836

Table 3.1 (cont'd)

j	$\log_{10} I_{H,j}$ ($L_\odot$ pc^{-2})	σ'_j (arcsec)	q'_j	$\log_{10} I_{H,j}$ ($L_\odot$ pc^{-2})	σ'_j (arcsec)	q'_j	$\log_{10} I_{H,j}$ ($L_\odot$ pc^{-2})	σ'_j (arcsec)	q'_j	$\log_{10} I_{H,j}$ ($L_\odot$ pc^{-2})	σ'_j (arcsec)	q'_j
(1)	(2)	(3)	(4)	(2)	(3)	(4)	(2)	(3)	(4)	(2)	(3)	(4)
11	1.2517	76.536	0.7300	2.0470	77.856	0.8731	⋯	⋯	⋯	1.5933	34.329	0.6985
12	⋯	⋯	⋯	PSF mag = 18.08			⋯	⋯	⋯	1.0584	85.239	0.7238
			$q'_{min} = 0.71$			$q'_{min} = 0.52$			$q'_{min} = 0.57$			$q'_{min} = 0.41$
	NGC 4261*			**NGC 4373a**			**NGC 4429***			**NGC 4435**		
1	4.3221	1.1300	0.8272	5.1773	0.1233	0.5200	5.3069	0.1099	0.8506	5.1425	0.1893	0.4802
2	4.0919	2.2040	0.7100	4.8418	0.3496	0.5200	4.8497	0.3361	0.5700	4.6328	0.5244	0.7973
3	3.9639	3.7297	0.7330	4.2347	1.0068	0.5751	4.2484	0.7858	0.7150	4.3501	1.2024	0.7934
4	3.0074	6.4280	0.7128	3.9133	2.1370	0.5750	4.2296	2.4506	0.5700	4.2373	2.3678	0.6816
5	3.3135	8.3664	0.7174	3.4648	4.7480	0.7467	3.5629	2.8757	0.8448	3.9737	4.4603	0.7654
6	3.1794	12.628	0.8213	3.0984	12.208	0.5200	3.8536	5.5932	0.6529	3.2103	11.771	0.4306
7	2.7882	19.961	0.8384	2.2347	29.124	0.5200	3.1773	11.419	0.5802	3.0833	16.253	0.4100
8	1.6889	40.901	0.8312	1.7128	55.969	0.5200	3.2655	16.358	0.5700	2.5444	17.346	0.9515
9	2.3336	45.937	0.8324	0.5813	131.04	0.9992	2.8525	48.696	0.5700	2.4697	31.458	0.5049
10	1.7842	95.152	0.9585	⋯	⋯	⋯	1.9408	118.45	0.5700	1.8732	49.121	0.9890
11	PSF mag = 19.95			⋯	⋯	⋯	PSF mag = 16.21			1.3577	101.44	0.5399
			$q'_{min} = 0.40$			$q'_{min} = 0.35$			$q'_{min} = 0.69$			$q'_{min} = 0.59$
	NGC 4697			**NGC 4751**			**NGC 4786**			**NGC 4797**		
1	5.9764	0.0395	0.9999	6.4801	0.0510	0.3500	4.3138	0.3212	0.9949	4.9958	0.1333	0.5900
2	5.2445	0.1514	0.6473	5.6520	0.2373	0.3500	4.4351	0.5693	0.7301	4.2163	0.4415	0.7869
3	5.0376	0.2026	0.5647	4.2275	0.6124	0.9133	4.1774	1.2630	0.8189	3.7328	0.8758	0.9757
4	4.8123	0.5661	0.7535	4.5265	0.7342	0.7270	3.5661	2.7314	0.7362	3.3653	1.8072	0.9995
5	4.4671	1.2230	0.6929	4.3672	1.7374	0.6292	3.4393	4.7352	0.8107	2.3105	3.5312	0.9926
6	3.7442	2.3117	0.9552	3.8814	4.3905	0.4725	2.5924	5.7134	0.8857	2.6645	4.2037	0.9986
7	4.2202	2.7378	0.4257	3.3609	8.3601	0.4138	2.5916	7.8986	0.6900	2.8346	7.7950	0.7230
8	3.8567	5.4689	0.4400	3.0032	15.729	0.4130	2.6872	12.792	0.6900	2.2715	15.781	0.6797
9	3.5383	5.9815	0.6994	2.4949	34.614	0.3968	2.3202	14.940	0.8763	1.6517	27.516	0.9771
10	3.4398	10.035	0.7140	1.7127	74.088	0.5078	2.1339	23.646	0.6900	⋯	⋯	⋯
11	3.0600	13.751	0.4000	0.5999	195.61	0.9785	1.7691	27.513	0.9666	⋯	⋯	⋯
12	2.8986	24.684	0.4962	⋯	⋯	⋯	0.5270	45.221	0.6900	⋯	⋯	⋯
13	2.7313	25.159	0.4000	⋯	⋯	⋯	1.3639	59.220	0.6900	⋯	⋯	⋯
14	2.8950	33.006	0.6334	⋯	⋯	⋯	1.0990	113.70	0.9629	⋯	⋯	⋯
15	2.5104	61.934	0.6155	⋯	⋯	⋯	⋯	⋯	⋯	⋯	⋯	⋯
16	2.0322	100.77	0.9248	⋯	⋯	⋯	⋯	⋯	⋯	⋯	⋯	⋯
			$q'_{min} = 0.53$			$q'_{min} = 0.75$			$q'_{min} = 0.31$			$q'_{min} = 0.56$
	NGC 5084			**NGC 5193**			**NGC 5208**			**NGC 5838**		
1	5.5612	0.0485	0.9625	5.4122	0.0779	0.8052	4.9465	0.0612	0.7764	5.5792	0.0949	0.9104
2	4.7119	0.4252	0.8361	4.3710	0.4351	0.7500	4.7779	0.2212	0.6476	5.3277	0.1949	0.5600
3	4.5954	0.8865	0.8839	4.3515	0.9310	0.7522	4.3055	0.4898	0.6486	4.9174	0.4639	0.9592
4	4.4646	1.9087	0.7429	3.9793	1.9798	0.8093	3.8914	1.2249	0.5854	4.4024	1.1418	0.7845
5	4.0175	4.6894	0.5300	3.4454	4.6495	0.7500	3.8230	1.6698	0.3100	4.2893	2.1769	0.7211
6	3.6375	8.7644	0.5300	3.0339	9.9193	0.8511	3.5863	2.3040	0.5434	3.8978	4.4985	0.8763
7	3.1027	19.579	0.5300	2.4763	19.507	0.9862	3.5117	5.6576	0.3100	3.3867	9.6674	0.5889
8	2.4945	36.803	0.5300	1.5685	50.580	0.9297	3.1011	6.0413	0.5247	2.8379	16.217	0.5738

Table 3.1 (cont'd)

j	$\log_{10} I_{H,j}$ ($L_\odot$ pc^{-2})	σ'_j (arcsec)	q'_j	$\log_{10} I_{H,j}$ ($L_\odot$ pc^{-2})	σ'_j (arcsec)	q'_j	$\log_{10} I_{H,j}$ ($L_\odot$ pc^{-2})	σ'_j (arcsec)	q'_j	$\log_{10} I_{H,j}$ ($L_\odot$ pc^{-2})	σ'_j (arcsec)	q'_j
(1)	(2)	(3)	(4)	(2)	(3)	(4)	(2)	(3)	(4)	(2)	(3)	(4)
9	2.3508	67.722	0.5300	⋯	⋯	⋯	2.3425	11.388	0.3100	2.6322	40.260	0.5600
10	⋯	⋯	⋯	⋯	⋯	⋯	2.4312	14.314	0.3100	1.0376	76.957	0.5600
11	⋯	⋯	⋯	⋯	⋯	⋯	2.3634	16.031	0.4189	⋯	⋯	⋯
12	⋯	⋯	⋯	⋯	⋯	⋯	1.5939	5.4971	0.3100	⋯	⋯	⋯
13	⋯	⋯	⋯	⋯	⋯	⋯	1.4257	30.922	0.3908	⋯	⋯	⋯
14	⋯	⋯	⋯	⋯	⋯	⋯	1.7014	33.555	0.4073	⋯	⋯	⋯
15	⋯	⋯	⋯	⋯	⋯	⋯	0.6639	95.056	0.8282	⋯	⋯	⋯
16	⋯	⋯	⋯	⋯	⋯	⋯	0.6420	155.62	0.9639	⋯	⋯	⋯
			$q'_{min} = 0.38$			$q'_{min} = 0.95$						
	NGC 6861			**NGC 6958**								
1	4.9281	0.0863	0.9897	4.1856	0.3370	0.9522						
2	4.8513	0.1909	0.9829	5.3515	0.1778	0.9821						
3	4.8755	0.4970	0.3800	4.7191	0.5959	0.9500						
4	4.5806	0.6573	0.9912	4.3206	1.4124	0.9500						
5	4.2921	1.4909	0.8093	3.9184	3.0309	0.9500						
6	4.2214	3.5096	0.4719	3.1345	7.0509	0.9500						
7	3.6775	4.3343	0.7784	2.8078	13.863	0.9500						
8	3.6322	7.4037	0.4323	1.9595	32.998	0.9500						
9	3.2281	12.053	0.4898	0.7920	101.15	0.9500						
10	2.7658	12.219	0.6782	1.597	41.903	0.9500						
11	2.6120	24.266	0.4577	⋯	⋯	⋯						
12	2.3642	27.267	0.7321	⋯	⋯	⋯						
13	1.7034	53.185	0.9982	⋯	⋯	⋯						
14	1.5977	52.037	0.5028	⋯	⋯	⋯						
15	1.1207	124.05	0.9964	⋯	⋯	⋯						

Note. — Individual Gaussian components from the best-fitting MGE for each galaxy in this H-band sample, after masking out neighboring galaxies, foreground stars, and the most dust-obscured regions of the CND. Projected terms are indicated by a $'$. During these fits, the individual q' values were constrained to be equal to or greater than the limit $q'_{\rm min}$ (listed for each galaxy), which ensured the solution could be deprojected for a range of inclination angles. For four of these ETGs (indicated with a *), we included an unresolved point source in the modeling process to remove contamination from distinct AGN in the H band. The magnitudes of these PSF components are given in such cases.

3.2.1 Tiny Tim vs. Empirical Results

We chose NGC 3862 to explore a comparison of the effects of the Tiny Tim and empirical H-band PSFs on an MGE solution due to its prominent AGN in the H-band, and consequently the prominent PSF component (see the Appendix). We followed the same method as previously outlined for the MGE solution utilizing the empirical PSF as for the solution utilizing the Tiny Tim PSF. We left the CND unmasked (see Figure 2.6) and included a PSF component. We also constructed the resulting circular velocity curves following the method described in §3.3.4.

Figure 3.2 shows the final drizzled H-band PSFs at the same spatial extent, the MGE fits using

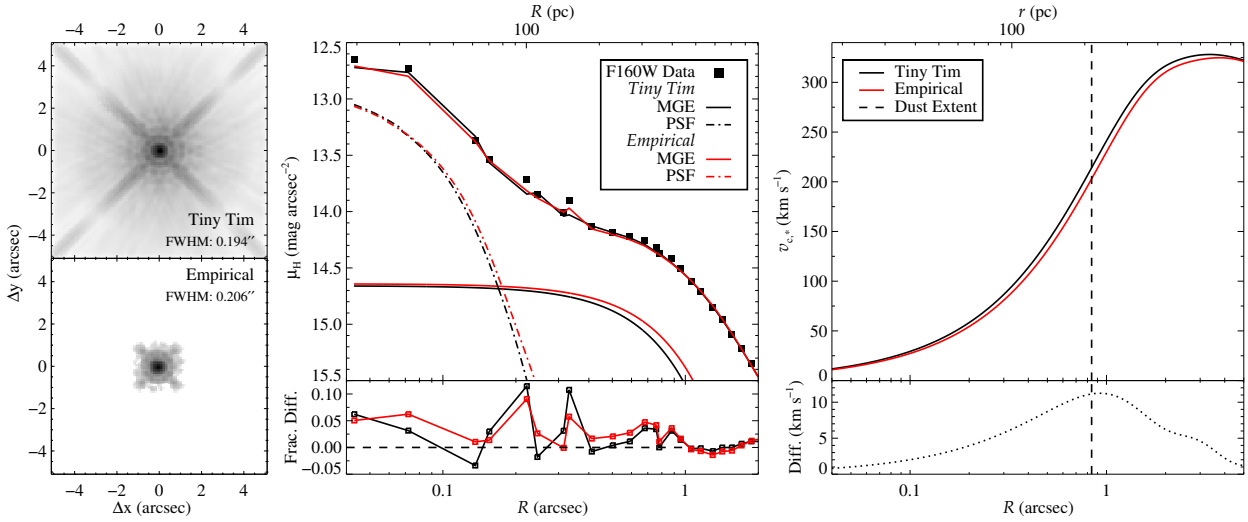

Figure 3.2 *Left panels:* The drizzled H-band Tiny Tim (*top*) and empirical (*bottom*) PSFs for NGC 3862 shown to the same spatial extent. *Middle panels:* MGE fits utilizing the Tiny Tim and empirical PSFs shown along the major axis. Note that the CND was left unmasked and a PSF component is included in both models to account for prominent AGN contamination. Both the full MGE and the first component are shown for the two models, each with generally good agreement (*bottom*) to the data. *Right panels:* Corresponding stellar circular velocity curves assuming a stellar-only potential and the difference (*bottom*) between the Tiny Tim fit and the empirical fit. The difference in velocity is generally smaller than the bin size of most ALMA CO data.

both types of PSF, and the corresponding stellar circular velocity curves assuming a stellar-only potential. We find good agreement between both MGE fits and the H-band surface brightness measurements, with the fractional residuals along the galaxy major axis in both models being smaller than $\sim 12\%$. The empirical PSF has somewhat better agreement with the observed stellar FWHM and leads to an arguably better fit of the inner $1''$ before becoming practically identical to the Tiny Tim fit out to larger radii. The empirical PSF also leads to a velocity curve with slightly smaller velocities out to $R \sim 5''$. The difference in velocity, with a maximum of ~ 11 km s^{-1}, is generally smaller than the bin size of most ALMA CO data. Our findings are consistent with the conclusions of Zhao et al. (2021) that an empirical PSF (in our case, one not derived from foreground stars in the FOV) does appear to lead to better fits. However, this does not disparage the common practice approach of utilizing a Tiny Tim PSF, as used by previous authors and in this work. Both fits agree with each other to within $\sim 5\%$. The data are well-represented by the Tiny

Tim fit, which suggests that the Tiny Tim PSF is an adequate prescription for the PSF in stellar luminosity modeling.

3.3 Discussion

3.3.1 Goodness of Fit

We find generally good agreement between each MGE and the respective H-band galaxy surface brightness measurements, with formal chi-squared per degree of freedom $\chi^2_{\rm dof} = 1 - 1.5$ in the 2D fit and fractional residuals along the galaxy major axis typically being smaller than $\sim 10\%$. The stellar isophotes of some targets trend towards disky or boxy shapes, especially for NGC 612, NGC 3271, NGC 4373a, NGC 4429, and NGC 5084. In these cases, the result is somewhat worse 2D decomposition in the MGE approach.

In most cases, larger discrepancies are seen for galaxies that have steep rises in ellipticity ($\varepsilon = 1 - b/a$) at larger radii, which exceeded their $q'_{\rm min}$ limitation. The most affected galaxies are NGC 1387, NGC 3271, NGC 4373a, NGC 4429, NGC 5084, and NGC 5838. However, these $q'_{\rm min}$ values are needed to allow for reasonable deprojection. Take as an example the MGE fit for NGC 1387, as is shown in Figure A.4. From $R \sim 10 - 35''$, the poorest fit region is coincident with a sharp rise in ellipticity that greatly exceeds the corresponding $\varepsilon_{\rm max} \sim 0.05$. Excessive ellipticity is the culprit for the poorer fits at larger radii for most of the aforementioned galaxies. The exception is NGC 5084, which shows a distinct disk component between $R \sim 10 - 100''$ (see Figure A.20) that is subdominant at these radii when averaging over all angles. If additional Gaussians are added to the 2D MGE, these new components still prefer to fit the larger-scale, more apparently round stellar surface brightnesses (unless we relax the $q'_{\rm min}$ constraints and adopt a very low initial q' guess). As a final note on this topic, we emphasize that, while these 2D MGEs do not always fully reproduce the H-band light, the impact of larger-scale discrepancies on the *central* deprojected stellar luminosity

densities is generally very small (see Figures 2.5 and 2.6).

Depending on the degree of dust attenuation, the needed masking may not retain a large fraction of the H-band surface brightnesses inwards of $R_{\rm dust}$. As a result, some of the MGE fits have inner components that are not as tightly constrained, especially for those with $\sigma' < 1''$. At slightly larger radii, there are frequently large gaps in coverage except along the minor axis near the far side of the disk. Some faint dust features that are below our masking threshold still affect the stellar surface brightness values (producing dips at small scales; e.g., see Figure 3.1 and A.9), which cannot be well fit by these concentric MGE models. Lastly, the central stellar light may appear more elongated along the major axis (e.g., NGC 1332; see also Bonfini et al. 2018) due to dense dust on the near side of the disk that approaches the nucleus in projection. Especially for the more edge-on disks, more aggressive dust masking is not always a viable solution.

Our decision to adopt a fixed PA for all MGE components for this paper does limit the full reliability of some MGE fits for radii $R \sim 20'' - 2'$. In Figure 2.5 we show H-band drizzled mosaics together with the best-fitting MGE solutions for NGC 612, NGC 3245, and NGC 3557, which are representative of the larger sample (shown in Figure 3.3). The MGE solutions agree well within zoom-in regions and out to at least $R \sim R_{\rm e}$, beyond which stellar isophotes often exhibit some level of PA twists that cannot be fully fit here. For 20% of this sample, these PA twists reach or exceed 45°, with most of the large shifts manifesting at large radii. Fully half of the ETG sample have much smaller $\Delta{\rm PA} < 15°$, which is more indicative of relaxed systems.

We note that while these dust-masked MGEs of H-band data well represents the intrinsic light distribution, relying solely on such a stellar luminosity model may bias the BH mass measurement. Gas-dynamical modeling that incorporates both dust-masked and dust-corrected stellar luminosity models provides a broader but more accurate BH error budget. Exploring a plausible range of extinctions is beyond the scope of this paper, so we instead just highlight previous results on the shifts in BH mass between models ($\Delta M_{\rm BH}$) due to extinction for relevant literature sources.

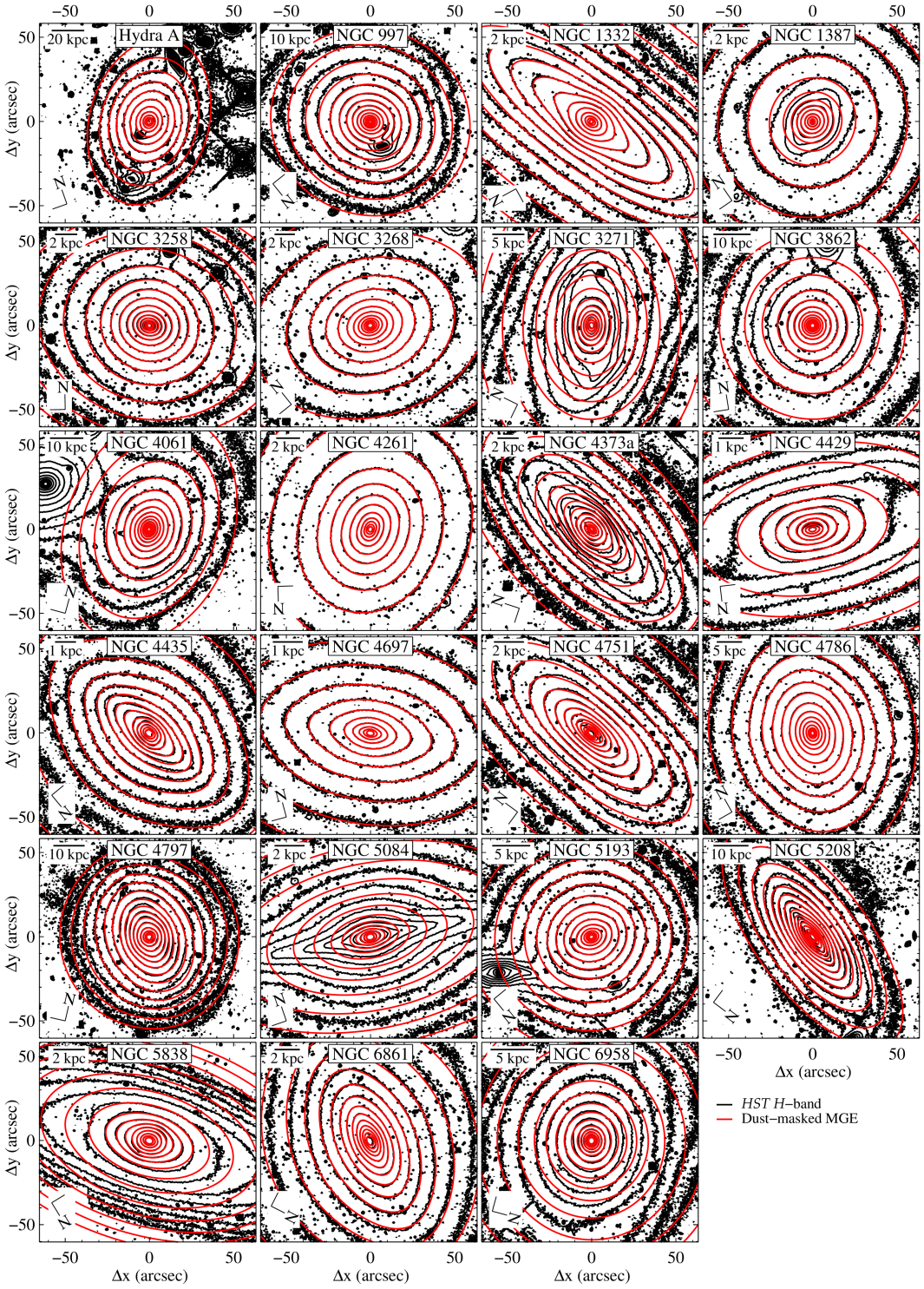

Figure 3.3 HST WFC3 F160W drizzled mosaics for targets not shown in Figure 2.5. Nearly full-frame sky-subtracted data are shown using contours that are logarithmically spaced to highlight the range of features. The best-fitting `GALFIT` MGE solutions are overplotted (in red). At larger radii, stellar isophotal PA twists, high ellipticity components, and disky/boxy isophotes result in unavoidable discrepancies.

For the three such cored galaxies, the impact has been relatively minor (Boizelle et al. 2019; 2021). The $\Delta M_{\rm BH}$ from the best-fitting BH masses ranged between at about $10-20\%$ with these dust-masked MGE corresponding to the upper end of this mass range. Because these cored galaxies have strong, Keplerian-like CO velocity upturns towards the center, effectively anchoring these BH mass measurements against changes in the stellar mass model, they may not be the most representative. This is best illustrated by BH mass measurements for more cuspy ETGs. For those with completed gas-dynamical modeling and whose CO emission extends within or near to $r_{\rm g}$ when exploring different stellar mass models (e.g., MGEs constructed in different filters, or alternating between dust-masking or correction techniques), the $\Delta M_{\rm BH}$ range between 30% and a factor of more than two (Barth et al. 2016a;b; Cohn et al. 2021; Davis et al. 2018; Kabasares et al. 2022). None of these more cuspy galaxies unambiguously show CO emission arising from deep within $r_{\rm g}$, contributing to – at least in part – the larger $\Delta M_{\rm BH}$ shifts.

3.3.2 Additional Challenges

The large angular extents and high dust opacities of some disks prevent minimal dust masking and straightforward analysis. For example, NGC 612 contains a large dusty disk ($R_{\rm dust} \sim 20''$) that shows evidence for both star formation (Duah Asabere et al. 2016) and moderate disk warping with at least $\Delta{\rm PA} \sim 20^\circ$ in the outer regions. Even in the H-band mosaic, excess light from star formation and thick dust necessitates masking nearly the entire disk region and nucleus (see Figures 1.5 and 2.5). As is reported in Table 3.1, the first 9 Gaussians in the 13-component fit have σ' that are smaller than the semi-major axis extent of the more regularly-shaped inner disk ($R \sim 10''$). The central part of the MGE fit well reproduces the galaxy surface brightnesses, as is shown in Figure A.1, although the heavily masked stellar surface brightnesses near the nucleus provide fewer constraints to anchor peak I_H values and fit σ' and q' for the innermost MGE components.

In at least two other cases, NGC 997 and NGC 1387, their large projected disk sizes ($R_{\rm dust} \sim$

$5-10''$) and rough uniformity towards the nucleus also introduce challenging case studies in dust masking (see Figure 2.6). For NGC 997, whose CND is viewed slightly less face-on ($i \sim 35^\circ$), we masked all of the near side of the disk and much of the far side that was not along the minor axis. For NGC 1387, the excess color above the stellar $J-H$ values approaches (but does not exceed) the rough 0.08 mag masking criterion. Since dust attenuation is not readily visible in the H-band mosaic, we did not mask out any regions of the more face-on ($i \sim 28^\circ$) dusty disk.

In addition to masking concerns, these CNDs may not reside in the galaxy's midplane in every case, or at least not at all radii. Tran et al. (2001) used HST optical imaging of ETGs to identify dust in either filamentary features or inclined disk shapes to quantify the prevalence of asymmetries and warped-disk signatures. They interpreted the range of observed features as evidence for a settling sequence of merger or accretion-acquired gas (see also Lauer et al. 2005). For our sample, the dust-disk orientations generally agree closely with the corresponding stellar photometric axis. One noticeable exception is NGC 3271, whose CND is oriented $\sim$20° off from the stellar isophotal PAs. A more complete analysis of potential mismatches would involve measuring and comparing stellar and gaseous kinematic axes.

We do see instances of moderate disk warping in our sample, most noticeably in the HST images of NGC 612 and NGC 4797. Localized dust asymmetries near the disk edges are also seen, as is the case for the CNDs in NGC 3268 (see the images in Boizelle et al. 2017) and, to a lesser extent, in NGC 4435 (see Figure 2.3). Boizelle et al. (2017; 2019) characterized disk warping as a function of radius R using ALMA CO kinematics for four of our targets, finding the derived $i(R) \approx \cos^{-1} q(R)$ changes by 5–10° at larger radii. Gas-dynamical modeling reveals hints of more extreme behavior from recovered $i(R)$ towards the disk center. Certain targets, especially NGC 3557 and NGC 4261, show CO kinematics that are moderately misaligned with the radio jet orientation (at the $10-50^\circ$ level; Boizelle et al. 2021; Ruffa et al. 2019), at least at the resolution limit of these beam-smeared ALMA data. This suggests sharp twists in the PA (and plausibly i) of the innermost CO kinematics.

In these cases, it is not clear that the outer dust b/a is always representative of the inclination of the galaxy's midplane.

For CNDs with larger angular extents, or for cuspier galaxies with higher central $\Delta(J-H)$, current near-IR observations with HST may not be sufficient to confidently constrain dust attenuation on a pixel-by-pixel basis. Indeed, extended dust features will also limit confidence that the inferred stellar surface brightness slopes in unmasked regions are representative of the intrinsic values. In such cases, James Webb Space Telescope (JWST) NIRCam data at $4.5-5$ μm will be warranted to further mitigate the impact of dust and to ensure high-quality MGEs for ALMA CO gas-dynamical modeling. JWST data will be especially useful in constraining the stellar behavior in the outer disk, which is expected to be optically thin at these longer wavelengths. Less extensive dust masks translates to better sampling of the stellar surface brightness values in the crucial $R = 1-10''$ range.

3.3.3 Consistency of the MGE Solutions

For two ETGs in this sample, NGC 3258 and NGC 4261, Boizelle et al. (2019) and Boizelle et al. (2021) presented dust-masked MGEs using the same underlying H-band data sets. In this paper, we decided to calculate new MGEs to explore the reliability of the MGE solutions when allowing for slight differences in mosaic construction, dust masking, and the number of Gaussian components. At the disk edges, we find minimal differences between the derived circular velocity profiles $v_{\rm c}(r)$ or the corresponding enclosed mass profiles $M(<r)$ for each MGE, assuming the same mass-to-light ratio and $M_{\rm BH}$, and a spherical mass distribution. Here, r is the physical distance in the galaxy's midplane. Additional details about constructing $v_{\rm c}(r)$ are found in §3.3.4. At interior radii, these profiles disagree by at most 10%. Since the BH masses in these targets are strongly constrained by Keplerian-like disk rotation and due to the very high resolution of $r_{\rm g}$ in both galaxies from ALMA data, such a small change in the underlying stellar luminosity model would likely only negligibly

impact gas-dynamical modeling results. At large radii, when compared to these other MGEs whose fits also included larger-scale imaging, we find our MGEs produce essentially the same $M(< r)$ curves out to the edge to the respective H-band mosaic, or out to $R \sim 2'$, suggesting that the MGEs in Table 3.1 should be reliable out to the edge of the respective HST footprint.

It is not trivial to compare MGE solutions and the corresponding v_c and $M(< r)$ profiles that differ significantly in wavelength and construction (see Figure 6 of Barth et al. 2016b). While we do not attempt any rigorous comparison for the entire sample, we do discuss one prominent – and challenging – example in NGC 4429. When modeling CO kinematics for this target, Davis et al. (2018) employed an MGE of the dust-masked F606W image and a radially-varying M/L_V ratio over the central disk region. They directly fit this variable M/L_V during the gas-dynamical modeling process. Using their MGE and fitted M/L curve, we recovered the corresponding enclosed mass profile. We compared it to the $M(< r)$ for our H-band MGE that had been scaled by the same M/L gradient shape after normalization to match the F606W-derived $M(< r)$ curve at the edge of the CO(3−2)-bright part of the disk, at $R \sim 5''$. In both cases, the innermost Gaussian component was ignored to eliminate dominant AGN contributions. We find that our MGE prefers significantly higher $M(< r)$ near the disk center, with the H-band MGE returning $\sim$20−30% higher mass between $R \sim 1 - 2''$. This discrepancy may be due in part to the number of components used. As shown in Table 3.1, our dust-masked MGE for NGC 4429 has two components with σ' that are smaller than that of the first remaining component reported by Davis et al. (2018). Another likely contributor is the wavelength difference. In unmasked regions (mostly along the minor axis), the H-band stellar light behind the disk is a factor of $\sim 5\times$ less attenuated than the F606W data, allowing for better recovery of the intrinsic stellar light distribution.

3.3.4 Circular Velocity Curves

To test the reliability of CNDs in ETGs in a CO TF analysis, we constructed circular velocity profiles $v_{c,\star}(r)$ corresponding to only the stellar light distribution. Assuming our galaxies are oblately axisymmetric and inclined at the same angle as their respective CNDs, we deprojected the H-band MGE models and numerically integrated the stellar luminosity densities using the `Jeans Anisotropic Models` (JAM; Cappellari 2008) modeling package to determine $v_{c,\star}$ as a function of radius. For simplicity, we assumed a uniform $M/L_H = 1.5 M_{\odot}/L_{\odot,H}$ based on single stellar population models (Vazdekis et al. 2010) and ignored dark matter contributions as negligible within the central few kpc for such galaxies (De Bruyne et al. 2004). In Figure 3.4, we plot both $v_{c,\star}(r)$ and $v_c(r)$ after including M_{BH}, either from literature measurements or estimates using BH mass-host galaxy correlations. Not including the (often uncertain) impact of M_{BH}, the $v_{c,\star}$ span about 150–400 at the disk edge R_{dust}. Following previous findings (e.g., Boizelle et al. 2019; 2021; Cohn et al. 2021), we do not attempt to include the much lower gas mass contributions to $v_c(r)$.

When plotted as a function of R_{dust}, it is clear that not all $v_{c,\star}$ curves reach V_{max} within the dust extent or approach a high asymptotic velocity at these radii. For some of our sample, the anticipated BH mass compensates for low $v_{c,\star}$ contributions near the center. Beyond the BH-dominated region, which typically does not contain significant CO emission, we find that about half of the $v_c(r)$ solutions reach a V_{max} at $R \lesssim R_{dust}$. For $\sim$20% of the sample, we find that the $v_c(r)$ reach an asymptotic velocity within the disk region, although sometimes the v_c only plateau beyond r_g before falling off at large r. As expected, only the larger CNDs reach V_{max}, which for our sample generally corresponded to galaxies with $R_{dust} \gtrsim 0.88$ kpc. For most of the apparently cored ETGs, the extended $v_c(r)$ profiles reach V_{max}, either within or beyond R_{dust}. Those with cuspy stellar surface brightness profiles tended to show asymptotic v_c within (or just beyond) the disk edge. Only one galaxy, NGC 5838, deviated from this trend and exhibited a clear maximum circular velocity.

The disks in our sample (with a median $R_{dust} \approx 0.4$ kpc) are smaller than the inferred sizes of

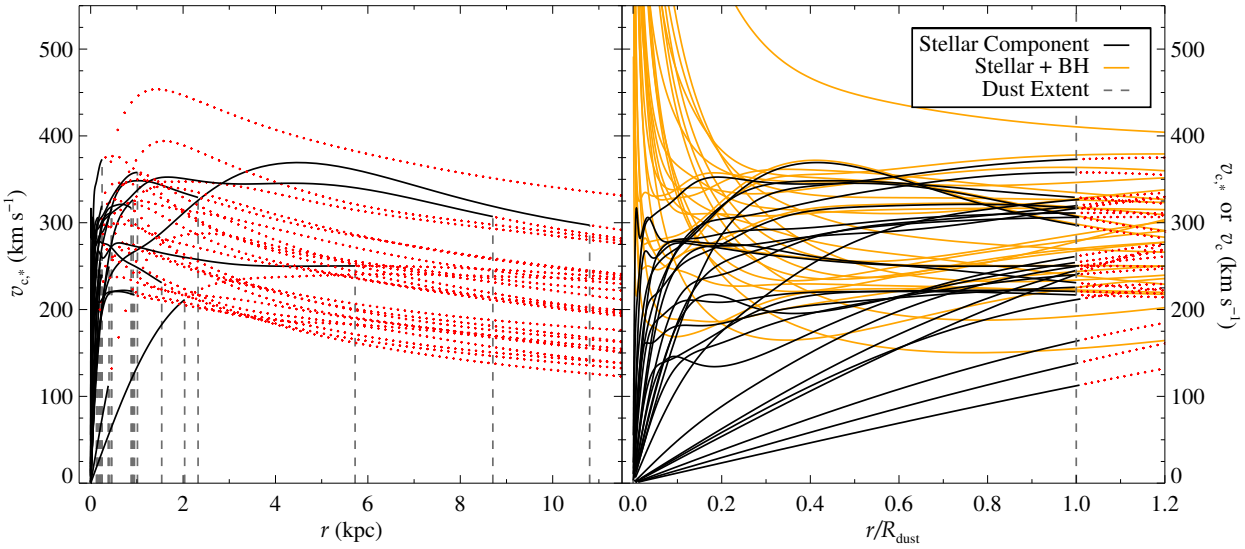

Figure 3.4 Circular velocity ($v_{c,\star}$ and v_c) curves for the galaxies in our sample, constructed by deprojecting the H-band MGEs and numerically integrating the stellar luminosity densities. Stellar rotation curves (black solid lines; *left panel*) assume a stellar-only potential. Solutions for $r > R_{dust}$ are included (red dotted lines) along with the extents of each dust disk (dashed lines). To better compare the inner curves of these results, the same $v_{c,\star}$ curves are normalized (*right panel*) to their respective dust disk radii, together with v_c curves (orange solid lines) that include the effects of the expected BH masses. With the exception of four BH masses already measured by stellar (Rusli et al. 2013) or gas-dynamical modeling (Barth et al. 2016b; Boizelle et al. 2021; Davis et al. 2018), the BH masses were estimated using $M_{BH} - \sigma_\star$ or $M_{BH} - L_K$ relations.

CNDs from previous CO surveys. From both the ATLAS^{3D} (ETG) and BIMA-SONG (late-type galaxy) surveys, we find a median CO radius $R_{CO} = 0.88$ kpc and 1.63 kpc, respectively (both based on values from Davis et al. 2013). We note that both CO surveys are limited by sensitivity considerations and do not detect CO emission from all dusty CNDs (e.g., for NGC 4261; Boizelle et al. 2021; Young et al. 2011). Because of sensitivity limitations, the R_{CO} may not probe the entire extent for those detected disks (to illustrate this, see a related scenario for NGC 4429; Davis et al. 2013; 2018). On the other hand, the ATLAS^{3D} survey tended to detect (Young et al. 2011) and resolve (Davis et al. 2013) only the largest CNDs. Because of these competing effects, we cannot confidently place the CND radii of our targets in context with volume-limited surveys. For a more comparative sample of dust-disk radii, Tran et al. (2001) found a median $R_{dust} \sim 0.1$ kpc. Unfortunately, this snapshot survey is not complete and the R_{dust} distribution is strongly clustered

around ∼100 pc.

3.3.5 Gas-Dynamical Modeling Results

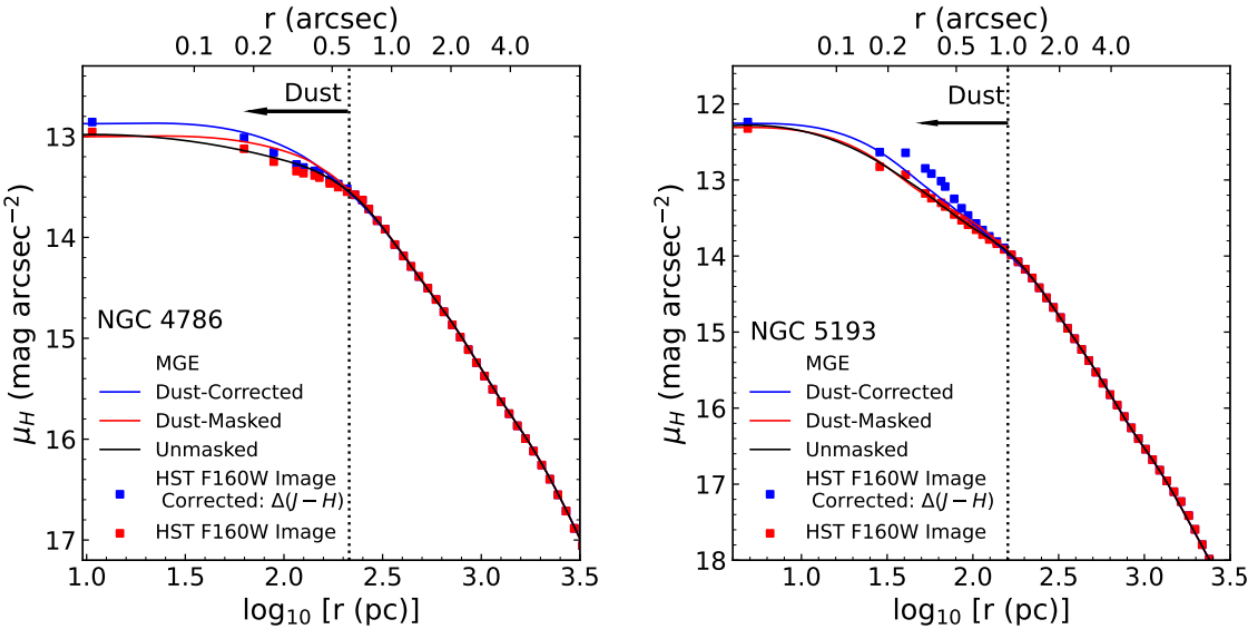

Figure 3.5 A comparison of the observed and modeled H-band surface brightness profiles of NGC 4786 (*left*) and NGC 5193 (*right*). The surface brightness measurements are made with the Python-implementation of the `sectors.photometry` routine (Cappellari 2002) which performs photometry along evenly spaced sectors from the major axis to the minor axis and averages measurements over the four quadrants of the image. For each panel, the red squares are the observed values from the H-band image, while blue squares are dust-corrected values. The lines in each panel correspond to surface brightness profiles extracted along the major axis for each of our 2D MGE models. Red lines are for dust-masked MGE models whereas black and blue lines represent dust-unmasked and dust-corrected MGEs, respectively. The dashed lines indicate the dust disk edge and the arrows indicate that the dust extends down to the nucleus. [From Kabasares et al., submitted]

We highlight some recent gas-dynamical modeling results. Using some of the MGEs from this thesis, Kabasares et al., (submitted) attempted to measure the BH masses of NGC 4786 and NGC 5193. Figure 3.5 shows their comparison of the observed and modeled H-band surface brightness profiles for both of these galaxies. Our dust-masked models are seen in red. Figure 3.6 shows the moment maps for NGC 5193 constructed from ALMA CO(2−1) data and the model. They measured a BH mass of $(M_{\rm BH}/10^8 M_\odot) = 5.0 \pm 0.2$ [1σ statistical]$^{+1.4}_{-1.3}$[systematic] in NGC 4786

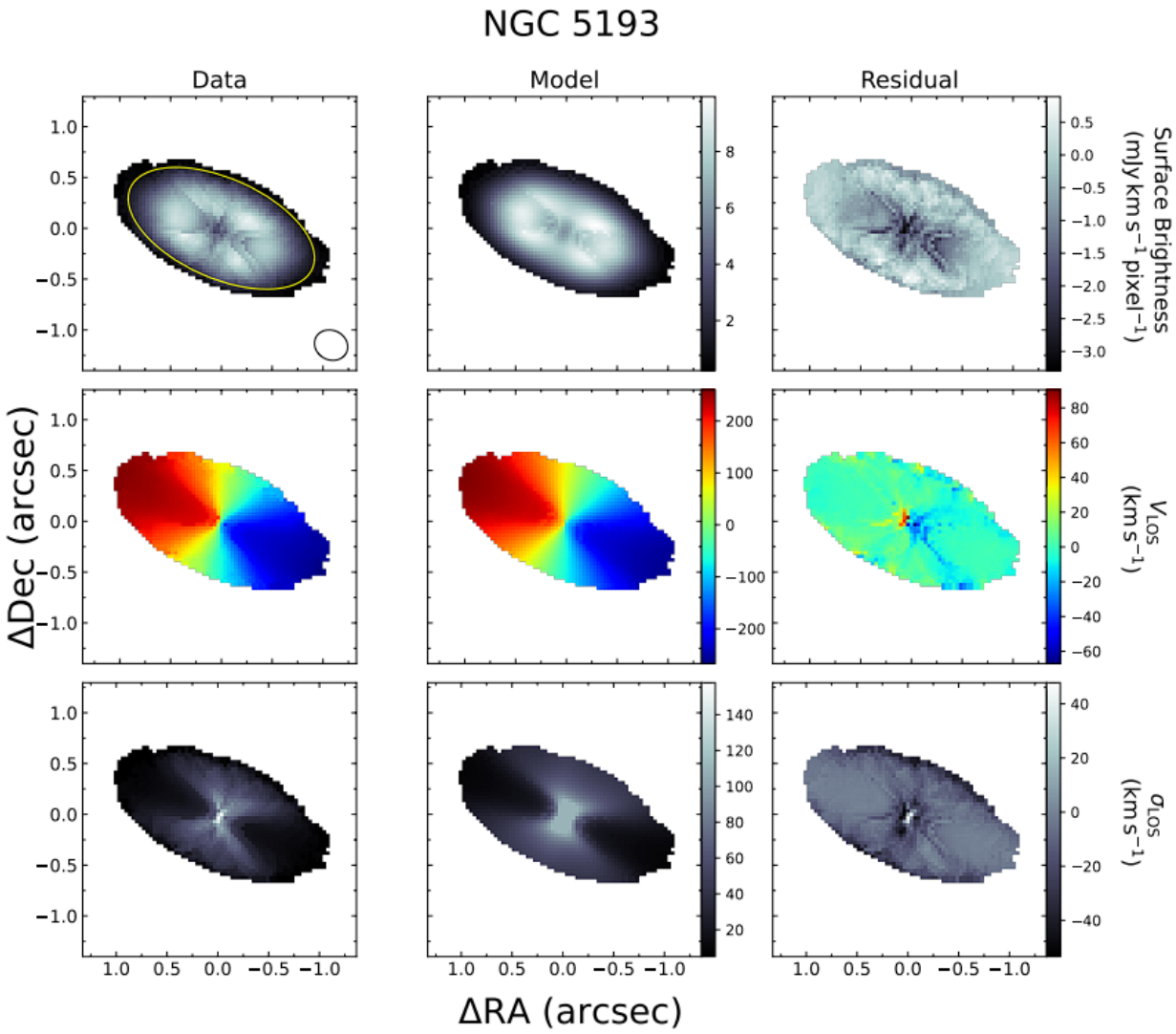

Figure 3.6 Moment maps for NGC 5193 constructed from the ALMA CO(2−1) data cube (*left*) and its fiducial model (*center*). Shown are maps of moments 0, 1, and 2, corresponding to surface brightness, line of sight (LOS) velocity ($v_{\rm LOS}$), and LOS velocity dispersion $\sigma_{\rm LOS}$. The units for the surface brightness map are mJy km s^{-1}pixel^{-1}, and the units for the $v_{\rm LOS}$ and $\sigma_{\rm LOS}$ maps are km s^{-1}. The systemic velocity of 3705 km s^{-1}estimated from our dynamical models has been removed from $v_{\rm LOS}$. Maps of (data-model) residuals are shown in the rightmost column. The coordinate system is oriented such that +x corresponds to East and +y corresponds to North. While the line profile fits have been determined at each pixel of the full disk, the elliptical fitting region used in calculating χ^2 is denoted in the top left panel with a yellow ellipse. The synthesized beam is represented by an open ellipse in the bottom left corner of the same image. [From Kabasares et al., submitted]

and $(M_{\rm BH}/10^8 M_\odot) = 1.4 \pm 0.03$ [1σ statistical]$^{+1.5}_{-0.1}$[systematic] in NGC 5193.

This recently submitted paper is the first of many to use the MGEs in this thesis in pursuit of BH

mass measurements. Plausible dust corrections, as demonstrated in Figures 3.5, 3.6, and the figures in §3.4 typically introduce the largest terms in the final BH mass error budget but such exploration is needed given the inherent uncertainty in the correct level of dust attenuation.

3.4 Future Work: Dust Attenuation Modeling

This current work has focused on data preparation and constructing dust-masked MGEs for gas-dynamical modeling. Ongoing work is extending this to determine dust attenuation from the multi-wavelength HST data we have obtained. Here, we detail the future process of modeling the extinction from the circumnuclear dust disk, which is essential in order to derive accurate models of the host galaxy stellar mass profile from the HST images.

As is the case with all of our targets, each CND is inclined dusty disk embedded in the midplane of the galaxy. Light emitted from within and behind the disk is attenuated while light from in front of the disk is unobscured. In the limit of very high optical depth for a thin disk, light from the far side of the disk would be completely obscured and a $B-I$ color map would not reveal any color excess [$\Delta(B-I)$; see Figure 3.7]. The maximum observed $\Delta(B-I)$ would only occur for some moderate value of optical depth along the disk where some reddened starlight is permitted to pass through. For an inclined, embedded dust disk, the near side of the disk would be expected to show a larger color excess than the far side as the near side of the disk obscures a greater fraction of the host galaxy's starlight (Elmegreen & Block 1999).

One can employ a simple embedded-screen model using the method described by Viaene et al. (2017) (see Figure 3.8) to examine the relationship between disk optical depth and observed color excess. In this model, the CND is treated as a thin, inclined disk bisecting the galaxy. Along a given line of sight, the fraction b of total stellar light originating behind the disk is obscured by simple screen dust extinction while the fraction f in front is unaffected. In the case of a thick disk, a small

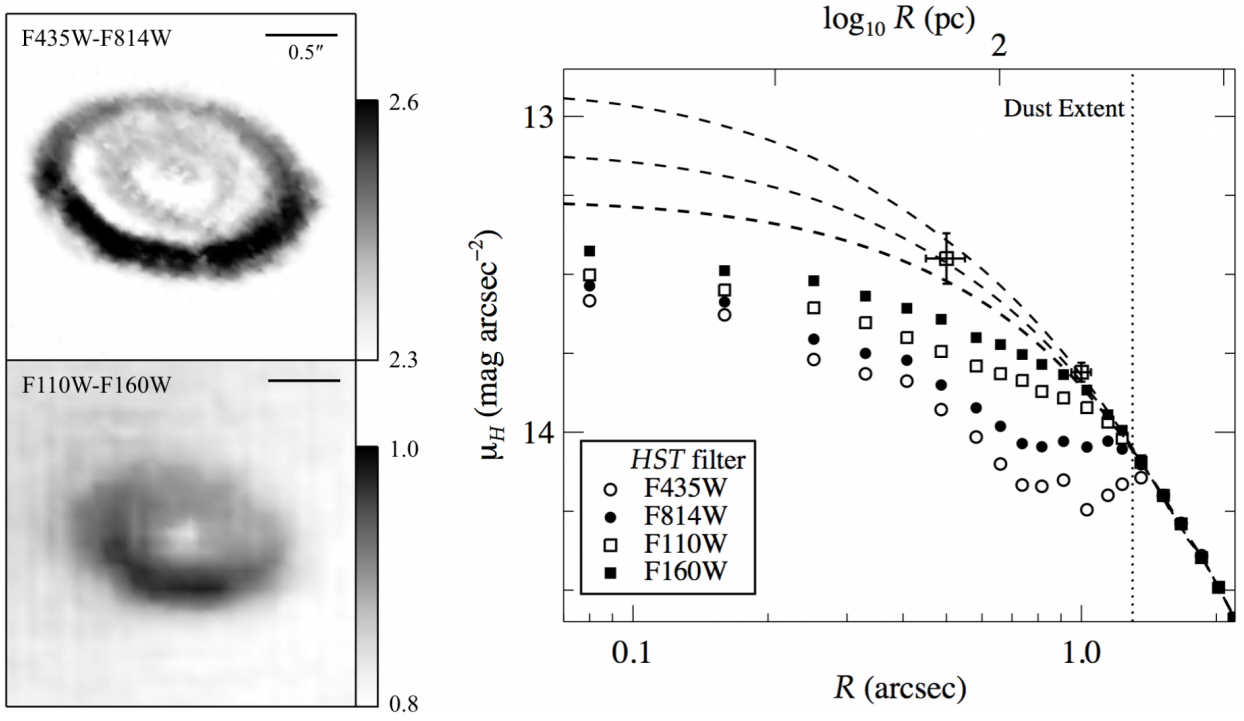

Figure 3.7 HST optical/IR observations of NGC 3258. While evident in each individual filter, the dust disk is most prominent in the optical (F435W-F814W; *top left*) and near-IR (F110W-F160W; *bottom left*) color maps. The dust disk extent appears largest in the optical colors. Since the $J-H$ colors are highest at $R \sim 0\farcs5$, the relatively low, coincident $B-I$ excesses indicate the disk so completely obscures the background stellar light that it no longer contributes appreciably to the observed optical color. The central H-band surface brightness (*right*) is much less obscured than at bluer wavelengths (scaled to match the F160W data points at $R \sim 1\farcs5$), although even at these reddest wavelengths the central stellar surface brightness still appears somewhat suppressed. Using dust attenuation models that treat the obscuration as a thin screen in the host galaxy midplane (Viaene et al. 2017), we approximate the range of extinctions at $R \sim 0\farcs5$ and $R \sim 1\farcs0$ and correct the H-band data assuming extinction at the lowest, average, and highest plausible values. We create three model surface brightness profiles (dashed lines) associated with these values to replace the dust-obscured data and derive dust-corrected model stellar luminosity profiles. For one of these individual stellar mass models, ALMA CO gas-dynamical modeling returns $\sim 0.5\%$ statistical uncertainties on the $M_{\rm BH}$ value, while the final BH mass error budget is dominated by the $\sim 5\%$ change in BH mass between these stellar models that reflects the dust systematic uncertainty (for more details, see Boizelle et al. 2019).

fraction ($w = 1 - f - b$) of the total light may originate within the disk. The wavelength-dependent ratio F'/F^0 of observed to intrinsic stellar light has the form

$$\left(\frac{F^{\rm obs}}{F^0}\right)_\lambda \approx f + w\left[\frac{1-10^{-A_\lambda/2.5}}{0.921A_\lambda}\right] + b[10^{-A_\lambda/2.5}]. \tag{3.4}$$

To determine f and b (assuming a very thin disk; $w \to 0$), one can evaluate Equation 3.4 at the pivot wavelengths of the filters used in the observations to generate predictions for the opacity-dependent

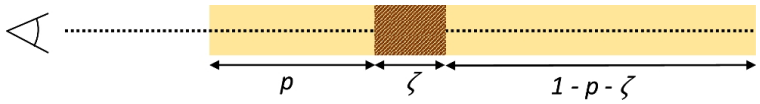

Figure 3.8 Graphic of the embedded dust screen model. A dust layer of thickness ζ is embedded in a stellar layer. A fraction of stars, p, in front of the disk are unobscured. [From Viaene et al. (2017)]

color excess at each spatial location,

$$\Delta(B-I) = -2.5\log_{10}\left[\left(\frac{F^{\rm obs}}{F^0}\right)_B\left(\frac{F^{\rm obs}}{F^0}\right)_I^{-1}\right], \tag{3.5}$$

and

$$\Delta(J-H) = -2.5\log_{10}\left[\left(\frac{F^{\rm obs}}{F^0}\right)_J\left(\frac{F^{\rm obs}}{F^0}\right)_H^{-1}\right]. \tag{3.6}$$

Figure 3.9 shows an example from Boizelle et al. (2019) of the modeled color excesses $\Delta(B-I)$ and $\Delta(J-H)$ of NGC 3258 as a function of intrinsic extinction A_V of the obscuring disk. These color excesses were extracted at three locations each and illustrate the effect of dust inclination on the color excess at different locations in the disk. As expected, the model predicts a small color excess for both very low and very high disk optical depths and reaches a maximum value at intermediate extinction. This simple embedded dust model predicts maximum color excess values that are in very close agreement with both the $B-I$ and $J-H$ color maps of NGC 3258, as seen in Figure 3.9.

In order to correct the observed H-band radial profile for extinction, one can adopt the approach described in Boizelle et al. (2019): examine the impact of extinction on the inferred $v_{c,\star}$ profile by adjusting the central H-band surface brightness profile to correct for three fiducial values of disk extinction that bracket the likely range. An example of the end result of these different dust-masked and dust-corrected stellar surface brightness profiles is shown in Figure 3.10. The best-fit radial circular velocity profile lies within the envelope created from the different dust-corrected MGE-derived $\mathrm{v}_{c,\star}$ solutions, albeit with a different dependence on radius. We aim to extend this and facilitate dust correction on a pixel-by-pixel basis to promote more robust and fulsome $M_{\rm BH}$ error budgets.

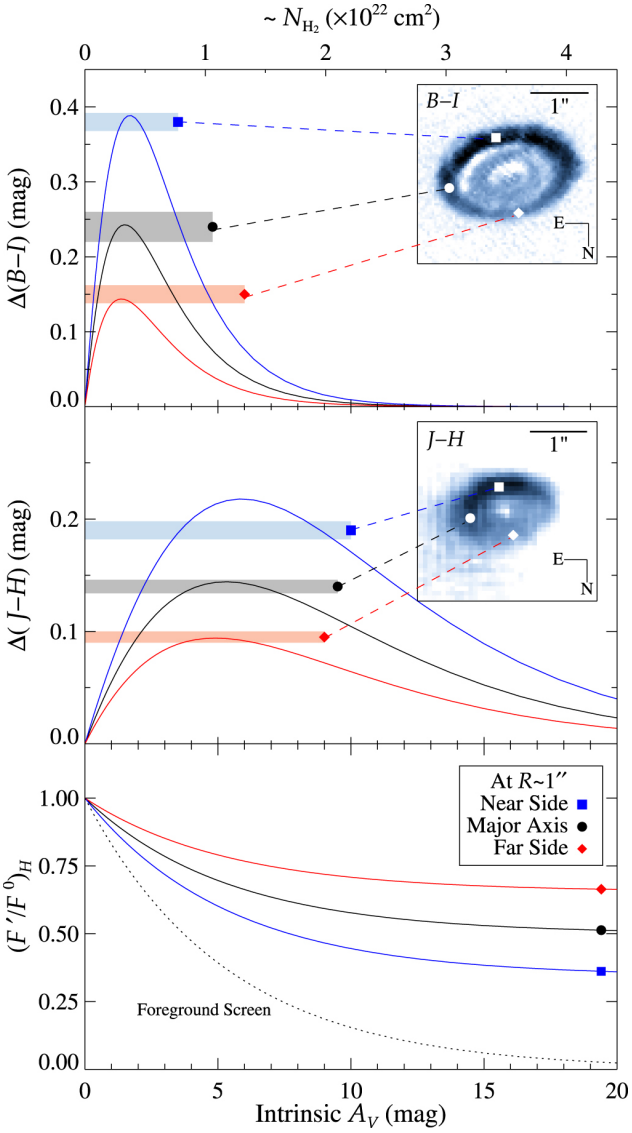

Figure 3.9 Modeled color excess (*top* and *middle panels*) and integrated line of sight H-band intensity (bottom panel) as functions of intrinsic V-band extinction A_V for the inclined, embedded-screen dust disk model with $i = 48^\circ$ (see Equations 3.4-3.6). Results were calculated for three disk locations each for the $B-I$ and $J-H$ maps at points within the ring of maximum color excess for each of the two color maps. Horizontal bars illustrate the ranges of $B-I$ and $J-H$ colors at each of these positions for comparison with model predictions. The $J-H$ color reaches maximal values at smaller radii than the $B-I$ color, indicating that the disk becomes increasingly opaque toward the center. The bottom panel also illustrates the integrated line of sight H-band intensity for the case of a foreground rather than embedded dust screen (dotted curve); in this case, the observed flux falls to zero in the limit of high disk extinction. [From Boizelle et al. (2019)]

3.5 Conclusion

Currently, the high-mass end of $M_{\rm BH}$-galaxy correlations remains underpopulated, with several of these BH measurements being less confident. Additional $M_{\rm BH}$ determinations are needed to better probe the co-evolution of the BH and its host galaxy over cosmic time, especially those at high precision. ALMA CO imaging of dynamically cold CO kinematics has enabled some of the most precise BH mass measurements to date, although ALMA data have been used in only a handful of cases. In this paper, we presented some of the data and detail MGE construction in preparation for gas-dynamical modeling. When fully utilized, the stellar luminosity models reported here will expand the number of confident BH mass measurements using ALMA by a factor of nearly three, and robust $M_{\rm BH}$ determinations in E/S0 galaxies by $\sim$25%. BH mass error budgets are often dominated by uncertainties in the central stellar surface brightness slope due to CND dust attenuation, and few studies have explored the effect that these uncertainties have on

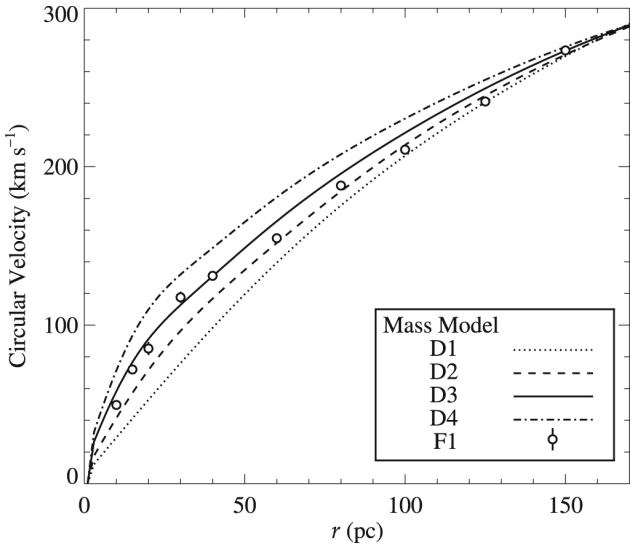

Figure 3.10 Plot comparing the circular velocity profiles ($v_{c,\star}$) arising from the enclosed stellar luminosity after scaling by the best-fitting stellar H-band mass-to-light ratios. These stellar luminosity models were constructed by deprojecting the dust-masked (model D1) and dust-corrected (models D2-D4) cases using a multi-Gaussian Expanssion (MGE). The best-fit radial circular velocity profile (in model F1) lies within the envelope of these MGE-derived $v_{c,\star}$ solutions, albeit with a different dependence on radius. [From Boizelle et al. (2019)]

stellar luminosity models and final $M_{\rm BH}$ measurements. Future work will explore dust attenuation modeling to create corrected MGEs.

From the ALMA archive, we have identified 26 ETGs whose CNDs show clean CO kinematics and good prospects for eventual $M_{\rm BH}$ determination. For this subset of ALMA-observed ETGs, we have obtained new optical and near-IR HST imaging to supplement archival HST data. After masking the worst of the dust attenuation, the H-band mosaics are generally well fit by these MGE models, with fractional differences typically smaller than $\sim 10\%$. In most cases, the larger discrepancies result from constraints on q' that are needed to enable deprojection. These $q'_{\rm min}$ levels primarily impact galaxies that show steep rises in ellipticity at larger radii, but should not affect the fidelity of MGE solutions within $R_{\rm dust}$ in most cases. During optimization, the PA of the MGE components are tied together, with the result being modest mismatches at larger radii in some cases with strong isophotal twists.

On smaller scales, the dusty disks generally appear to be dynamically relaxed in their respective galaxy midplanes. However, disk warping is evident in some dust features as well as CO kinematics in the literature. The q' constraints were based on dust b/a, so some ambiguity in the disk inclination angle may slightly impact the MGE solutions presented here. Despite the best masking efforts, dust attenuation still influences the MGE goodness-of-fit in the central regions, leading to inner components that are not as tightly constrained.

Comparing our MGE solutions to those in the literature, we find minimal ($\sim$10%) differences between the derived circular velocity profiles $v_{\rm c}(r)$ or the corresponding enclosed mass profiles $M(<r)$ when constructing MGEs from data in the same filter. From fits that also included larger-scale data, we also determined that the MGEs reported in Table 3.1 should be reliable out to the edge of the HST footprint, which in most cases extends out to $R \sim 2'$. In one case, comparing our MGE to one constructed using optical data shows more significant differences. This may be due to differences in the dust mask or just the wavelength difference. Our MGEs fit to H-band mosaics

allow for better recovery of the intrinsic stellar light in unmasked regions.

Previous MGEs made for gas-dynamical modeling were not always uniformly constructed and at times lacked a straightforward approach to masking dust features. The MGE models in this thesis will help correct these problems and provide the best possible results for gas-dynamical modeling. The data files and products arising from this project will also prove useful beyond its primary goal of supporting the existing ALMA data sets. These dust-masked MGEs will facilitate other dynamical modeling efforts, including those using stellar kinematic data or those that will pursue a re-analysis of past ionized gas-dynamical modeling (Beifiori et al. 2009). These multi-wavelength HST data will be key to constraining dust attenuation across the disk, and forthcoming dust-corrected MGEs will ensure robust exploration of BH mass measurement errors. Because of both its depth and wavelength coverage, this HST data and ongoing analysis will have additional legacy value in studies of stellar population gradients, central star formation, and globular cluster populations in ETGs.

Appendix A

Supplementary Material

Due to the large number of figures in this thesis, we are placing in this Appendix all but one of the figures showing our MGE results to not distract from the main paper.

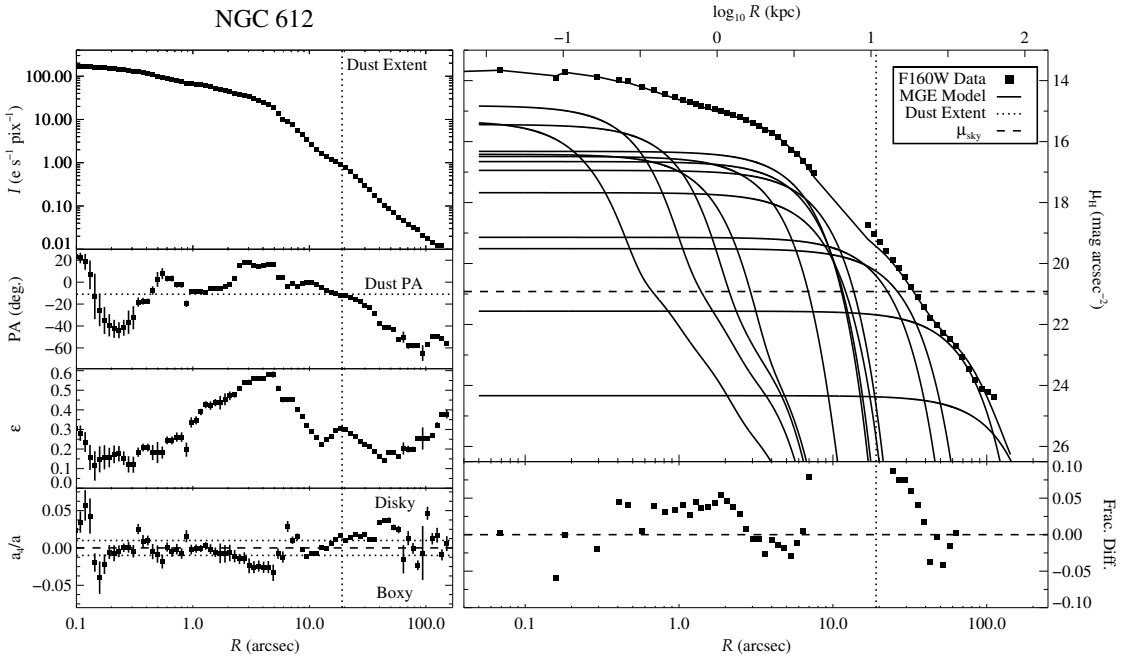

Figure A.1 Same as for Figure 3.1 but for NGC 612.

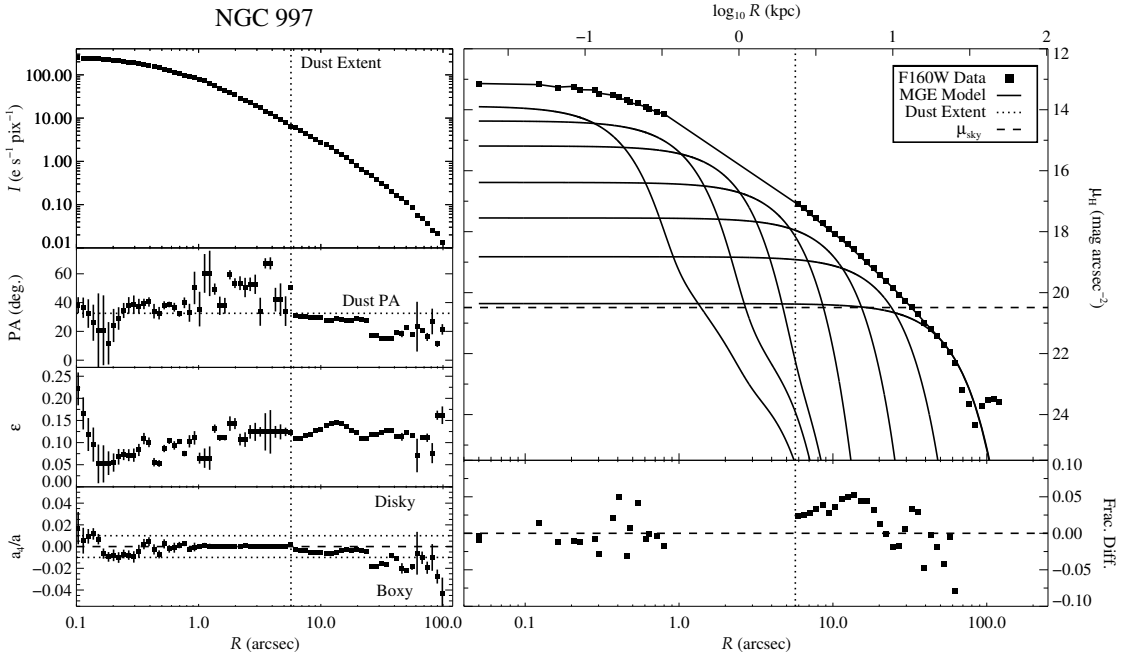

Figure A.2 Same as for Figure 3.1 but for NGC 997.

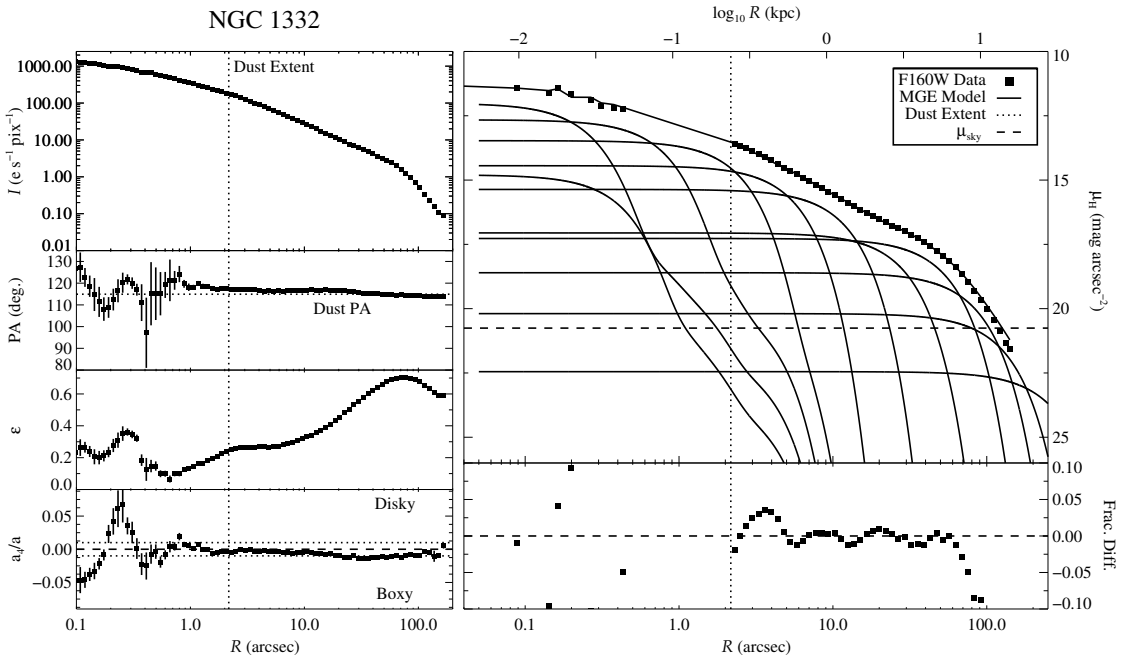

Figure A.3 Same as for Figure 3.1 but for NGC 1332.

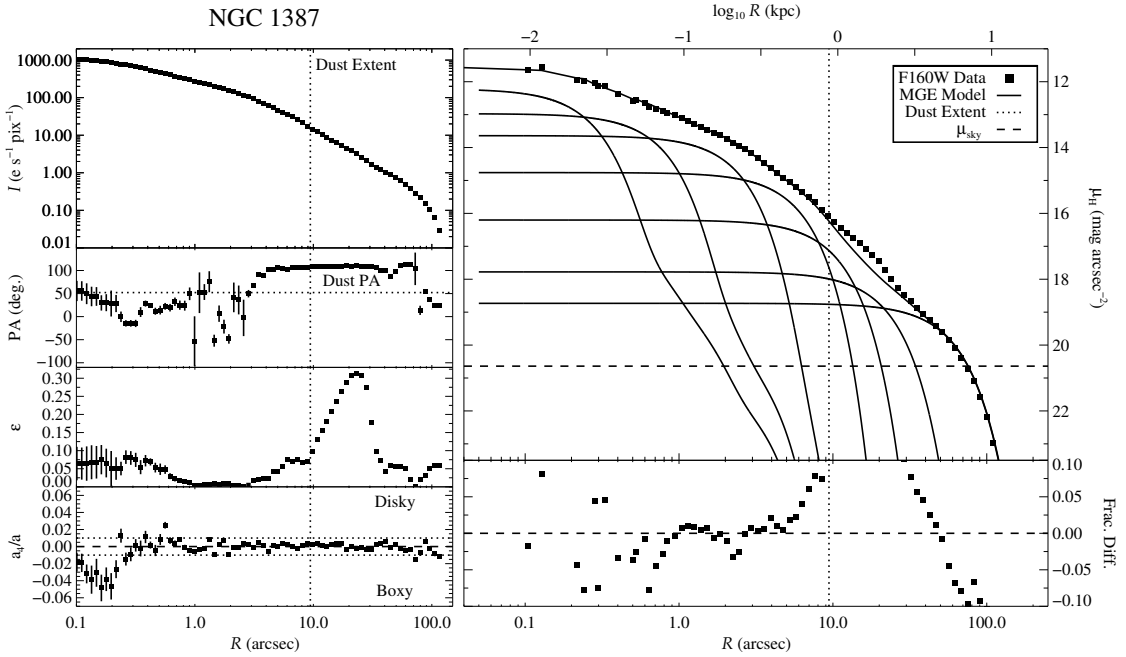

Figure A.4 Same as for Figure 3.1 but for NGC 1387.

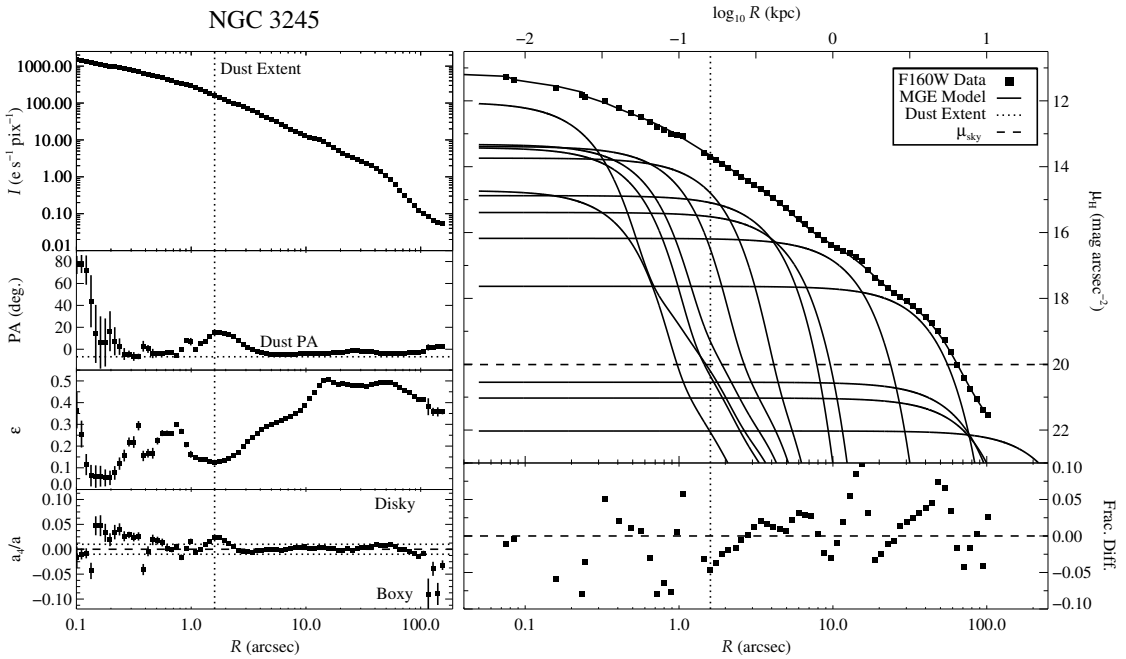

Figure A.5 Same as for Figure 3.1 but for NGC 3245.

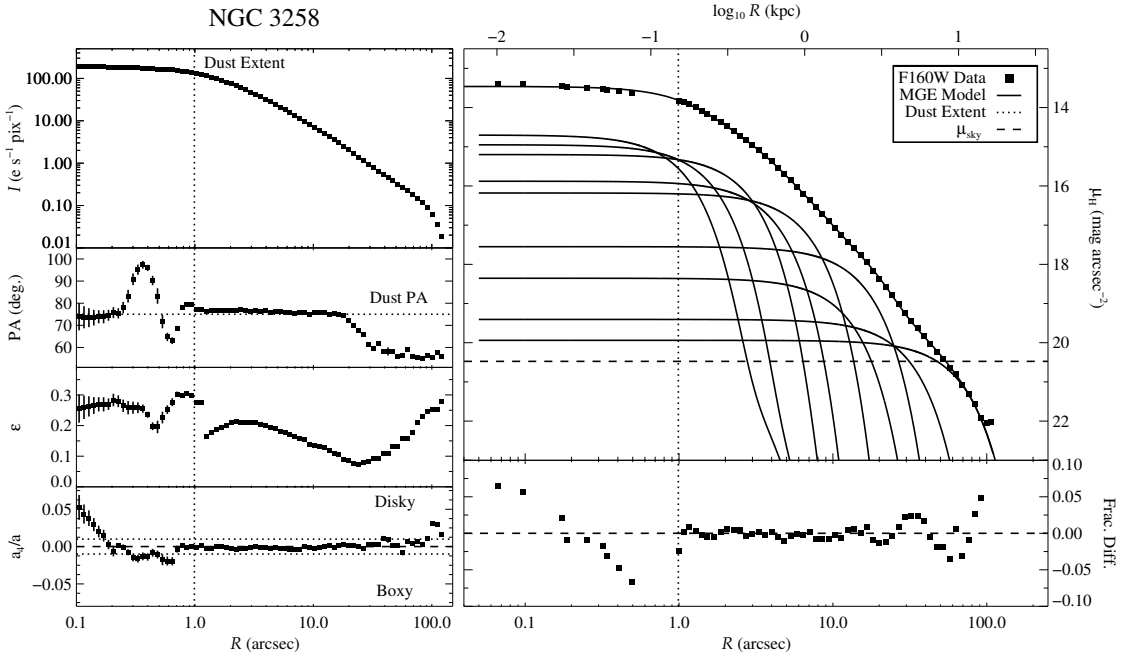

Figure A.6 Same as for Figure 3.1 but for NGC 3258.

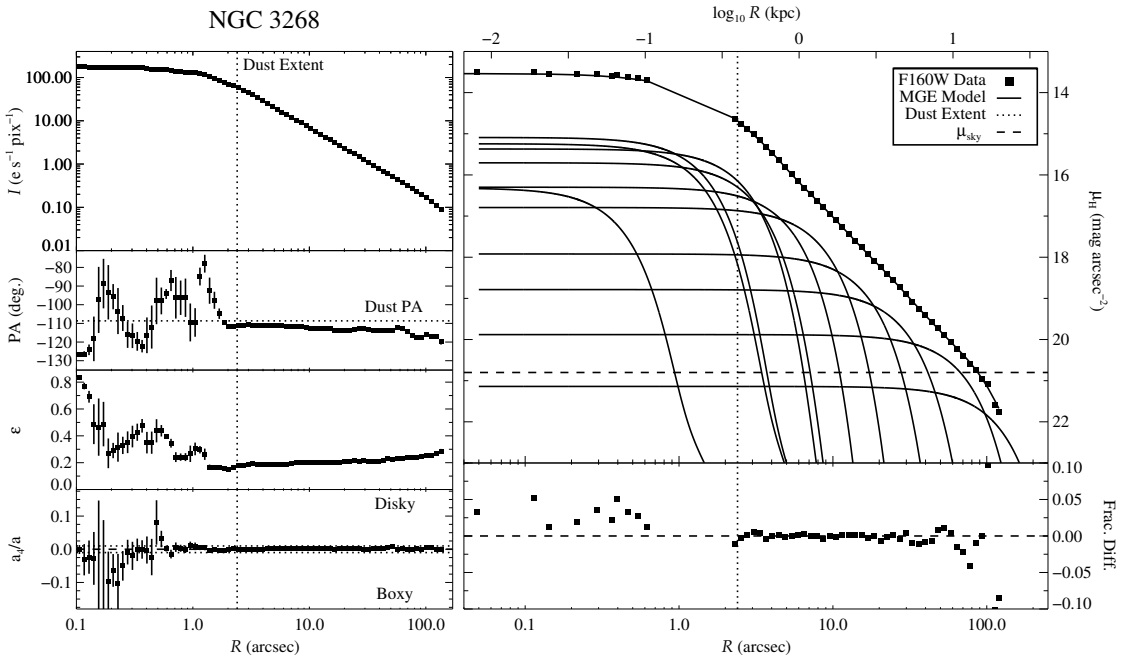

Figure A.7 Same as for Figure 3.1 but for NGC 3268.

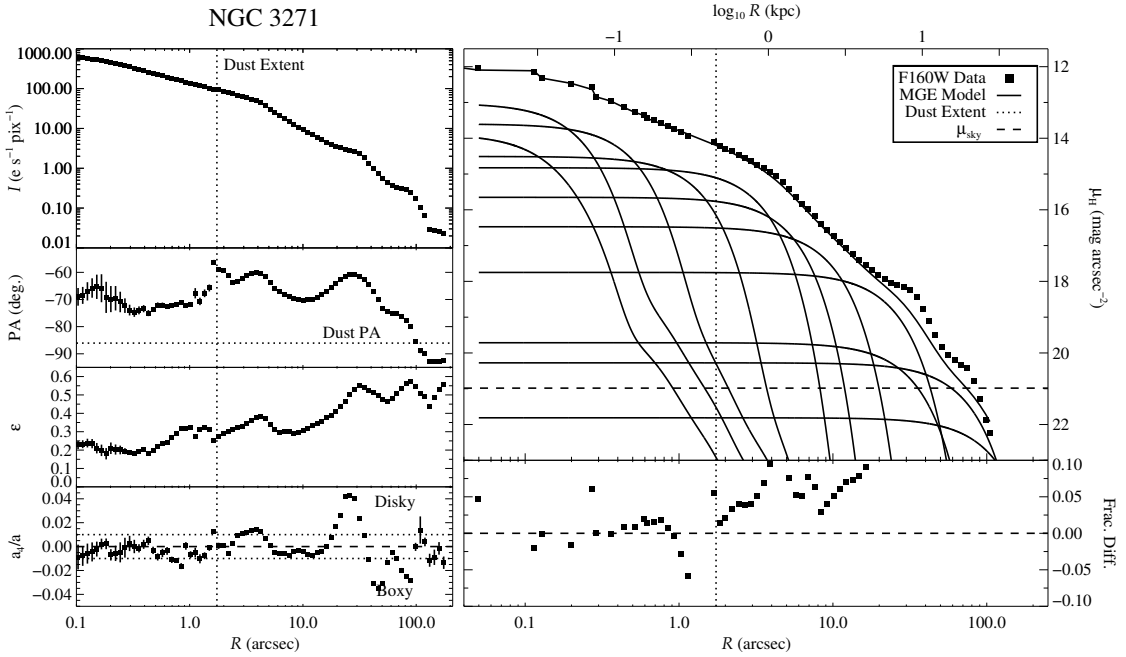

Figure A.8 Same as for Figure 3.1 but for NGC 3271.

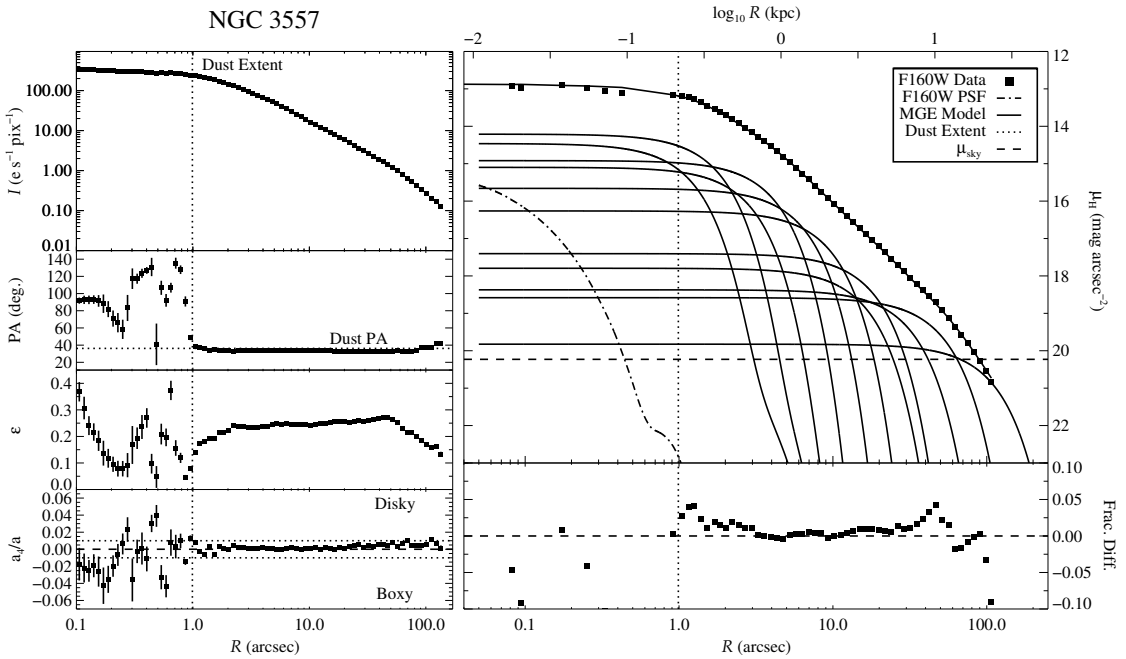

Figure A.9 Same as for Figure 3.1 but for NGC 3557.

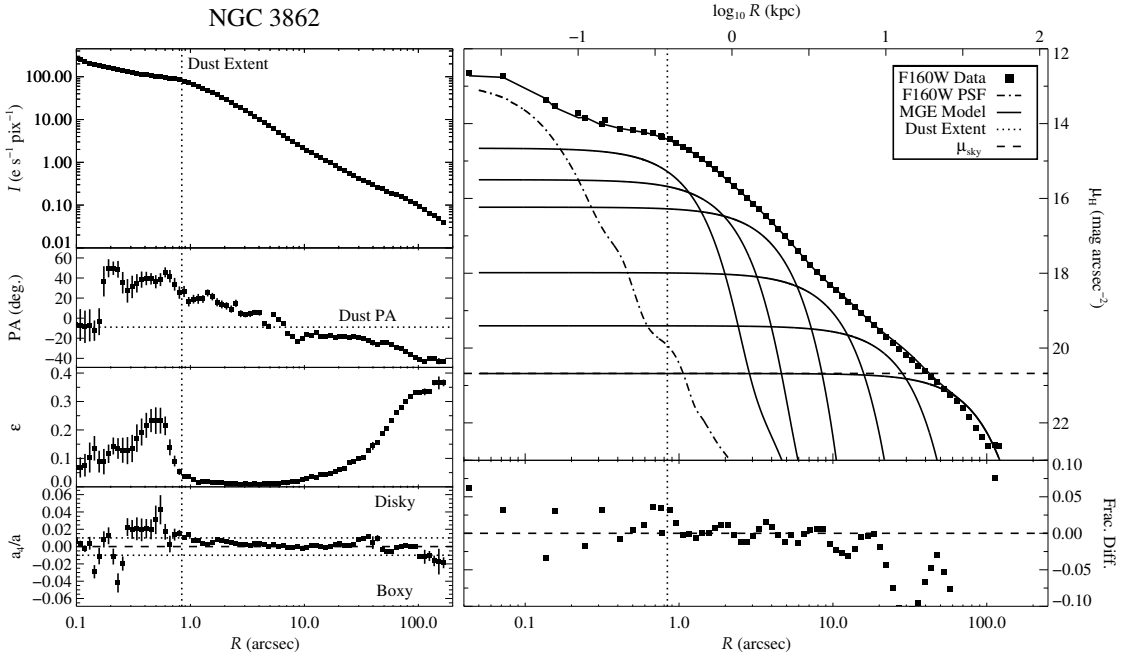

Figure A.10 Same as for Figure 3.1 but for NGC 3862.

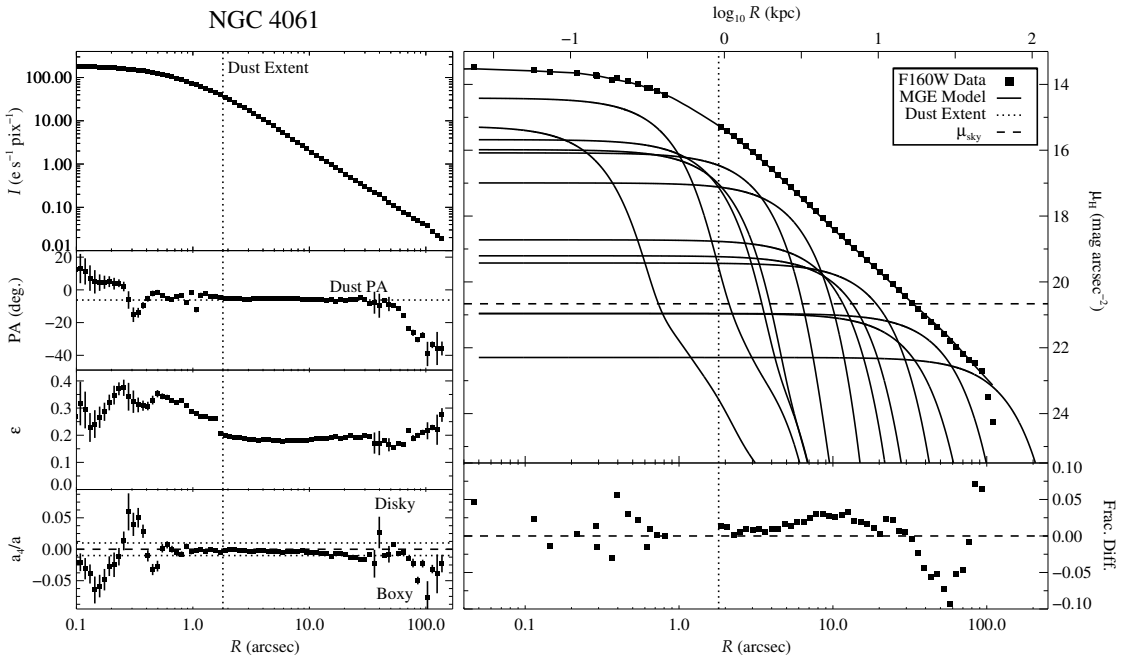

Figure A.11 Same as for Figure 3.1 but for NGC 4061.

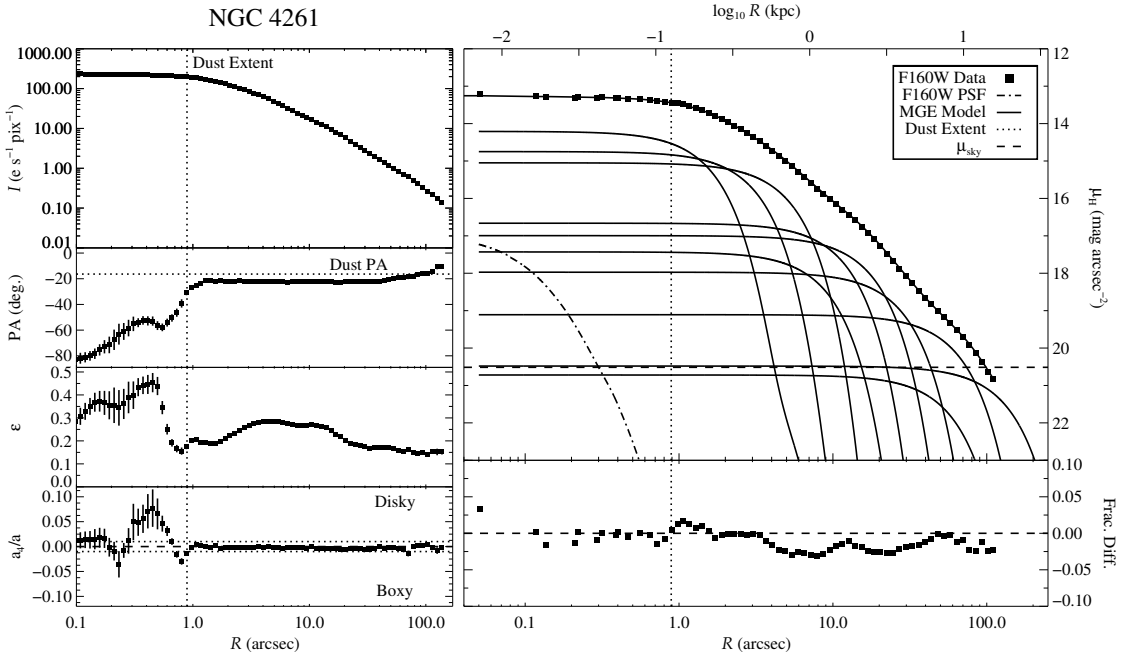

Figure A.12 Same as for Figure 3.1 but for NGC 4261.

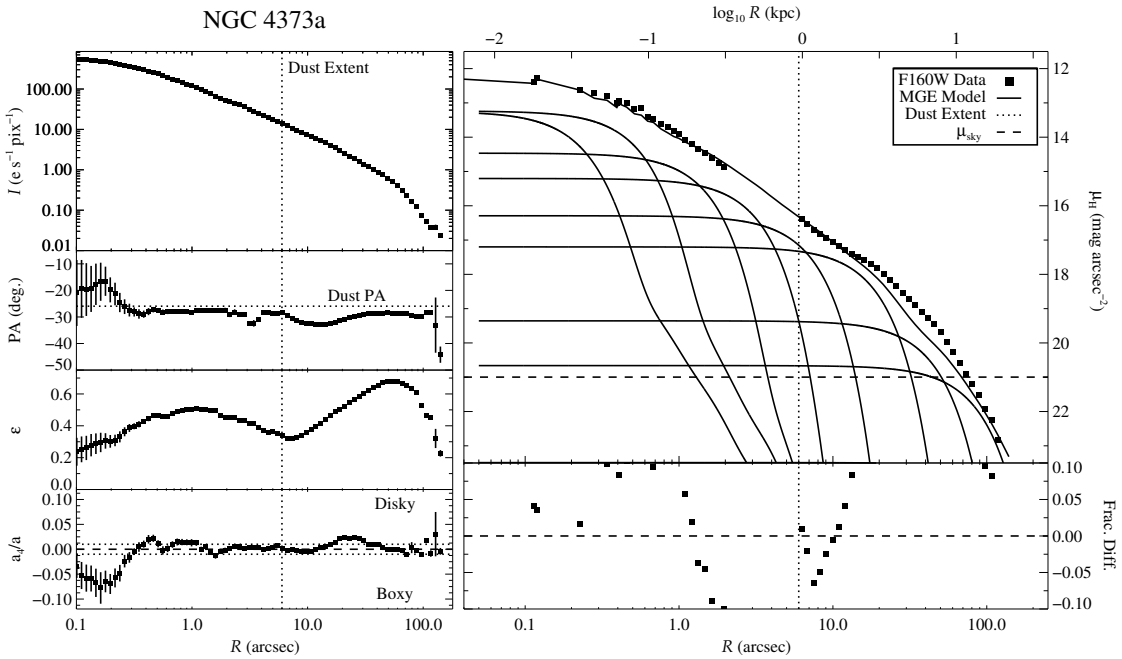

Figure A.13 Same as for Figure 3.1 but for NGC 4373a.

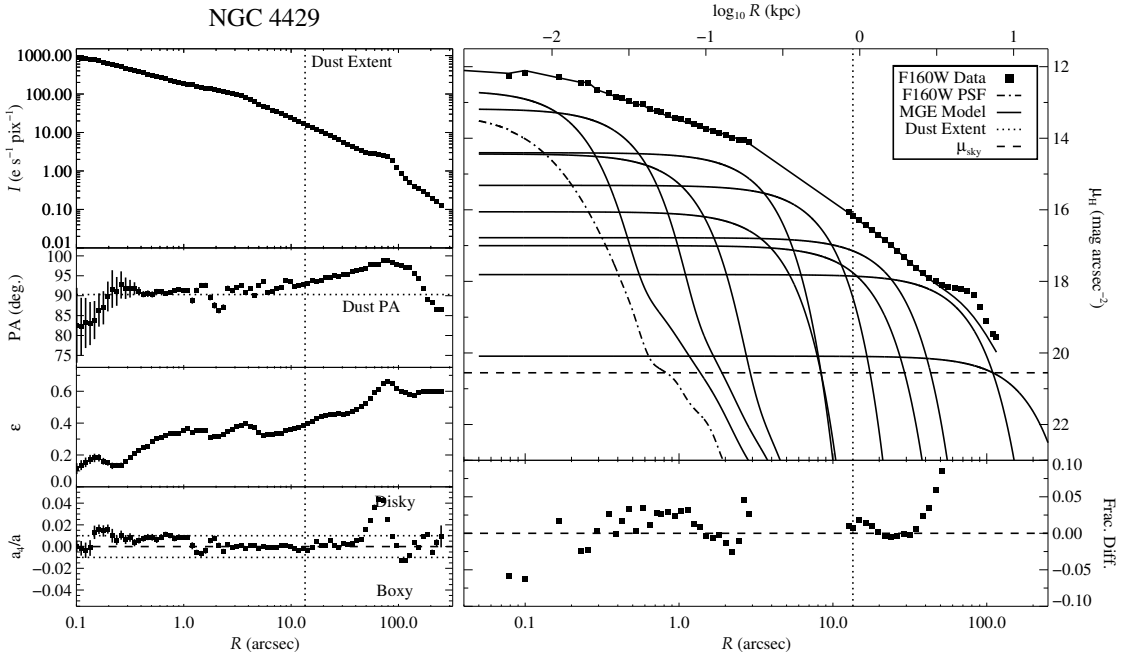

Figure A.14 Same as for Figure 3.1 but for NGC 4429.

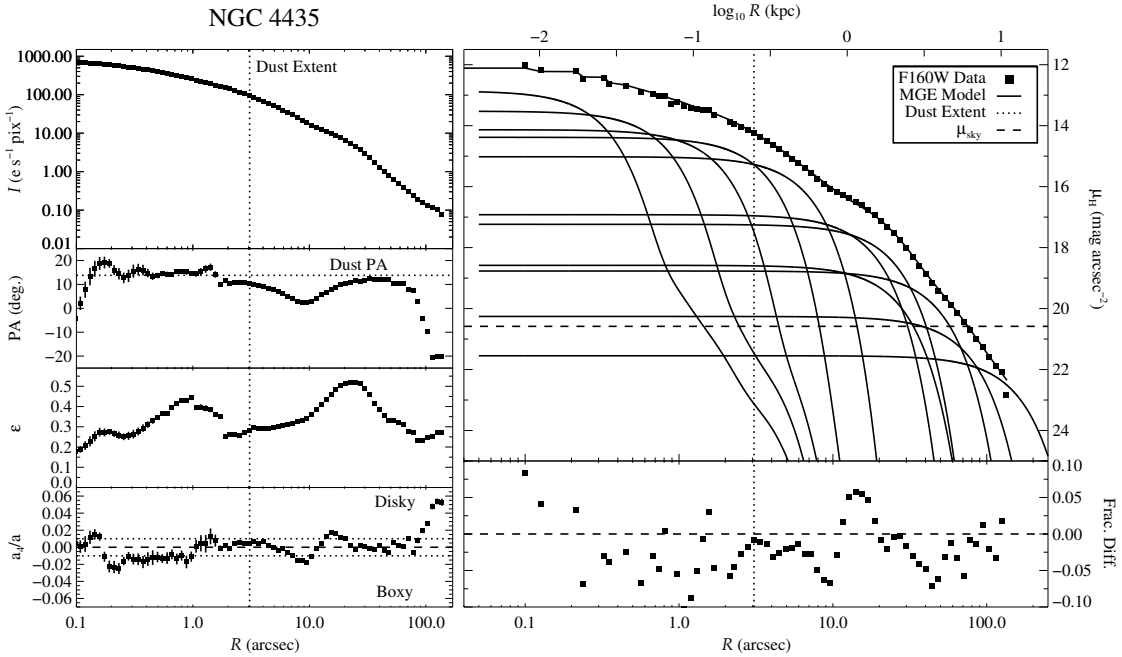

Figure A.15 Same as for Figure 3.1 but for NGC 4435.

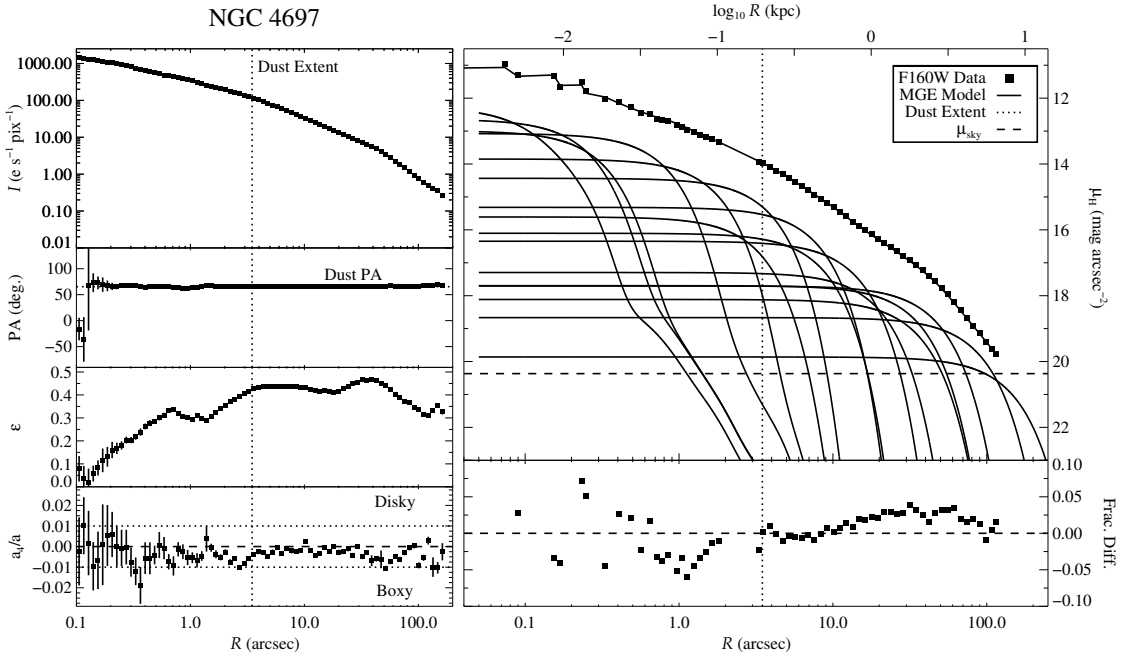

Figure A.16 Same as for Figure 3.1 but for NGC 4697.

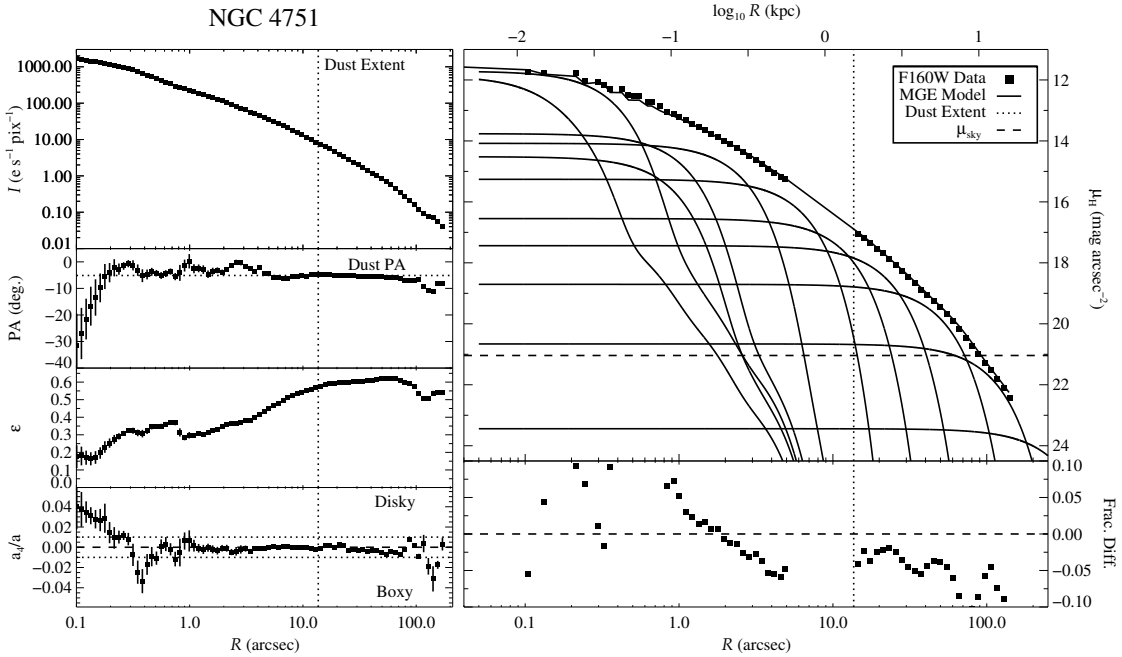

Figure A.17 Same as for Figure 3.1 but for NGC 4751.

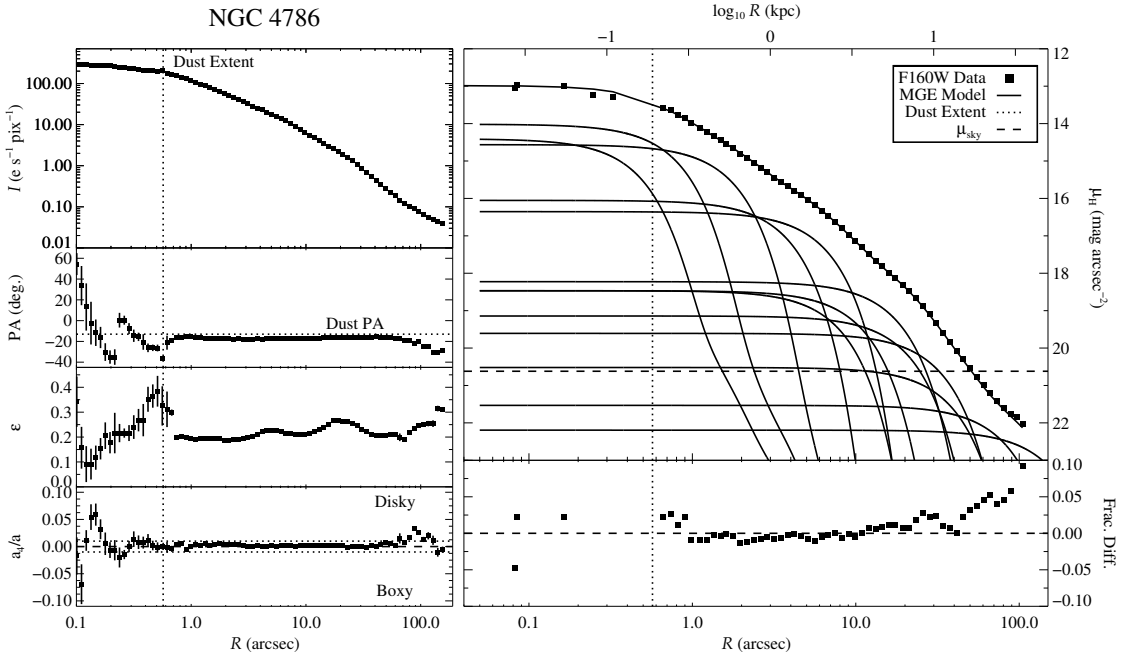

Figure A.18 Same as for Figure 3.1 but for NGC 4786.

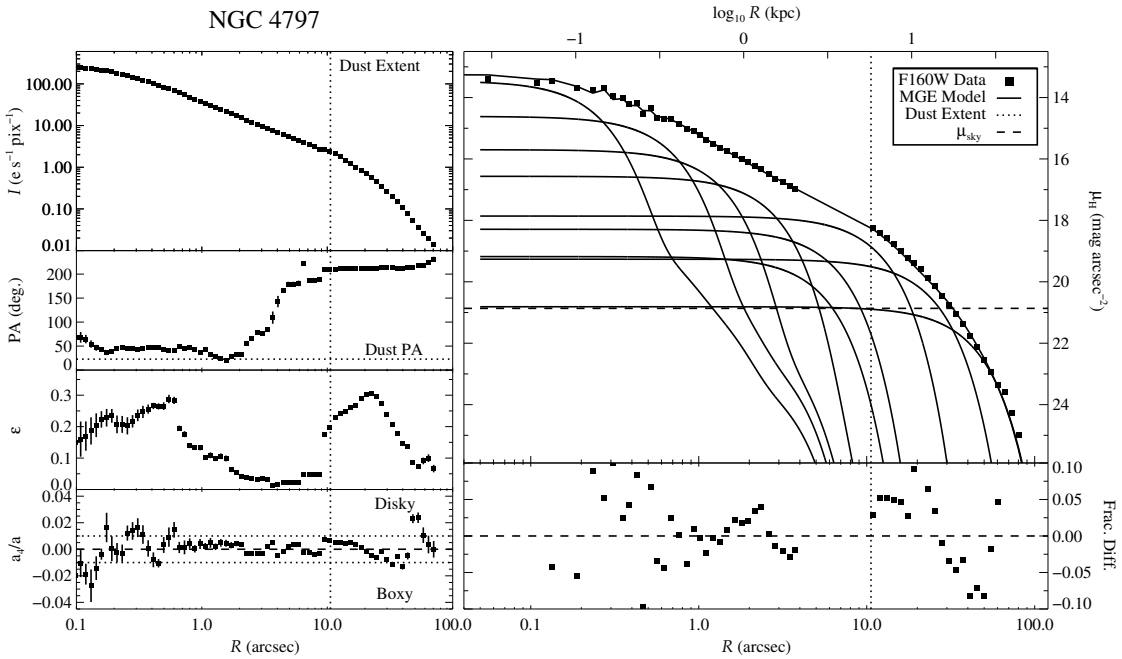

Figure A.19 Same as for Figure 3.1 but for NGC 4797.

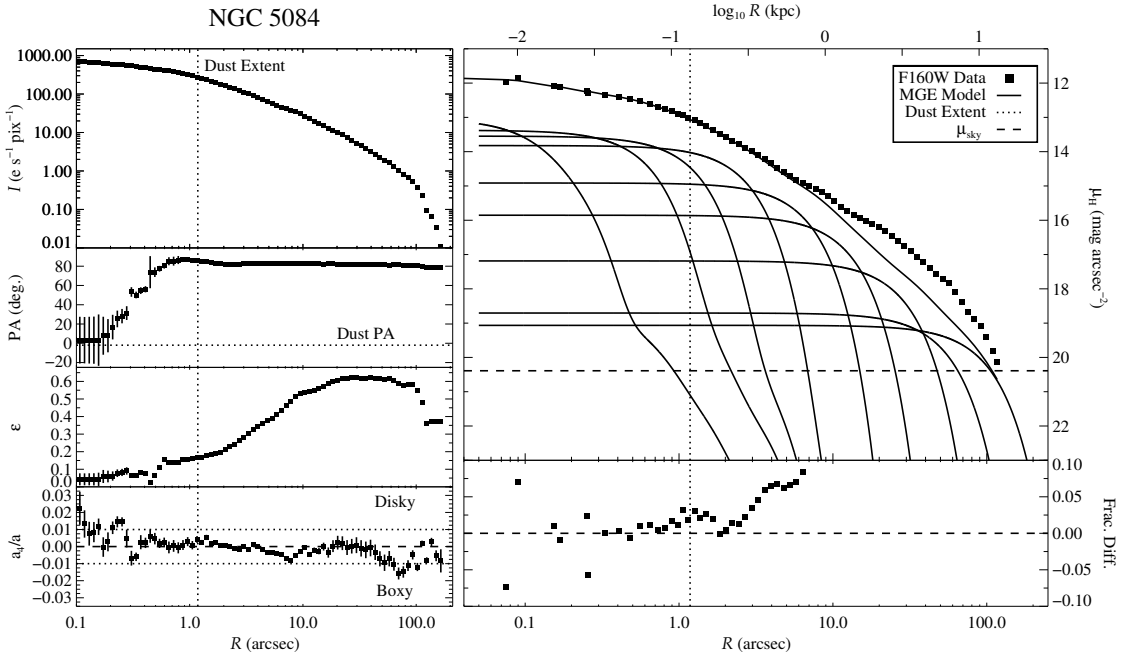

Figure A.20 Same as for Figure 3.1 but for NGC 5084.

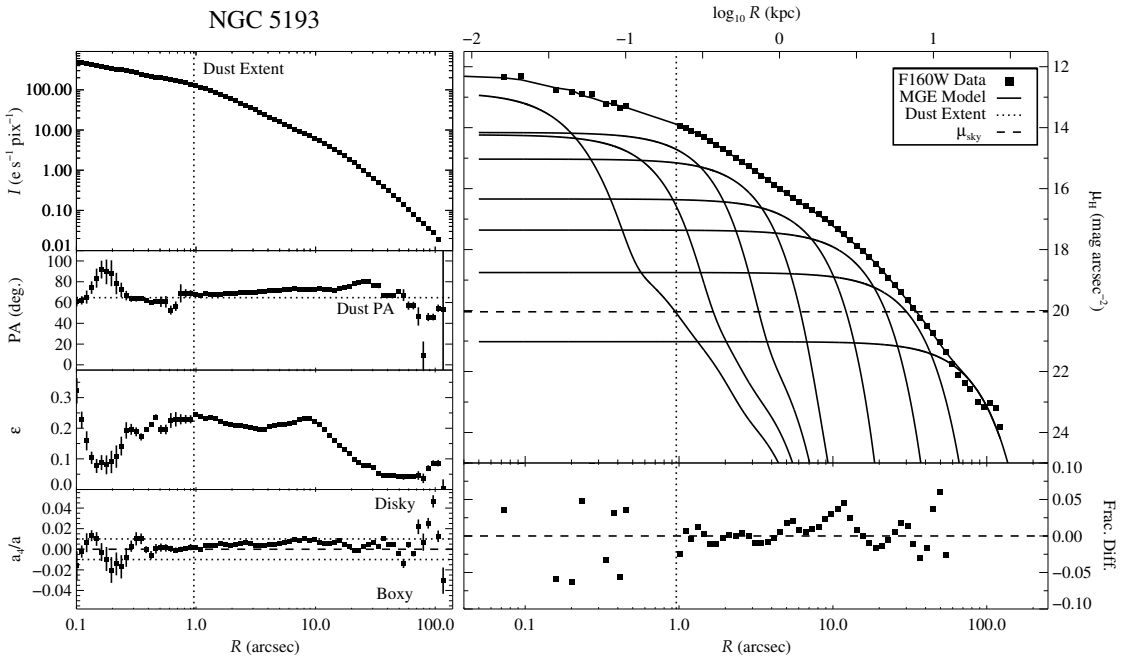

Figure A.21 Same as for Figure 3.1 but for NGC 5193.

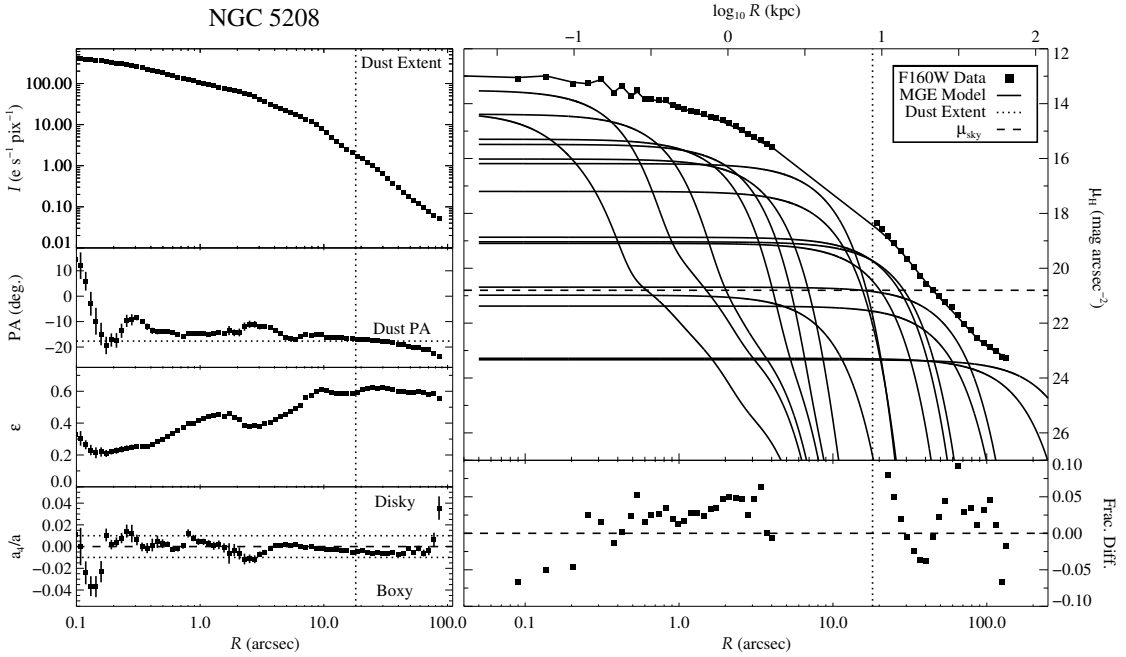

Figure A.22 Same as for Figure 3.1 but for NGC 5208.

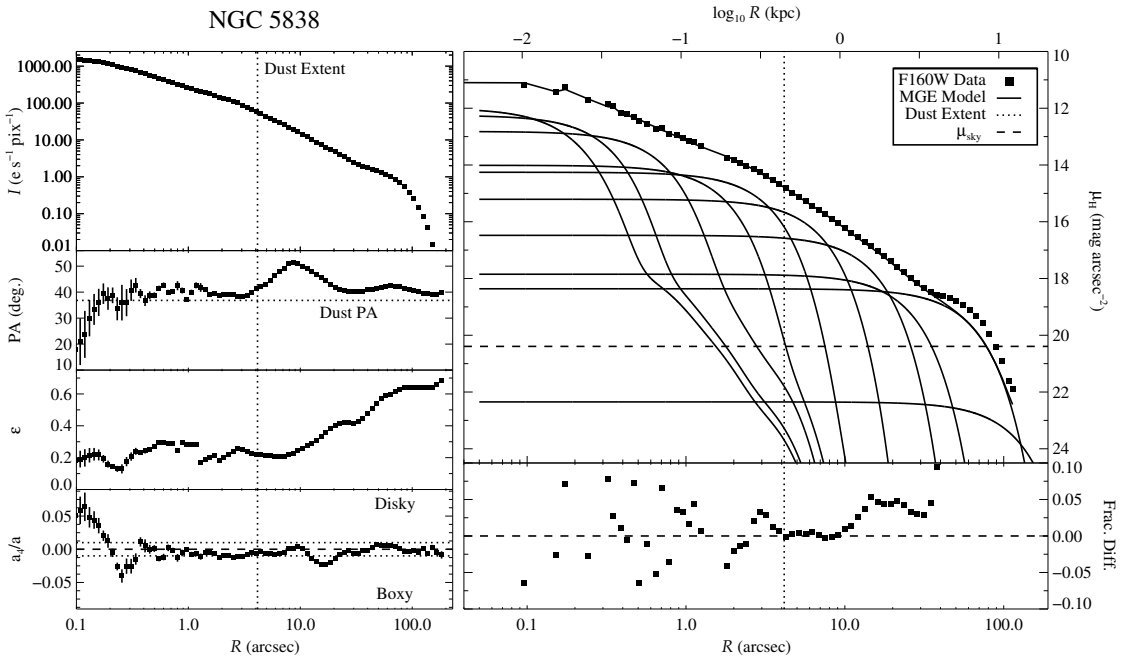

Figure A.23 Same as for Figure 3.1 but for NGC 5838.

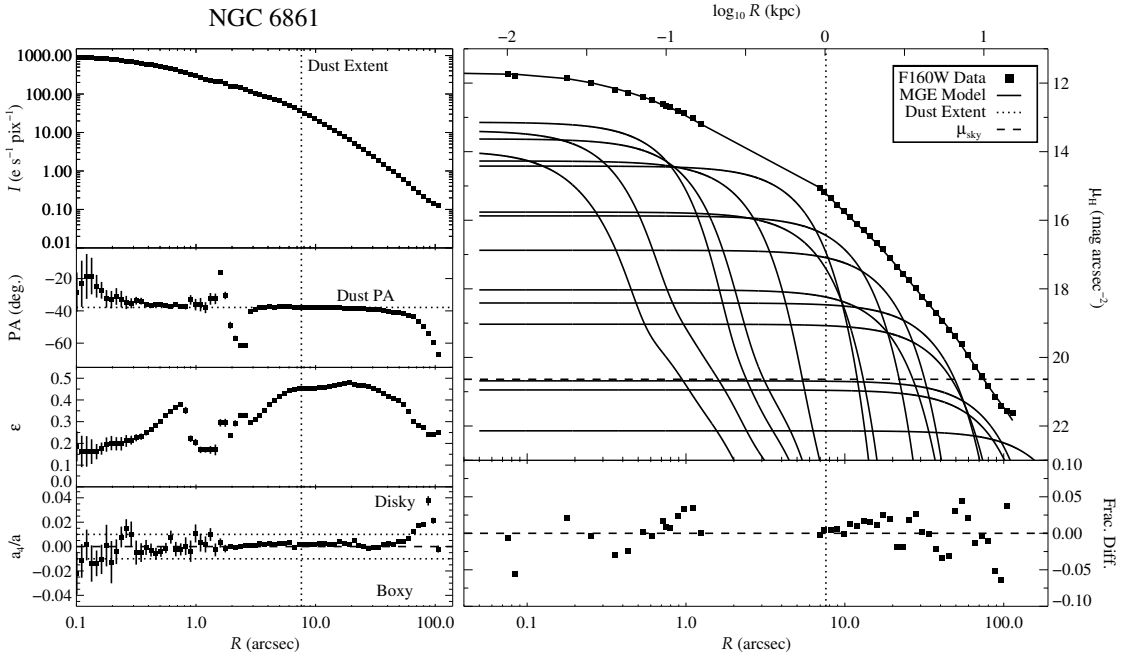

Figure A.24 Same as for Figure 3.1 but for NGC 6861.

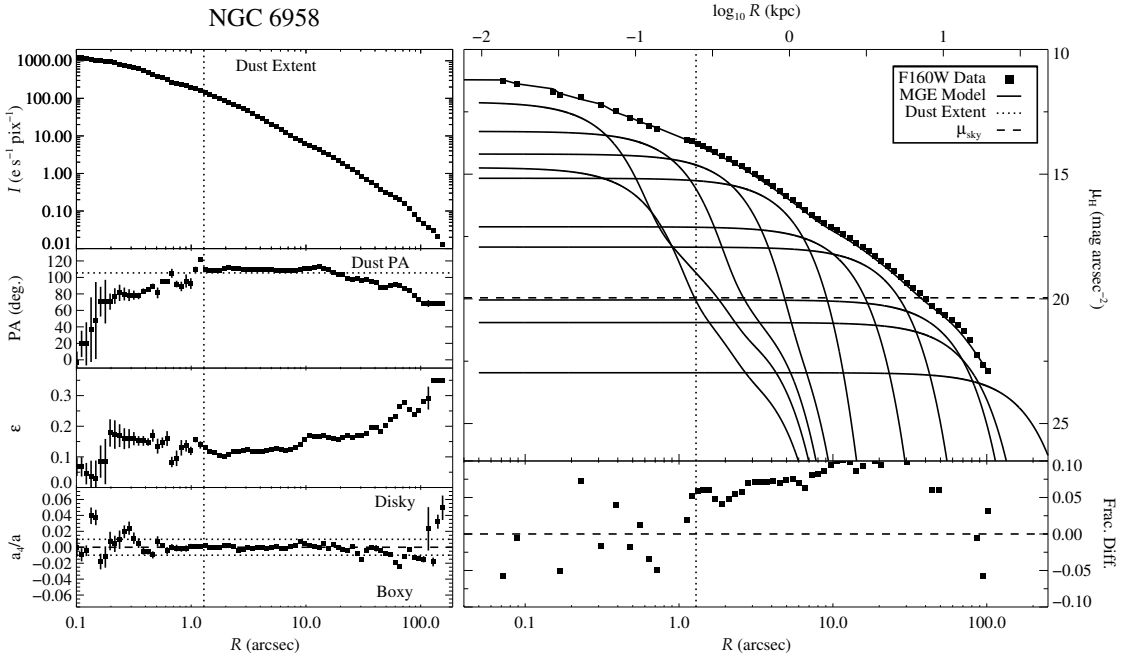

Figure A.25 Same as for Figure 3.1 but for NGC 6958.

Bibliography

Alatalo, K., et al. 2013, MNRAS, 432, 1796

Astropy Collaboration et al. 2018, AJ, 156, 123

Barth, A. J., Boizelle, B. D., Darling, J., Baker, A. J., Buote, D. A., Ho, L. C., & Walsh, J. L. 2016a, ApJ, 822, L28

Barth, A. J., Darling, J., Baker, A. J., Boizelle, B. D., Buote, D. A., Ho, L. C., & Walsh, J. L. 2016b, ApJ, 823, 51

Beifiori, A., Sarzi, M., Corsini, E. M., Dalla Bontà, E., Pizzella, A., Coccato, L., & Bertola, F. 2009, ApJ, 692, 856

Bernardi, M., Hyde, J. B., Sheth, R. K., Miller, C. J., & Nichol, R. C. 2007, AJ, 133, 1741

Blakeslee, J. P., Jensen, J. B., Ma, C.-P., Milne, P. A., & Greene, J. E. 2021, ApJ, 911, 65

Blakeslee, J. P., et al. 2009, ApJ, 694, 556

Bogdán, Á., Lovisari, L., Volonteri, M., & Dubois, Y. 2018, ApJ, 852, 131

Boizelle, B. D., Barth, A. J., Darling, J., Baker, A. J., Buote, D. A., Ho, L. C., & Walsh, J. L. 2017, ApJ, 845, 170

Boizelle, B. D., Barth, A. J., Walsh, J. L., Buote, D. A., Baker, A. J., Darling, J., & Ho, L. C. 2019, ApJ, 881, 10

Boizelle, B. D., et al. 2021, ApJ, 908, 19

Bonfini, P., González-Martín, O., Fritz, J., Bitsakis, T., Bruzual, G., & Cervantes Sodi, B. 2018, MNRAS, 478, 1161

Cantiello, M., Blakeslee, J. P., Raimondo, G., Mei, S., Brocato, E., & Capaccioli, M. 2005, ApJ, 634, 239

Cappellari, M. 2002, MNRAS, 333, 400

—. 2008, MNRAS, 390, 71

Cappellari, M., et al. 2011, MNRAS, 413, 813

Cohn, J. H., et al. 2021, ApJ, 919, 77

Davis, T. A. 2014, MNRAS, 443, 911

Davis, T. A., Bureau, M., Cappellari, M., Sarzi, M., & Blitz, L. 2013, Nature, 494, 328

Davis, T. A., Bureau, M., Onishi, K., Cappellari, M., Iguchi, S., & Sarzi, M. 2017, MNRAS, 468, 4675

Davis, T. A., Greene, J., Ma, C.-P., Pandya, V., Blakeslee, J. P., McConnell, N., & Thomas, J. 2016, MNRAS, 455, 214

Davis, T. A., Greene, J. E., Ma, C.-P., Blakeslee, J. P., Dawson, J. M., Pandya, V., Veale, M., & Zabel, N. 2019, MNRAS, 486, 1404

Davis, T. A., et al. 2011, MNRAS, 414, 968

—. 2018, MNRAS, 473, 3818

—. 2022, MNRAS, 512, 1522

De Bruyne, V., De Rijcke, S., Dejonghe, H., & Zeilinger, W. W. 2004, MNRAS, 349, 440

de Nicola, S., Saglia, R. P., Thomas, J., Dehnen, W., & Bender, R. 2020, MNRAS, 496, 3076

Del Popolo, A. 2009, ApJ, 698, 2093

Dickey, J. M., & Kazes, I. 1992, ApJ, 393, 530

Dressel, L. 2022, in WFC3 Instrument Handbook for Cycle 30 v. 14, Vol. 14, 14

Duah Asabere, B., Horellou, C., Jarrett, T. H., & Winkler, H. 2016, A&A, 592, A20

Elmegreen, B. G., & Block, D. L. 1999, MNRAS, 303, 133

Emsellem, E., Monnet, G., & Bacon, R. 1994, A&A, 285, 723

Ferrarese, L., Ford, H. C., & Jaffe, W. 1996, ApJ, 470, 444

Ferrarese, L., & Merritt, D. 2000, ApJ, 539, L9

Gebhardt, K., et al. 2000, ApJ, 539, L13

Gonzaga, S., Hack, W., Fruchter, A., & Mack, J. 2012, The DrizzlePac Handbook

Goullaud, C. F., Jensen, J. B., Blakeslee, J. P., Ma, C.-P., Greene, J. E., & Thomas, J. 2018, ApJ, 856, 11

Ho, L. C. 2007, ApJ, 669, 821

Jensen, J. B., Tonry, J. L., Barris, B. J., Thompson, R. I., Liu, M. C., Rieke, M. J., Ajhar, E. A., & Blakeslee, J. P. 2003, ApJ, 583, 712

Kabasares, K. M., et al. 2022, ApJ, 934, 162

Kenworthy, W. D., et al. 2022, ApJ, 935, 83

Kormendy, J. 1982, Saas-Fee Advanced Course, 12, 115

Kormendy, J., & Ho, L. C. 2013, ARA&A, 51, 511

Kormendy, J., & Richstone, D. 1995, ARA&A, 33, 581

Krajnović, D., et al. 2011, MNRAS, 414, 2923

Krist, J., & Hook, R. 2004, The Tiny Tim User's Guide, https://www.stsci.edu/files/live/sites/www/files/home/hst/instrumentation/focus-and-pointing/documentation/_documents/tinytim.pdf, Baltimore: STScI

Kuo, C. Y., et al. 2011, ApJ, 727, 20

La Barbera, F., De Carvalho, R. R., De La Rosa, I. G., Gal, R. R., Swindle, R., & Lopes, P. A. A. 2010, AJ, 140, 1528

Lauer, T. R., et al. 2005, AJ, 129, 2138

—. 2007, ApJ, 662, 808

Ma, C.-P., Greene, J. E., McConnell, N., Janish, R., Blakeslee, J. P., Thomas, J., & Murphy, J. D. 2014, ApJ, 795, 158

Maiolino, R. 2008, New A Rev., 52, 339

McConnell, N. J., & Ma, C.-P. 2013, ApJ, 764, 184

McMaster, M., & et al. 2008, Wide Field and Planetary Camera 2 Instrument Handbook v. 10.0

Mei, S., et al. 2007, ApJ, 655, 144

Mould, J. R., et al. 2000, ApJ, 529, 786

Neumayer, N., Cappellari, M., Reunanen, J., Rix, H. W., van der Werf, P. P., de Zeeuw, P. T., & Davies, R. I. 2007, ApJ, 671, 1329

North, E. V., et al. 2019, MNRAS, 490, 319

Onishi, K., Iguchi, S., Davis, T. A., Bureau, M., Cappellari, M., Sarzi, M., & Blitz, L. 2017, MNRAS, 468, 4663

Paturel, G., Petit, C., Prugniel, P., Theureau, G., Rousseau, J., Brouty, M., Dubois, P., & Cambrésy, L. 2003, A&A, 412, 45

Peng, C. Y., Ho, L. C., Impey, C. D., & Rix, H.-W. 2010, AJ, 139, 2097

Pirzkal, N. 2014, The Near Infrared Sky Background, Instrument Science Report WFC3 2014-11, 11 pages

Riess, A. G., et al. 2022, ApJ, 934, L7

Ruffa, I., et al. 2019, MNRAS, 484, 4239

—. 2023, MNRAS, 522, 6170

Rusli, S. P., et al. 2013, AJ, 146, 45

Ryon, J. E. 2022, in ACS Instrument Handbook for Cycle 30 v. 21.0, Vol. 21, 21

Saglia, R. P., et al. 2016, ApJ, 818, 47

Science Software Branch at STScI. 2012, PyRAF: Python alternative for IRAF, Astrophysics Source Code Library, record ascl:1207.011

Smith, M. D., et al. 2019, MNRAS, 485, 4359

—. 2021a, MNRAS, 500, 1933

—. 2021b, MNRAS, 503, 5984

Sofue, Y. 1992, PASJ, 44, L231

Thater, S., et al. 2022, MNRAS, 509, 5416

Tiley, A. L., Bureau, M., Saintonge, A., Topal, S., Davis, T. A., & Torii, K. 2016, MNRAS, 461, 3494

Tiley, A. L., et al. 2019, MNRAS, 482, 2166

Tody, D. 1986, in Society of Photo-Optical Instrumentation Engineers (SPIE) Conference Series, Vol. 627, Instrumentation in astronomy VI, ed. D. L. Crawford, 733

Tody, D. 1993, in Astronomical Society of the Pacific Conference Series, Vol. 52, Astronomical Data Analysis Software and Systems II, ed. R. J. Hanisch, R. J. V. Brissenden, & J. Barnes, 173

Tonry, J. L., Dressler, A., Blakeslee, J. P., Ajhar, E. A., Fletcher, A. B., Luppino, G. A., Metzger, M. R., & Moore, C. B. 2001, ApJ, 546, 681

Topal, S., Bureau, M., Tiley, A. L., Davis, T. A., & Torii, K. 2018, MNRAS, 479, 3319

Tran, H. D., Tsvetanov, Z., Ford, H. C., Davies, J., Jaffe, W., van den Bosch, F. C., & Rest, A. 2001, AJ, 121, 2928

van den Bosch, R. C. E., & de Zeeuw, P. T. 2010, MNRAS, 401, 1770

van den Bosch, R. C. E., Greene, J. E., Braatz, J. A., Constantin, A., & Kuo, C.-Y. 2016, ApJ, 819, 11

van den Bosch, R. C. E., van de Ven, G., Verolme, E. K., Cappellari, M., & de Zeeuw, P. T. 2008, MNRAS, 385, 647

Vazdekis, A., Sánchez-Blázquez, P., Falcón-Barroso, J., Cenarro, A. J., Beasley, M. A., Cardiel, N., Gorgas, J., & Peletier, R. F. 2010, MNRAS, 404, 1639

Verdoes Kleijn, G. A., van der Marel, R. P., & Noel-Storr, J. 2006, AJ, 131, 1961

Viaene, S., Sarzi, M., Baes, M., Fritz, J., & Puerari, I. 2017, MNRAS, 472, 1286

Wright, E. L. 2006, PASP, 118, 1711

Yoon, I. 2017, MNRAS, 466, 1987

Young, L. M., et al. 2011, MNRAS, 414, 940

Zhao, W., et al. 2018, ApJ, 854, 124

Zhao, Y., Ho, L. C., Shangguan, J., Kim, M., Zhao, D., & Gao, H. 2021, ApJ, 911, 94

Index